Mathematical Modelling of Casting Processes

by

Zia Abdullah
B.A.Sc. (Mechanical Engineering)
University of Ottawa, 1982

A Thesis Submitted in Partial Fulfillment of
The Requirements For The Degree of
Doctor of Philosophy
in
Mechanical Engineering

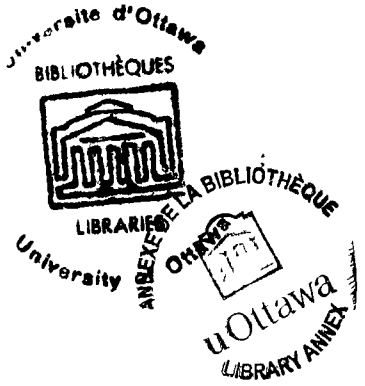

Candidate

Supervisor

Co–supervisor

The University of Ottawa
August 1988

Abstract

Numerical and experimental work is carried out to investigate liquid metal flow and heat transfer during permanent mold casting processes.

Conduction heat transfer during the solidification of a cast iron plate is simulated using a finite difference ADI method. Experimental temperature distributions in the casting and mold are compared with the computed results. The effects of finite pouring time and liquid metal gating locations are investigated. The results indicate the significance of finite pouring time and liquid metal convection on the temperature distributions in the casting and the mold.

Conservation equations of the mass, momentum and energy are solved to simulate the liquid metal flow and heat transfer during the pouring and solidification of a cylindrical grey iron casting in a cast iron mold. The Finite Volume Method is used. Turbulence is simulated using the K–ϵ model. Novel treatments are developed to simulate the rising level of the liquid metal and the free surface during mold filling. A new model is developed to treat liquid metal flow in the solid–liquid mushy region.

The computational methods to treat liquid metal flow during mold filling are verified using experimental data for velocity fields and free surface profiles during the filling of a cylindrical container with water. The natural convection computations are also verified using experimental data for free convection of a Pb–Sn alloy. Experimental work is carried out to obtain temperature distributions during the casting of the cylindrical ingot. Very good agreement is obtained with the computed results. Temperature fields, solidus front shapes and velocity fields during pouring and solidification are reported.

Contents

List of Figures

List of Tables

Nomenclature

a	- nodal coupling coefficients
A	- area
b	- body force (Section 2.3)
B	- computationally large number
B	- body force due to thermal gradients (Section 5.3)
c	- specific heat
C_1	- constant in the K–ϵ model
C_2	- constant in the K–ϵ model
C_D	- constant in the K–ϵ model
C_D	- coefficient of drag (Section 4.2)
C_μ	- constant in the K–ϵ model
C	- carbon percent
d	- diameter
d_1, d_2	- primary and secondary dendrite arm spacing
E	- energy released by a node during solidification
E	- Young's modulus (Section 2.3)
F	- radiation shape factor
$\mathbf{F}$	- force vector (Section 2.3)
g	- gravity
Gr	- Grashof number
h	- enthalpy
h^*	- effective heat transfer coefficient
H	- latent heat content of cell
$H_{c,b}$	- heat flux from the bottom of the casting
$H_{m,b}$	- heat flux into the bottom of the mold
$H_{c,w}$	- heat flux from the side of the casting

$H_{m,w}$ - heat flux into the side of the mold

k - thermal conductivity

K - turbulence kinetic energy

K_p - permeability of porous medium

$\mathbf{K}$ - global stiffness matrix

l - length scale of the tubulent eddys

m - mass

m - tangent to the surface (Chapter 4)

n - normal to the surface (Chapter 4)

p - pressure

P - surface pressure (Chapter 4)

PP - pressure correction variable (Chapter 4)

Pe - cell Peclet number ($u\Delta x/\nu$)

Q - heat generation term (also used for latent heat)

r - radius

R - thermal contact resistance at the mold casting interface

s - solid fraction

S - source term

Sp - component of the linearized source term

Su - component of the linearized source term

t - time

T - temperature

u, v - velocity

$\mathbf{u}$ - nodal displacement vector

U_G - grid velocity

V - cell volume

Vol - casting volume

U_{in} - inlet velocity (Chapter 4)

x, y - co-ordinate axes

Greek Symbols

α	- coefficient of thermal expansion of solid (Chapter 2)
α	- indicates fluid region ($\alpha = 1$) and free suface region ($\alpha = 0$) (Chapter 4)
β	- coefficient of thermal expansion of liquid
$\delta_{i,j}$	- Kronecker delta
δg	- air gap width
χ	- temporary variable (Chapter 4)
η	- function defining free surface shape (Chapter 4)
η_t	- contact fraction of top wall interfacial area at mold–casting interface (Chapter 4)
η_w	- contact fraction of side wall interfacial area at mold–casting interface (Chapter 4)
ϵ	- emissivity (Chapter 2)
ϵ	- strain (Section 2.3)
ϵ	- energy dissipation (Chapter 3)
Γ	- diffusive coefficient
ρ	- density
ϕ	- general variable
σ	- Stefan-Boltzmann constant
σ	- stress (Section 2.3)
$\sigma_{h,t}$	- constant in the K–ϵ model
$\sigma_{K,t}$	- constant in the K–ϵ model
$\sigma_{\epsilon,t}$	- constant in the K–ϵ model
ς	- under–relaxation factor
τ	- shear stress on the fluid surface
Θ	- residual errors
ξ	- axial variable in the transformed space
μ	- dynamic viscosity

ν	- kinamatic viscosity (μ/ρ)
ν	- Poison's ratio (Section 2.3)

Subscripts

α	- alpha phase
β	- beta phase
c	- indicates ceiling of the mold cavity (Chapter 2)
e	- equivalent (Section 2.3)
eff	- effective
F	- denotes fluid containing neutrally buoyant particles (Section 4.2)
$false$	- false source
$fill$	- filling
hyd	- hydrostatic
gap	- used with time to indicate gap formation time
i, j, k	- tensor indices
i, k	- co-ordinate indices
l	- liquidus
l	- upper limit of fluid region (Chapter 4)
$L1$	- used with Q to indicate latent heat release between liquidus and solidus temperatures (Chapter 2)
$L2$	- used with Q to indicate latent heat release at the solidus temperature plateau (Chapter 2)
lam	- laminar
$mold$	- used with temperature to indicate mold temperature
n, s, e, w	- north, south, east, west
o	- initial
P	- denotes neutrally buoyant particle (Section 4.2)
$pour$	- used with temperature to indicate pour temperature
ref	- reference value
s	- solidus

s	- upper limit of free surface region (Chapter 4)
t	- turbulent
$TOT1$	- used with Q to indicate sensible heat release between liquidus and solidus temperatures (Chapter 2)
w	- indicates side walls of the mold cavity (Chapter 2)
x	- indicates direction
y	- indicates liquid metal surface (Chapter 2)
yc	- used with F to indicate shape factor between liquid metal surface and mold cavity ceiling
yw	- used with F to indicate shape factor between liquid metal surface and mold cavity walls
$1, 2, 3$	- principal stress directions
ϕ	- denotes association with appropriate variable ϕ

Superscripts

$'$	- indicates fluctuating component (Chapter 3)
$'$	- indicates transformed space (Chapter 4)
n	- cycle counter (Chapter 2)
m	- cycle counter (Chapter 2)
o	- previous iteration
$*$	- half time step temperatures (also used for effective heat transfer coefficient)

Acknowledgements

I would like to express my sincere gratitude to my supervisor, Professor M. Salcudean, who has been a constant source of enthusiasm, encouragement and guidance throughout the course of this study. Professor Salcudean has been an esteemed mentor to me for a number of years and I consider myself very fortunate to have benefited from her intellect, knowledge and experience.

I would also like to express my appreciation to my co–supervisor, Professor M. Munro, for the interest shown in this work. His suggestions and comments have contributed much to the preparation of this thesis.

I would like to thank Dr. K. Davis for many hours of discussion, useful suggestions and the experimental measurements carried out at the EMR laboratories. Dr. Davis has been a valuable source of information about the metallurgical aspects of permanent mold casting processes. Thanks are also due to Del Maeda for the *Pb–Sn* experimental work and to Micheal Keating for setting up the flow visualization experiments.

Financial support for this research has been provided by the Department of Energy, Mines and Resources, and the Natural Science and Engineering Research Council of Canada.

This work is dedicated to my wife, Ayesha, and to my parents for their loving support, patience and confidence.

Chapter 1

INTRODUCTION

Computer–aided techniques are important to the design and production of castings for economic and practical reasons. Canada's foundries serve over 90% of the durable goods industry, and have net annual sales of over 1.5 billion dollars [30,91]. Traditionally, casting techniques have been left to skilled and experienced foundrymen, however, if the industry is to maintain its position in an increasingly competitive market these skills will have to be supplemented with a more scientifically based approach.

In a typical casting process, liquid metal is poured into a mold, solidification takes place and the casting is ejected from the mold. The molds are usually made of sand or metal. Metallic (or permanent) molds are becoming more common as the equipment and procedures needed to reduce environmental hazards associated with sand molds are becoming increasingly expensive. Also, the dimensional consistency and surface finish obtainable with metallic molds reduce the requirements for expensive final machining and finishing operations.

In the present work, fluid flow and heat transfer during permanent mold casting processes are mathematically and experimentally investigated. An engineering

benefit of the work is that the mathematical models can be subsequently used as part of a series of CAD packages for casting design.

1.1 Description of the casting cycle

The permanent mold casting cycle can be divided into two main stages from the heat transfer point of view:

1)The filling stage

This stage extends for the period during which the liquid metal is poured into the mold. It is usually neglected completely in the literature [13,49,64,65,114,132] and an assumption of 'instantaneous' filling is made. In reality, this stage is important because:

1. Significant convection is induced in the liquid metal by the incoming jet. This affects the temperature and solute distribution in the liquid metal [3,59].

2. The finite time period required during filling causes the liquid metal to be in contact with the bottom region of the mold for a longer period of time than the top. This causes asymmetry in the temperature distribution in the mold which increases the thermal stresses, possibly reducing mold life [99]

3. Solidification often occurs close to the mold walls during pouring because of the large temperature difference between the mold and the liquid metal.

4. The velocity and temperature distributions at the end of the filling stage provide the correct initial conditions for the solidification stage.

2)The solidification stage

In this stage the cooling and solidification of the liquid metal takes place. Natural convection occurs in the liquid metal. The flow pattern depends on the velocity field initially generated during the filling stage. Solidification continues and the solidus front advances into the liquid metal. Pure metals solidify isothermally, and alloys solidify over a range of temperatures (called a *mushy* region) bounded by the solidus and liquidus temperatures. A gap forms at the mold–casting interface because the casting contracts and the mold expands thermally. Heat transfer at the interface is a complex phenomenon, consisting of radiation, conduction through the air in the gap and conduction at spot contacts. The metal shrinks during phase change, and if fresh liquid metal is not available to account for the shrinkage, a cavity or a porous area forms inside the casting. The casting is usually ejected from the mold once a thick enough shell of solidified metal has formed to contain the liquid core.

1.2 Literature review

Numerical techniques presently available can solve a large variety of problems in the areas of permanent molding, conventional casting, diecasting and continuous casting. Detailed reviews of the published literature are presented in [2,97]. The objective in this section is to review some of the literature relevant to the heat transfer and liquid metal flow aspects of casting processes.

1.2.1 Modelling of conduction heat transfer

Conduction is the dominant mode of heat transfer in metals because of their low Prandtl number. As the simulation of conduction is much simpler than that of convection, the bulk of the modelling effort so far has addressed this area. A number

of numerical techniques are available to solve the transient heat conduction equation. Of these techniques, the finite difference method [83,107], the finite element method [18,133], and recently the boundary element method [8,11] are more common. These are discussed in many texts and publications and therefore will not be described here. In this section an overview of conduction modelling pertaining to casting processes is presented.

Early work was done by Lazardis [64,65], who determined one and two dimensional solutions for the solidification of a semi–infinite slab. The energy conservation equation resulting in the determination of the rate of movement of the interface was expressed in explicit finite difference form. Constant property and isothermal solidification assumptions were made. Pehlke *et al.* [85] and Jeyarajan and Pehlke [54] simulated the solidification of Silicon Brass alloys and Aluminum in sand molds two dimensionally. A modified specific heat approximation was used for latent heat. Davies [22] solved transient heat conduction to determine heat transfer and feeding range in the runners of sand molds. Latent heat was incorporated in an enthalpy formulation. Reddy [92] simulated the solidification of 'V' shaped Al–Cu castings in sand molds. Latent heat release was simulated by a post iterative integration technique. Brody and Stoehr [13] and Stoehr [114] discussed an explicit solution of the conduction equation for casting and welding problems. Clyne [16] developed an explicit finite difference formulation for one–dimensional heat conduction with non–isothermal latent heat release. Ohtsuka *et al.* [81] explicitly simulated heat conduction during solidification of aluminum alloy castings in steel molds. A thermal contact resistance between the casting and the mold was simulated. Zeng and Pehlke [132] simulated heat conduction during solidification of cylindrical brass castings in sand molds. An explicit finite difference method was used. Pouring time was simulated without convection by allowing a stepwise increase in the liquid metal level. Thermal contact resistance and gap formation was simulated. Good agreement with experimental data was obtained.

Marrone *et al.* [73,74] simulated the solidification of 'T' and 'L' shaped steel

castings in sand molds. An explicit finite difference formulation and the Alternating Direction Implicit (ADI) method were used. Jeyarajan and Pehlke [53] also used the ADI method to study the solidification of cylindrical Aluminum alloy castings in sand molds. Low [70] used the ADI Method to solve the heat conduction equation for square and cylindrical ingots. Pouring time and thermal contact resistance were not modelled. Latent heat release was modelled by a modified specific heat method.

Weatherwax and Riegger [130] and Abis [4] used finite element techniques to model three–dimensional solidification of aluminum castings. Latent heat release was simulated by the modified specific heat method. Hong *et al.* [48,49] applied the boundary element method to study solidification. Latent heat was taken into account by a post–iterative temperature adjustment method.

Thomas *et al.* [121] compared the relative performance of finite difference and finite element methods. Analytical solutions of series form were obtained assuming constant values for certain problem parameters. The boundary conditions consisted of fixed temperature (Dirichlet type), and heat flux (Neumann type). The ADI method [84] was used with the finite difference formulation. Three time stepping schemes were evaluated; the first two were three level schemes and the third was the two level Crank Nicholson [19] method. Latent heat release was modelled by the apparent capacity method, in which the heat capacity was evaluated from the enthalpy gradients. The methods were compared on the basis of accuracy, cost and stability. It was concluded that for the test cases considered and for regular geometries the ADI method was the most cost effective, while providing results of comparable accuracy and stability. The finite element methods are far better suited to irregular geometries. The Crank Nicholson scheme was found to be of comparable accuracy to the three step schemes considered. All the methods provided reasonably accurate overall results in the test cases considered.

1.2.2 Modelling convective effects

Convection during pouring and solidification has received less attention than conduction because of difficulties in studying these phenomena. Despite the low Prandtl number, convection heat transfer can be significant in liquid metals [17,39]. Convection also affects the solute distribution in multi–component systems [90], and the grain structure (therefore the properties) of the solidified product [17].

The problem of determining liquid motion in a Newtonian fluid consists of solving the conservation equations for the mass and momentum in the computational domain. Convection occurs during the filling and solidification stages. Some efforts to model convection relevant to casting processes are discussed in the following.

Convection during the filling of the mold

During the filling of molds, the liquid metal flow field is partly bounded by a free surface. The Marker and Cell (MAC), and Volume of Fluid (VOF) methods have been developed by Harlow, Welch, Nichols and Hirt [38,41,42,43,79] to treat such flows. These approaches have been used with explicit convection diffusion codes in which the governing differential equations are discretized by finite difference techniques based on a term by term truncated Taylor Series approximation. In the MAC method each cell in the domain contains massless marker particles which move at the local fluid velocity. The free surface shape is determined from the position of the marker particles. In the VOF method a variable 'F' is defined which indicates the fractional volume of fluid in each cell. The values of 'F' are bounded between 0 and 1; 0 indicating an empty cell and 1 indicating a full cell. The quantity 'F' is convected in a manner similar to the other variables in the domain.

The Courant time step limitation [38] applies to both the MAC and VOF techniques. This restriction does not cause any additional constraints when applied to explicit codes, however an implicit scheme would lose its advantage if the Courant

limitation is required for the surface treatment. This limitation becomes increasingly restrictive with mesh refinement. Also, the methods cannot be used for steady state flows.

Stoehr and Hwang [115] have used the MAC method to predict the flow of liquid metal in rectangular mold cavities. Smith and Wilkes [110] used the MAC method in cylindrical coordinates to simulate the free surface flow of a fluid issuing vertically upwards from the base of a vertical cylindrical cavity. Their results were limited to laminar, very low velocity flow. Many studies [60,61,102,104,119] have assumed a pseudo–frictionless wall instead of modelling the correct surface shape. This assumption does not correctly reflect the pressure and velocity distributions in the region of the free surface and the resulting errors have often been attributed to the turbulence modelling.

Natural convection and solidification

Natural convection occurs in the liquid metal during the period in which the casting solidifies. The Boussinesq approximation [51] (in which density variation is used only to compute the effects of thermal buoyancy forces on the fluid) is often used in modelling natural convection. The main difficulty in the computation of such flows is that part of the flow domain boundary consists of a moving and somewhat arbitrarily shaped solid–liquid interface.

Sparrow *et al.* [112] simulated melting of a solid around a semi–infinite vertical pipe, embedded in the solid and heated above the fusion temperature. The Control Volume Method was used with a coordinate transformation to conform the mesh to the liquid region. The interface position was updated explicitly at the end of each time step, however, during the computations it was assumed to be stationary. It was found that the convection significantly altered the phase front shape.

The stream function–vorticity approach has the advantage that the pressure

is eliminated from the momentum equations and the mass conservation equation is satisfied implicitly. Application of the boundary conditions is, however, less straightforward and extension to three dimensions is not economical. Szekely and Yadoya [120] used the stream function–vorticity approach to compute fluid flow in the continuous casting problem. Turbulence was computed by a one–equation model. The flow patterns were compared with water model studies and reasonable agreement was obtained. Later, Asai and Szekely [7] used the model for the prediction of flow patterns, heat transfer and tracer distribution for the continuous casting of steel slabs. A reasonable agreement was obtained with previously published experimental data for the solidification profiles, however the agreement was much poorer for the tracer dispersion.

Guenigault and Roots [35] studied solidification inside spheres and tubes using the stream function formulation. Isothermal latent heat release was assumed with constant thermophysical properties. Ramachandran *et al.* [90] solved the solidification problem in a rectangular two–dimensional enclosure with adiabatic top and bottom boundaries using a stream function formulation. A coordinate transformation was used to conform the mesh to the liquid region and the Boussinesq approximation was used.

Desai and Kim [26], and Desai *et al.* [25] used the finite element method with the stream function formulation to model the advancing liquid metal front in runner channels and the free convection in molds. The advancing front was modelled by a mesh transformation. The work was done for a two–dimensional domain and laminar flow. Solidification was not modelled.

The problem with mesh transformation techniques is that their use is generally limited to 'quasi one–dimensional' solidification in which the interface is constrained to traverse primarily along one coordinate direction, and is constrained from becoming too convoluted. This is required to conserve the orthogonality and regular distribution of the mesh. Mesh transformation methods are not simple to imple-

ment in existing codes, and have limitations in their scope of application. A simpler approach [128] is to use a regular mesh and impose zero velocities in the solidified regions of the domain. If the solidus–liquidus interface has a convoluted shape it is approximated in a ' stepwise ' manner. An advantage of this formulation is that it can easily be implemented in existing codes. Sindir [108] has shown that a stepwise approximation to a curved boundary can provide results with reasonable overall accuracy, however, the conditions near the boundary are not correctly represented.

The previously discussed works have dealt with isothermal solidification. In practice, the solidification of alloys is more common, where a two phase or 'mushy' zone exists between the solid and the liquid regions. Flow in this zone has also been studied [33,34,72,113].

Stewart and Weinberg [113] and Gabathuler and Weinberg [33,34] have experimentally studied the penetration of liquid metal into the mushy zone for Lead–Tin and Aluminum alloys with Silicon, Copper and Magnesium. Penetration is defined as the depth in the mushy zone, measured from the liquidus interface, to the point at which significant liquid metal flow occurs. Radioactive tracer particles were introduced into the melt and at some time the solidifying sample was quenched. The liquid metal penetration into the mushy zone was then deduced from the distribution of the tracer particles in the quenched sample. The liquid was stirred by a rotating disk at the top. The solid fraction at maximum liquid metal penetration was found to be about 0.37. The penetration of the liquid metal was small when compared to the thickness of the mushy zone and increased slightly with the liquid metal velocity. Water model studies were done to study the interdendritic fluid flow. It was found that liquid penetration was not significantly affected by dendrite size and concentration.

In the following paragraphs, some approaches to treat the computation of convection in mushy zones during solidification modelling are discussed.

Increased viscosity approach

In this approach [1,98,128] the effective viscosity of the fluid in the solidifying region is increased to suppress the velocities. The effective viscosity is coupled to solidification so that it is increased to a very large value as the solid fraction approaches unity. This method suffers from a lack of information about the viscosity variation in the mushy zone and near the freezing point.

Boucheron and Smith [10] used the SIMPLE algorithm and the increased viscosity approach to model fluid flow and heat transfer with solidification for two different cases; the first of a jet impinging normally on a plate, and the second of natural convection in enclosures. For the first case the numerical results were compared with previously published analytical solutions and good agreement was obtained. The performance of the method was found to be much poorer for the case of modelling solidification during natural convection in enclosures.

D'Arcy source approach

Another method, which seems to be especially suited to the modelling of mushy solidification of alloys is the D'Arcy Source Method [1,98,128]. During the solidification of eutectic alloys the formation of dendrites takes place which, it is assumed, causes the mushy zone to behave as a porous medium. The velocity is coupled to the solid fraction, which is inversely related to the porosity. The method is discussed in detail in a subsequent chapter of this thesis. This appears to be a better approach than the increased viscosity method, as it is easier to evaluate porosity rather than viscosity as a function of the solid fraction.

1.2.3 Latent heat formulations

Latent heat treatment is a major aspect of phase change modelling. A comprehensive review of the progress until about 1980 has been published by Lunardini [71].

Other sources of review articles are conference proceedings edited by Lewis, Morgan and Habashi [67], Lewis and Morgan [66], Lewis, Morgan and Zienkiewicz [68], Brody and Apelian [12], Dantzig and Berry [21], Kou and Mehrablan [56], Cheng, Lunardini and Seki [15], and the publications by Voller and Cross [125], Poirier and Salcudean [87], and Salcudean and Abdullah [97].

This section will briefly review some of the 'weak' solutions that are generally used in technical applications. In such weak solutions of boundary value problems it is not necessary to explicitly impose the behavior of the solution near any of the singularities. It is also not necessary to separately consider the liquid and the solid regions: the phases and the shape of the phase front can be determined later from the solution. Weak solutions are important because certain numerical schemes converge to the weak solution of the original boundary value problem, despite discontinuities of the temperature gradient at the phase front [71]. Methods which utilize weak solutions can easily be extended to solve multidimensional problems. Some widely used weak methods are the ' Apparent Capacity ', ' Heat Integration ' and ' Enthalpy ' formulations. A comparison of these and other methods for one and two–dimensional water and liquid metal problems has been published by Poirier and Salcudean [87]. Detailed descriptions are also given in Salcudean and Abdullah [97].

In the Apparent Specific Heat Method [57,71] the latent heat is included in the specific heat of the material. An apparent specific heat is defined in the range of the phase change temperatures to account for the entire enthalpy change, including both the sensible as well as the latent heat. The advantages of this formulation are that it is numerically very economical and very simple to implement. The disadvantages are that it cannot handle isothermal solidification; in fact an excessively large mushy range has to be assumed which does not correctly reflect the physics of the problem. Also, extremely small time steps are required to correctly account for the enthalpy change during solidification. Poirier and Salcudean [87] found that in general this method performed poorly when compared to other formulations.

In the Effective Capacity Method [87] the apparent capacity function is integrated to obtain an effective capacity for each control volume. This technique has been demonstrated for one and two–dimensional cases [87], and can be extended to three–dimensional problems. The method performs significantly better than the other weak formulations. The latent heat is correctly accounted for and the solution is relatively independent of the mushy range. An assumption of a large fictitious mushy range is not required. This solution is generally accurate both globally and locally (near the phase front) for the liquid metal test cases. The results are relatively insensitive to the time step. Some disadvantages of this method are that it is not simple to implement and the numerical integration is considerably more expensive if the temperature gradients in the mushy range are steep. The apparent capacity function varies significantly in the presence of steep thermal gradients, resulting in the requirement for a higher sampling frequency during numerical integration.

In the Heat Integration (or Post Iterative) Method [27,29,95,100] the temperatures of all the nodes are monitored. When the temperature of a node drops below the freezing temperature, it is considered to be undergoing phase change. An accounting for the energy lost by the node at each cycle is set up and at the end of each cycle the nodal temperature is reset to the freezing temperature. The energy lost by the node is monitored until it is equal to the latent heat. At this point a flag is set, indicating that the node has 'solidified'. In the subsequent cycles the temperature of the node is allowed to fall in the usual manner. Some advantages of this method are that it can be used very easily in multidimensional modelling, with isothermal or non–isothermal phase change and arbitrary time step. The method is computationally economical. A disadvantage is that as the phase front is not continuously followed, the results are less accurate near the phase change location. The accuracy of the results depend on the time step. An elaborate system of accounting and indexing has to be maintained for each node.

The Enthalpy Formulation has been widely applied [101]–[126] to treat latent

heat release in heat transfer problems. The basic method consists of writing the transient part of the energy equation in terms of the enthalpy instead of the temperature. A variation between the total (sensible plus latent) enthalpy and temperature is defined, based on the latent heat release characteristics of the phase change material. This variation is in the form of a step function for isothermal solidification. At each time step the new value of the dependant nodal variable (the enthalpy) is computed and the nodal temperature is determined from this value by using the previously defined variation of the enthalpy with temperature.

The enthalpy method is reasonably accurate for metals solidifying over a mushy range [87]. The solution is relatively independent of the time step and mushy range. The method is somewhat more complex and expensive than the other approaches. The computational cost increases rapidly with mesh refinement. This technique performs poorly close to the phase front for isothermal solidification [122,123,124], and the solution oscillates about the phase change temperature. This inaccuracy increases when modelling the phase change of water because of the large ratio of the latent heat to sensible heat.

The Source Based Method has been recently proposed by Voller [127]. In this technique the latent heat is introduced in the source terms of the finite difference expression of the energy equation. The method is discussed in detail in a subsequent chapter of this thesis. The technique has certain similarities to the enthalpy formulation. The method easily adapts to the general algorithms of the TEACH and PHOENICS codes as they are designed to solve nonlinear equations through iterative techniques. The latent heat content is directly coupled to the nodal temperature which produces fairly accurate results, especially for non-isothermal solidification of metals. This formulation, like some of the others discussed previously, suffers from the characteristic limitations of weak methods, *i. e.* it produces an oscillating solution near the phase front for isothermal solidification. The overall accuracy is reasonable, however the solution is less accurate close to the phase front. An advantage of this method is that the value of the solid fraction is explicitly available. This

is required to couple solidification to other phenomena, for example suppression of flow velocities or special interface boundary conditions.

1.3 Scope of the present work

The heat transfer mechanisms during the casting processes are numerous and very complex. Mathematical modelling of these processes can potentially improve the level of understanding and can aid in the design of both the casting and the mold.

The literature search has shown that very little work has been done in the area of modelling the filling stage of the casting cycle. Neglecting the filling stage may be valid if the solidification time is large compared to the filling time, however this is usually not the case in the permanent mold casting cycle. Convection has been neglected in the bulk of the work. This may not be valid for many cases. The solidification of binary alloys (which release part of their latent heat between the liquidus and solidus temperatures and part at the solidus temperature) is not treated. Cast iron is an example of a very commonly used binary alloy. Free surface flows are common during mold filling, however their treatment is limited to very sophisticated (and expensive) transient explicit codes. A commonly used assumption of a frictionless flat surface is usually inadequate, resulting in errors in the pressure distribution and the resulting velocity fields.

In the present study permanent mold casting processes are investigated by mathematical modelling and experimental work. The mathematical models specifically take finite pouring times into account. Latent heat release for binary alloys is simulated. Convection during the filling process and during solidification is modelled. Alternative techniques of treating the phase change are also presented. A new method to treat free surface flows using the Finite Volume Method has been developed and has proven to be useful in other areas of research. The computational

results have been verified against experimental data. The work done during the course of this thesis has been published [1,3,97,98,99,100].

1.4 Arrangement of the thesis

The work contains six chapters:

Chapter 2 describes the development of mathematical models to simulate heat conduction during the solidification of cast iron plates. Conduction based models are a necessary basic step towards the simulation of casting processes because of their simplicity and economy. The models indicate that finite pouring time causes an asymmetry in the temperature distribution in the mold, which results in higher mold stresses. The post–iterative method is extended to treat latent heat release for binary alloys. The computed results are verified against experimental data.

Chapter 3 describes the Finite Volume Method which has been used as a basis of the mathematical modelling in the subsequent chapters.

Chapter 4 develops mathematical models to simulate the fluid flow during filling of molds. A novel technique to model free surface flow is developed. An Eulerian–Lagrangian technique is presented to treat domains which change spatially in time. Experimental data on the flow distribution during filling of a cylindrical container with water is presented and compared with the computed results.

Chapter 5 describes the mathematical modelling of the casting of a cylindrical cast iron ingot in a cast iron mold. The computed results are verified against experimental data.

Chapter 6 summarizes the work, and outlines the contributions, engineering benefits, conclusions and recommendations.

Chapter 2

CONDUCTION MODELLING

2.1 Overview

In this chapter, a mathematical model simulating heat transfer due to conduction is presented. This is a logical approach to solidification modelling, as conduction plays a dominant role in heat transfer during the solidification of metals and its numerical solution is considerably simpler than that of convection.

Computational and experimental work has been carried out to simulate the complete casting cycle from pouring through freezing of a $0.2\,m \times 0.2\,m \times 0.0254\,m$ cast iron plate. This work has been published [3,99,100] and has led to the following contributions:

1. A mathematical model of the heat transfer in the complete mold casting system is presented.

2. Heat transfer at the mold–casting interface is simulated by a model which takes the spot conduction, radiation and conduction through the air into account.

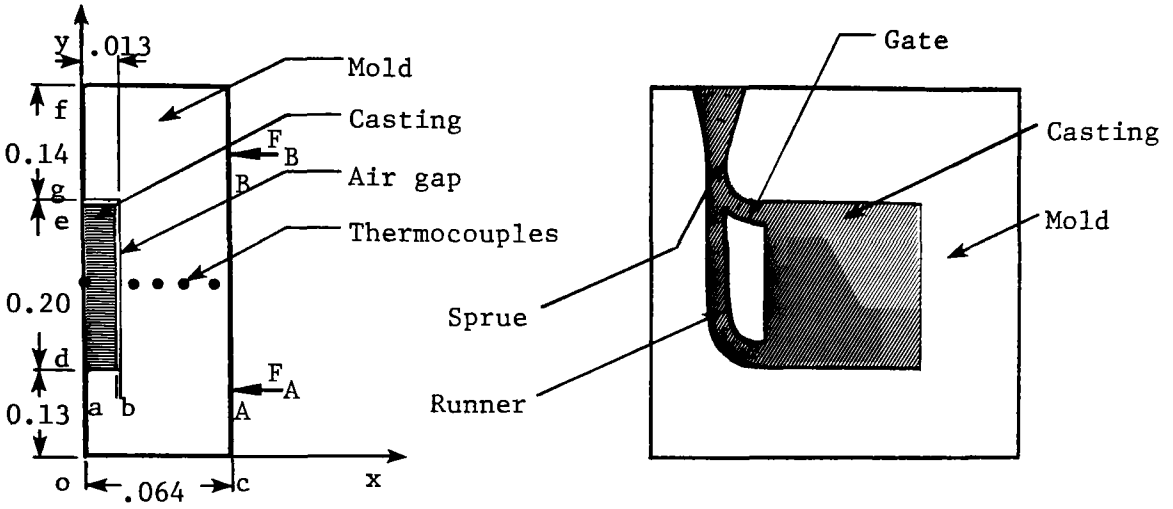

Figure 2.1 Schematic of a mold half showing thermocouple positions and gating arrangement

3. A finite pouring time is taken into account, and its significance is demonstrated.

4. Comparison of the computed results against experimental data is reported.

2.2 Experimental work

Tests were performed[1] in vertically parted cast iron molds, mounted in a horizontal hydraulic press with a closing force of $4450N$. The test casting was a plate measuring $0.2\,m \times 0.2\,m \times 0.0254\,m$, divided evenly between the two mold halves. A schematic diagram of the mold is shown in Figure 2.1. The mold cavity surfaces were sprayed with a thin layer of a commercial ceramic mold-coating material, followed by a graphite layer. In addition, they were sooted with an acetylene flame before each

[1]The experimental work reported in this section was done in collaboration with the personnel of CANMET/PMRL at the Department of Energy, Mines and Resources, Government of Canada.

pour. Gray cast iron containing approximately 3.5% Carbon, 2.5% Silicon and 0.3% Manganese was cast. Gating was from the side (shown in Figure 2.1), either at the top or at the bottom of the mold cavity. Pour time was about 8 seconds. Mold temperatures were measured with chromel-alumel thermocouples with 40 *mil* (1.02 *mm*) O.D. stainless steel sheaths, inserted in close–fitting holes at the positions shown in Figure 2.1. The thermocouples in the casting were shielded by thin–walled silica tubes of 2 *mm* O.D. Temperatures were recorded with a Cyborg Isaac 41A data logger with an accuracy of $\pm 2^{o}C$.

The alloy was melted at $1380^{o}C$ in an induction furnace and tapped into a ladle for pouring. Experimental evidence indicates that a temperature drop of the order of $100^{o}C$, occurred as metal entered the mold and traversed the gating system.

2.3 Mathematical modelling

The development of a mathematical model simulating the solidification of the casting described previously is presented in this section. In the first phase the heat transfer in the casting and the mold is modelled. Temperature distributions are obtained and used as input parameters for the second phase, in which the stresses in the mold are computed. The material properties are taken from reference [6] and shown in Table 2.1. The experimental parameters are specified in Table 2.2. The thermal conductivity and specific heat are functions of temperature [6]

$$c = \begin{cases} 263 + 2.1T - 6.34 \times 10^{-3}T^2 + 7.04 \times 10^{-6}T^3 \ (J/kg^{o}C) & T < 800\,^{o}C \\ 690 \ (J/kg^{o}C) & 800\,^{o}C < T < 1144\,^{o}C \\ 610 \ (J/kg^{o}C) & T > 1144\,^{o}C \end{cases}$$

Table 2.1 Properties of cast iron

Material	Gray Iron
Carbon content	3.5 % (w/o)
Silicon content	3.0 % (w/o)
Manganese content	0.3 % (w/o)
Eutectic (Solidus) Temperature	1144 ^oC
Liquidus Temperature	1250 ^oC
Heat of fusion	$2.1 \times 10^2 KJ/kg$
Liquid density	7200 kg/m^3
Emissivity, ϵ	0.8
μ	$10.19 \times 10^{-3} kg/ms$
β	$1 \times 10^{-4}\ C^{-1}$
Solid density	7300 kg/m^3
Viscosity	$10.19 \times 10^{-3} Kg/ms$
Youngs Modulus	$9 \times 10^{10} Pa$
α	$1 \times 10^{-5}\ C^{-1}$
Poissons ratio	0.3

$$k = \begin{cases} 50.76 - 0.0076T\ (W/m^2\,^oC) & T < 800\,^oC \\ 42\ (W/m^2\,^oC) & 800\,^oC < T < 1144\,^oC \\ 29\ (W/m^2\,^oC) & T > 1144\,^oC \end{cases}$$

Table 2.2 Experimental parameters

Pouring time	8.0 s
Ambient temperature	25 ^oC
Pouring temperature	1275 ^oC
Mold temperature, (T_{mold})	230 ^oC

2.3.1 Phase I, Modelling of heat transfer

Governing equation and assumptions

The differential equation of heat conduction through an isotropic material in two–dimensional cartesian coordinates is written as

$$\nabla k \nabla T + Q = \rho c \frac{dT}{dt} \tag{2.1}$$

The following assumptions are made in obtaining the solution of the above equation:

1. *Liquid metal convection effects resulting through pouring are negligible.*
2. *Heat transfer through natural convection in the liquid metal is negligible.*
3. *During pouring, the liquid metal level rises discretely with time.* The continuous rising of the liquid metal surface is simulated by a stepwise increase in the level.
4. *During pouring, the heat transfer from the liquid metal surface consists of radiation to the top and side walls of the mold cavity.* Natural convection in the air above the liquid metal surface is neglected.
5. *Physical properties such as conductivity and specific heat are temperature dependent; the density is phase dependent.*

6. *The liquidus and solidus temperatures are based on the Iron-Carbon Equilibrium diagram. The effect of Silicon on the Fe-C equilibrium diagram is accounted for by using a 'Carbon equivalent', C_e, equal to* $(C\% + \frac{1}{3}Si\%)$. This is a standard technique of accounting for the effects of Silicon [24]. Manganese has no effect on the liquidus or solidus temperatures [24].

7. *Cast Iron is a hyper-eutectic; it releases part of the latent heat as it cools from the liquidus to the solidus temperature and the rest isothermally at the solidus temperature. Latent heat is released uniformly with temperature in the mushy region. The fraction of the latent heat released between the liquidus and the solidus temperatures depends on the Carbon equivalent.* In the present work this fraction is obtained using the following proportional expressions with the iron carbon equilibrium diagram [24]:

$$(C_{eutectic} - C_e)/(C_{eutectic} - C_\alpha) \quad \text{for } C_e \leq C_{eutectic}$$
$$(C_e - C_{eutectic})/(C_\beta - C_{eutectic}) \quad \text{for } C_e > C_{eutectic}$$

8. *Heat transfer from the mold outside surface to the surroundings is through free convection and radiation.*

Treatment of the mold casting interface

The heat flow from the liquid metal to the mold results in a skin of solidified metal which initially remains in contact with the mold. As solidification continues the casting and the mold may stay in contact at the asperities on the microscopically rough walls, or a gap may form at the mold–casting interface. Gap formation occurs mainly due to (a) expansion of the mold, (b) contraction of the casting, or (c) oxidation of the volatile components of mold coating. The interface heat transfer is a complex combination of spot conduction at the asperities, radiation, and conduction through the air in the gap. Standard correlations describing heat

transfer between rough surfaces in contact are usually not applicable because of the effects of gap formation and the oxidizing mold coatings. The detailed study of the interface heat transfer is still an open area of research, however, it is not within the scope of this study.

In the present work an interface heat transfer model taking the spot conduction, radiation and air conduction into account is used. The model is based on the following assumptions:

1. *Initially the heat transfer between the casting and the mold is through conduction with a thermal contact resistance.* This assumption is valid for the initial period during which the skin of solidified metal is 'thin' and conforms to the mold. A thermal contact resistance value of $1.6 \times 10^{-4} m^2\,^{\circ}C/W$ is used. Davies [23] has reported contact resistance values in the range of $2.0 \times 10^{-4} m^2\,^{\circ}C/W$ to $4.0 \times 10^{-4} m^2\,^{\circ}C/W$ for castings in permanent molds with ceramic and graphite coatings for the period when the mold and casting are in contact.

2. *After a time interval, t_{gap}, a gap is formed between the mold and the casting along the surfaces indicated in Figure 2.1.* The time at which the gap forms, and the locations along the interface where it forms cannot be rigorously established. The location of gap formation is geometry dependant (discussed subsequently in this chapter), as well as a function of a number of other parameters. Gap formation times in the range of 5–15 seconds have been deduced from mold and casting temperature measurements in a number of studies [45,46,80,118].

   In the present study the casting is assumed to 'sit' on the bottom of the mold cavity, therefore no gap formation is assumed at the bottom surface. It is assumed that a gap forms between the top surface of the casting and the mold instantaneously. A gap formation time of 10 seconds is assumed for the side wall and its influence on the total solidification time is investigated.

3. *After gap formation, the heat transfer is by radiation and conduction through the air and local regions of contact.* The fraction of the wall area in contact is very difficult to estimate, as it depends on the geometry, material properties, wall temperatures and mold coating. In the present study it is assumed that approximately 3% of the side area of the casting is in contact with the mold after gap formation. No thermal contact is assumed between the casting and the mold at the top surface after gap formation.

4. *The gap width is 2mm during the casting cycle.*

   The gap width is less critical than the other parameters as it only influences the heat conduction through the air in the gap. It will be shown subsequently that conduction through the air is very small as compared to radiation and spot conduction. The Grashof number for the air in the interface is on the order of 10^{-1}, and therefore convection is insignificant. Ho and Pehlke [45] have measured gaps widths of approximately 1 mm by installing linear transducers in mold and casting (under unidirectional solidification).

Initial conditions

At time $t = 0$, the initial conditions are imposed as (Figure 2.1):

Medium

Air for $o \leq x < b$

$d < y < e$

Cast iron for $o \leq x \leq b$ and $b \leq x \leq c$

$o \leq y \leq d$ $\quad o \leq y \leq f$

$e \leq y \leq f$

Temperature

$$T = T_{mold} \quad \text{for} \quad o \leq x \leq c$$
$$o \leq y \leq f$$

Boundary conditions

During the pouring of liquid metal in the mold the liquid metal surface exchanges heat through radiation with the top and side walls of the mold cavity. Hence:

$$-k_{Liquid\ metal}\frac{\partial T}{\partial y}\bigg|_{d<y<e} = F_{yw}\epsilon\sigma(T_y^4 - T_w^4) + F_{ye}\epsilon\sigma(T_y^4 - T_c^4) \tag{2.2}$$

where 'y' is the level of the liquid metal surface at time 't' during pouring and F_{yw}, F_{ye} are radiation shape factors.

Before gap formation, a thermal resistance, R, due to mold coating and contact between the casting and mold is assumed. The heat flux across the mold casting interface for $0 \leq t \leq t_{gap}$ is written as:

$$q = \frac{A}{R}(T_c - T_m) \tag{2.3}$$

where T_c and T_m are the casting and mold wall temperatures respectively, at the mold casting interface.

The convective heat transfer in the liquid metal is ignored as stated earlier. After gap formation, the heat transfer is due to radiation, conduction through the air and conduction at local points of contact.

$$-k_{Casting}\frac{\partial T}{\partial x}\bigg|_{x=a} = h^*(T_b - T_a) + F\epsilon\sigma(T_b^4 - T_a^4) \tag{2.4}$$

$$-k_{Casting}\frac{\partial T}{\partial y}\bigg|_{y=g} = h^*(T_e - T_g) + F\epsilon\sigma(T_e^4 - T_g^4) \tag{2.5}$$

where h^* is an equivalent heat transfer coefficient taking into account the spot conduction and conduction through the air gap. T_b and T_e are the temperatures at the walls of the casting, and T_a and T_g are the temperatures at the walls of the mold (see Figure 2.1).

Latent heat treatment

The latent heat of fusion is released in the liquidus–solidus temperature range and is taken into account by the post–iterative method. In this work the technique is extended to treat binary alloys. This method is implemented as follows:

1. The latent heat content of cast iron is divided into two parts; the first part, Q_{L1}, is released as the metal cools from the liquidus temperature, T_l, to the solidus temperature, T_s, and the second part, Q_{L2}, is released isothermally at the solidus temperature, T_s. The ratio of the magnitudes of these two parts is based on the carbon equivalent for the alloy. The total sensible plus latent heat release between the liquidus and the solidus temperatures is

$$Q_{TOT1} = \{Q_{L1} + c_{i,k}(T_l - T_s)\}\rho_{i,k}\Delta x_i \Delta y_k \tag{2.6}$$

2. Freezing of node i,k is considered to begin at the $(n+1)$th cycle when the temperature of the node $T_{i,k}$ drops below T_l, or

$$T_{i,k}^{n+1} < T_l < T_{i,k}^{n} \tag{2.7}$$

3. An energy budget is set up for the node i,k until the $(n+m)$th cycle when solidification is completed. The total energy, $E_{i,k}$, released by the node i,k from the time that the temperature dropped from the liquidus temperature is given as:

$$E_{i,k}^{n+1} = (T_{i,k} - T_l)c_{i,k}\rho_{i,k}\Delta x_i \Delta y_k \tag{2.8}$$

$$E_{i,k}^{n+j} = E_{i,k}^{n+1} + \sum_{j=2}^{m}(T_{i,k}^{n+j-1} - T_{i,k}^{n+j})c_{i,k}\rho_{i,k}\Delta x_i \Delta y_k \tag{2.9}$$

4. As long as $E_{i,k}^{n+j} \leq Q_{TOT1}$, the node is in the mushy region. The latent heat Q_{L1} is assumed to be released uniformly between the liquidus and the solidus temperatures. The temperature of the node is recomputed as:

$$T_{i,k} = T_l - \frac{E_{i,k}^{n+j}}{Q_{TOT1}}(T_l - T_s) \tag{2.10}$$

5. When $Q_{TOT1} < E_{i,k}^{n+j} \leq (Q_{TOT1}+Q_{L2})$ the eutectic arrest is simulated through the isothermal release of the second part of the latent heat. At the end of each cycle the temperature of the node is set as:

$$T_{i,k} = T_s \tag{2.11}$$

6. Solidification is considered to be completed at the $(n+m)$th time step when

$$E_{i,k}^{n+m} > (Q_{TOT1} + Q_{L2}) \tag{2.12}$$

At this time step the temperature of the node is computed as:

$$T_{i,k}^{n+m} = T_s - \frac{E_{i,k}^{n+m} - Q_{TOT1} - Q_{L2}}{c_{i,k}\rho_{i,k}\Delta x_i \Delta y_k} \tag{2.13}$$

At this stage a flag is set, indicating that the node has solidified. In subsequent cycles the temperature of the node is allowed to drop in the normal manner.

Mold filling

The mold is filled by gating the liquid metal from the side at the top or at the bottom of the cavity. In the present study, the continuous rising of the liquid metal is simulated in a stepwise manner. The computational domain is discretized as shown in Figure 2.2(a). The casting is considered to be composed of a number of horizontal 'layers' of cells. Each layer of cells represents a certain depth of the poured liquid metal, with which a certain 'filling time' is associated, based on the total pour time of the casting and the assumption of uniform filling rate. Initially, all the cells corresponding to the casting are assigned properties of air and temperature equal to the initial mold temperature. The practices of top and bottom gating are numerically simulated as follows.

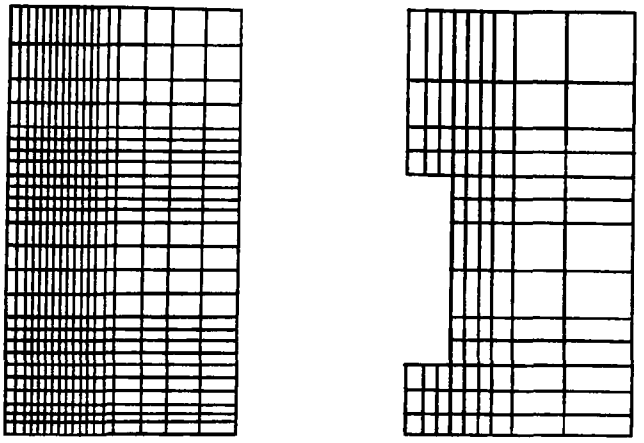

Figure 2.2 Mesh used in the solution

Top Gating

The elapsed time since the beginning of the process is monitored. When this time equals or exceeds the 'filling time' associated with a particular layer of cells, the physical properties associated with the cells in that layer are changed to those of liquid cast iron and the temperatures are set to the pouring temperature. In this manner, successive layers of cells, starting from the bottom layer are 'activated' or 'filled' as time progresses. The top layer is the last layer to be filled at the pour time after which the modelling of the pouring process is considered to be completed.

Bottom Gating

When the elapsed time exceeds or equals the 'filling time' of the first layer of cells at the bottom of the casting, that layer is 'activated' as discussed previously. When the elapsed time exceeds or equals the filling time of the second layer of cells from the bottom of the casting, the following steps are taken:

1. The enthalpies (as well as all the associated indexing and tracking information about latent heat released, etc.) corresponding to the bottom layer are

transferred to the second layer from the bottom.

2. The indices, properties and temperatures of the cells in the bottom layer are reset to those corresponding to liquid metal at pouring temperature.

When the elapsed time exceeds the 'filling time' for the third layer from the bottom this process of transferring the enthalpies and indexing is carried out from the second layer to the third layer and from the first layer to the second layer. The indices, properties and temperatures of the bottom layer are once again reset to those corresponding to liquid metal at pouring temperature. This process is repeated for each successive layer of cells at their particular filling times. When the top layer is filled at the pour time, the modelling of the pouring process is considered to be completed. During the pouring process, radiation heat transfer from the surface of the liquid metal to the top and side walls of the mold cavity is also modelled. The mixing of the liquid metal due to the effects of the inlet jet and natural convection is neglected.

Numerical procedures

The governing differential equation (2.1) is expressed in finite difference form using forward difference for the time variable and central difference for the second order space derivatives. The Alternate Direction Implicit (ADI) method [84] is adopted as the solution procedure. The method is unconditionally stable [84,107,121] and is considerably more economical than other techniques [121]. The 20×28 mesh used is shown in Figure 2.2(a). Computations were done previously on a 16×25 mesh [100] and no significant mesh dependence was observed either in the total solidification time or the mold temperature distribution. Over the first half time step the finite difference equations are expressed implicitly in the x-direction and explicitly in the y-direction. In the second half time step the procedure is reversed and the equations are formulated explicitly in the x-direction and implicitly in the

y-direction. These formulations over the two half time steps are shown by equations (2.14) and (2.15), respectively.

$$\begin{aligned} k_{i-1,i}\Delta y_k \frac{(T^*_{i-1,k} - T^*_{i,k})}{(\Delta x_{i-1} + \Delta x_i)/2} &+ k_{i,i+1}\Delta y_k \frac{(T^*_{i+1,k} - T^*_{i,k})}{(\Delta x_i + \Delta x_{i+1})/2} + \\ k_{k-1,k}\Delta x_i \frac{(T^n_{i,k-1} - T^n_{i,k})}{(\Delta y_{k-1} + \Delta y_k)/2} &+ k_{k,k+1}\Delta x_i \frac{(T^n_{i,k+1} - T^n_{i,k})}{(\Delta y_k + \Delta y_{k+1})/2} \\ &= \rho_{i,k} c_{i,k} \Delta x_i \Delta y_k \frac{(T^*_{i,k} - T^n_{i,k})}{\Delta t/2} \end{aligned} \tag{2.14}$$

$$\begin{aligned} k_{i-1,i}\Delta y_k \frac{(T^*_{i-1,k} - T^*_{i,k})}{(\Delta x_{i-1} + \Delta x_i)/2} &+ k_{i,i+1}\Delta y_k \frac{(T^*_{i+1,k} - T^*_{i,k})}{(\Delta x_i + \Delta x_{i+1})/2} + \\ k_{k-1,k}\Delta x_i \frac{(T^{n+1}_{i,k-1} - T^{n+1}_{i,k})}{(\Delta y_{k-1} + \Delta y_k)/2} &+ k_{k,k+1}\Delta x_i \frac{(T^{n+1}_{i,k+1} - T^{n+1}_{i,k})}{(\Delta y_k + \Delta y_{k+1})/2} \\ &= \rho_{i,k} c_{i,k} \Delta x_i \Delta y_k \frac{(T^{n+1}_{i,k} - T^*_{i,k})}{\Delta t/2} \end{aligned} \tag{2.15}$$

In equation (2.14), over the first half time step, the T^* are unknown and T^n are known from the preceding time step or initial conditions. Over the second half time step, the T^* in equation (2.15) are known and the T^{n+1} are unknown. Hence, successive applications of equation (2.14), followed by equation (2.15) give the new temperature field after an elapse of time Δt. Equations (2.14) and (2.15) each contain three unknowns. The resulting system of tri–diagonal equations can be solved very efficiently. A computer program was developed based on this method to calculate the temperature distributions, heat transfer coefficients and solidification front progress as functions of time.

2.3.2 Phase II, Modelling of thermal stresses

In this phase a mathematical model is developed to simulate the thermal stresses in the mold.

Governing equations and assumptions

The governing equations (in tensorial notation) are the equilibrium equations:

$$\sigma_{ij,j} + b_i = 0 \tag{2.16}$$

and the compatibility equation:

$$\epsilon_{ij,km} + \epsilon_{km,ij} - \epsilon_{ik,jm} - \epsilon_{jm,ik} = 0 \tag{2.17}$$

The stress strain relations are given by:

$$\epsilon_{ii} - \alpha T = \frac{1}{E}\left[\sigma_{ii} - \nu\left(\sigma_{jj} + \sigma_{kk}\right)\right] \tag{2.18}$$

$$\epsilon_{ij} = \frac{2}{E}\sigma_{ij}(1+\nu) \tag{2.19}$$

The Von Mises equivalent stress is defined as:

$$\sigma_e = \frac{1}{4}\sqrt{(\sigma_1 - \sigma_2)^2 + (\sigma_2 - \sigma_3)^2 + (\sigma_3 - \sigma_1)^2} \tag{2.20}$$

The governing equations are solved by the finite element method using a previously developed thermal stress analysis code [103] featuring eight node isoparametric rectangular elements. The following assumptions are made.

1. *Plane strain analysis is valid.*
2. *The stresses are in the elastic range.*
3. *The material properties are independent of temperature.*
4. *At time, $t = 0$ the mold temperature is uniform.*

The mold is discretized into 99 elements as shown in Figure 2.2(b). The mechanical properties of the cast iron mold are given in given in Table 2.1. The system of equations in matrix form is:

$$[\mathbf{K}]\{\mathbf{u}\} = \{\mathbf{F}\} \tag{2.21}$$

where **K** is the global stiffness matrix, **u** is the nodal displacement vector and **F** is the force vector. The thermal strains are determined and converted to equivalent nodal forces, which are then assembled into the force vector. The solution of the above equation yields the nodal strains from which the stresses are determined.

Initial conditions

The mold is preheated to prevent premature solidification of the liquid metal. A uniform initial temperature distribution is assumed. Therefore:

$$T = T_{mold} \quad o \leq x \leq b \quad \text{and} \quad b \leq x \leq c$$
$$o \leq y \leq d \qquad o \leq y \leq f$$
$$e \leq y \leq f$$

Boundary conditions

The mold consists of two symmetric halves pressed together with a force of 4450 N (transmitted through four bolts). The 'x'–displacement is constrained to zero at the vertical symmetry axis where the mold halves meet. The 'y'–displacement is constrained to zero at the location where the bottom bolt is attached to the mold (Location 'A' in Figure 2.1). Therefore

$$F_A = 2225\ N \qquad x = c;\ y = h$$

$$F_B = 2225\ N \qquad x = c;\ y = g$$

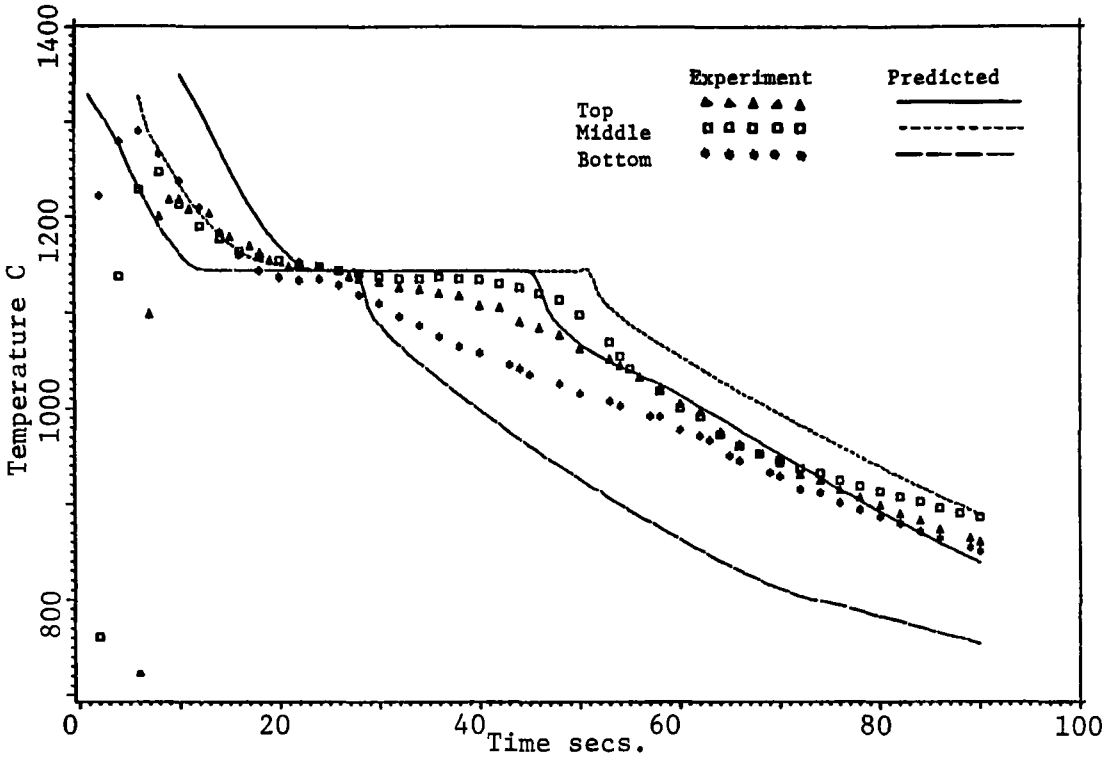

Figure 2.3 Temperatures at the center of the casting (Top gating)

$$\text{x displacement} = 0 \quad \text{at} \quad x = 0;\ y = d, g$$

$$\text{y displacement} = 0 \quad \text{at} \quad x = c;\ y = d$$

2.4 Results and discussion

2.4.1 Temperature distribution

Top Gating

In Figure 2.3 the initial temperature drop and the plateau represent respectively, liquid cooling and eutectic solidification. The effect of a finite pour time is reflected by earlier solidification at the bottom, shown both in the computed and actual cooling curves. It is noted that the eutectic arrest is not so flat as predicted. The

most likely reason is the assumption in the model that the phase diagram for cast iron can be taken as pseudo-binary between iron and a 'carbon equivalent' equal to $C\% + 1/3Si\%$. This is an approximation to the true diagram, which has an $Fe - C - Si$ ternary eutectic trough. The 0.3% Mn further modifies the diagram. The agreement between computed and observed solidification times is reasonable at the bottom and middle positions, however, at the top of the casting solidification is completed faster than predicted. The difference can be explained by the assumption in the model that fresh metal at the pour temperature is continuously being added to the top of the metal as it rises in the mold cavity during the pour. Convective stirring by the metal stream entering the gate is ignored. Such stirring brings cooler metal from within the casting up to the top surface, reducing the solidification time at the casting top. The relatively hotter metal going into the lower regions of the casting may be one of the causes of the experimental temperatures at the bottom being higher then the computed values.

The final temperature drop represents post-solidification cooling of the casting. The predictions of the model for this stage are reasonably accurate at the top and middle positions. In both cases the predicted curves are somewhat more flat than the actual curves. It is probable that the assumption of a gap width at the mold–casting interface that is constant with time becomes inaccurate in the later stages of cooling when the solidified casting shrinks away from the mold walls. Cooling is then slower than predicted. At the bottom of the casting, the observed post–solidification cooling is far slower than predicted, which can be explained as follows. The model assumes that the bottom of the casting is always in contact with the mold. With a top side gate, however, solidified metal in the gate will hold the casting close to the top surface of the mold cavity, and the bottom of the casting will be pulled away from the mold as the casting shrinks, reducing heat loss from the bottom of the casting.

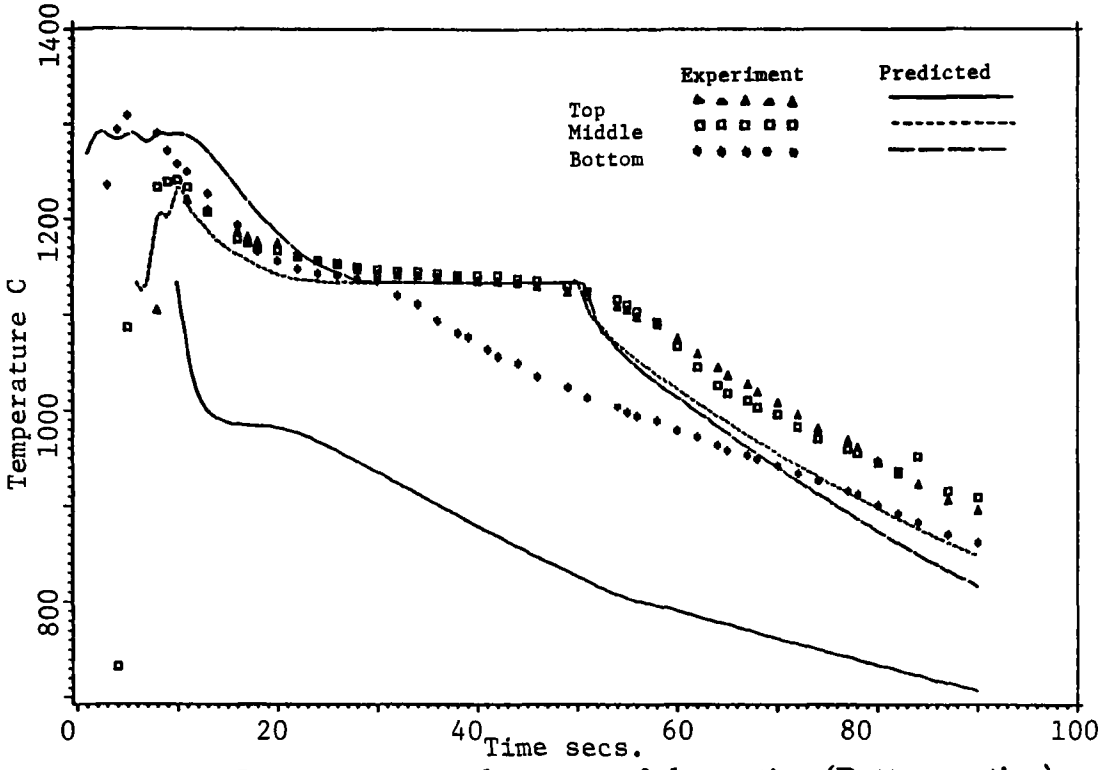

Figure 2.4 Temperatures at the center of the casting (Bottom gating)

Bottom Gating

In Figure 2.4, the agreement between observed and computed temperatures at the middle of the casting is satisfactory, with the same small differences as noted for the top-gated case. There are, however, large discrepancies both at the top and the bottom of the casting. The computed cooling curves for the middle and bottom of the casting are very close to one another but the experimental data indicates that the bottom cools at a much greater rate than the middle.

The present model for bottom gating assumes that hot metal is introduced at the base of the mold cavity, and cooling takes place as it is displaced upwards during filling. Metal at the top will then have a low temperature when it reaches its final location, and solidification will take place early. Solidification at the bottom, in contrast, is delayed according to the model by the influx of hot metal. There is in fact little difference between the observed temperatures at the top and middle of

the casting, and the bottom region is the first to freeze.

General comments

Comparison between the experimental cooling curves shown in Figures 2.3 and 2.4 shows that there is little difference between the top gated and bottom gated cases. The main difference is that the top solidifies faster with top gating, an initially surprising result. It appears that for both gating systems convective stirring is sufficient to remove most of the temperature differences within the liquid soon after the mold is filled. As soon as a solidified shell has formed, the top gate raises the casting from the bottom of the mold cavity, slowing solidification at the casting bottom. When gated at the bottom, the casting is held at the bottom of the mold cavity and a gap opens at the top, slowing solidification at the top.

In summary, reasonable agreement has been obtained between observed and computed cooling curves in the central region of the casting for both top and bottom gating. Agreement between actual and computed temperatures at the top and bottom of the casting during solidification and post-solidification cooling is less satisfactory. The discrepancies have two main causes. First, differences in temperature within the liquid metal in the mold cavity both during and after pouring are exaggerated in the model because convective stirring is not allowed for. Second, the position of the gates can have an important influence on the casting–mold gap width, in effect keying the casting against certain mold cavity surfaces once a sufficiently strong solidified shell has formed. The air gap width is assumed to be constant but in reality it is a function of both position as well as time.

Temperature distribution in the mold

Figure 2.5 shows the thermal contours in the mold. Asymmetry of the temperature distribution due to finite pouring time was observed for both top as well as bottom

gating. The liquid metal remains in contact with the bottom of the mold cavity longer than the top, hence temperatures in the bottom region of the mold are higher, as shown for the case of top gating in Figure 2.5.

Figure 2.6 illustrates the computed and measured temperatures in the mold at the thermocouple locations shown in Figure 2.1. It can be seen that the predicted results agree well with the measured values at the mid-height of the mold cavity. This agreement is consistent with the results presented in Figure 2.3 where a reasonable agreement between the predicted and measured temperatures is shown at the mid-height of the casting. It can be seen that initially very steep temperature gradients exist in the mold which diminish rapidly with time.

Solidification time and interface heat transfer

Figure 2.7 shows the effects of gap formation time and thermal contact resistance (before gap formation) on the total solidification time. In the present simulation it is assumed that the gap at the top surface of the casting forms instantaneously and the gap at the side forms at time 10 seconds after pouring begins. As can be seen, the gap formation time has a significant effect on the solidification time. The value of the thermal contact resistance before gap formation also affects the solidification time, but to a lesser extent.

Figure 2.8 shows the variation of the gap heat transfer coefficient as a function of time. The gap heat transfer consists of conduction through the air, radiation across the gap and conduction at local points of contact. In the present model the values of the conduction through air and through local points of contact is constant because the gap width and spot contact area are assumed to remain constant with time. The radiative component of the gap heat transfer coefficient drops as the surface temperature of the casting decreases. A wide range of gap heat transfer coefficient values ($200 W/m^2\,^oC$–$2000 W/m^2\,^oC$) are reported in the literature [45,46,80,118]

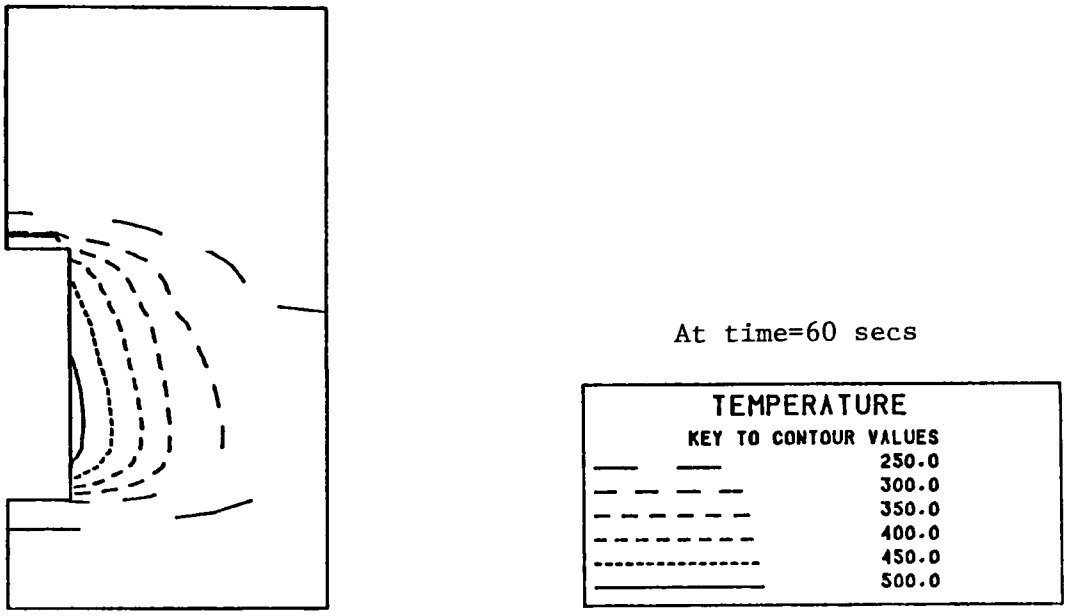

Figure 2.5 Thermal contours in the mold (Top gating)

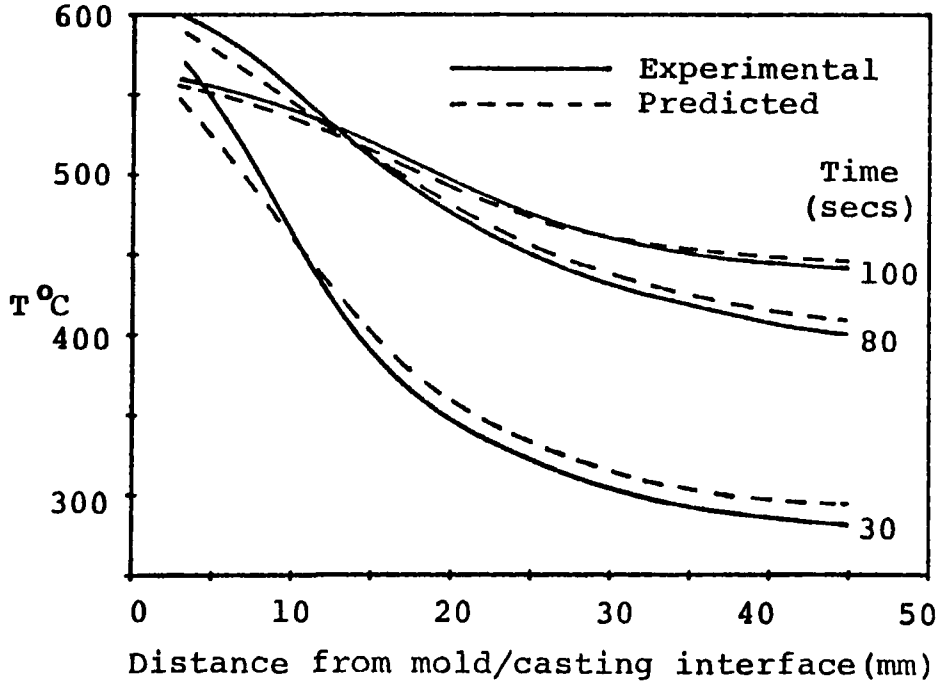

Figure 2.6 Temperature distribution in the mold (Top gating)

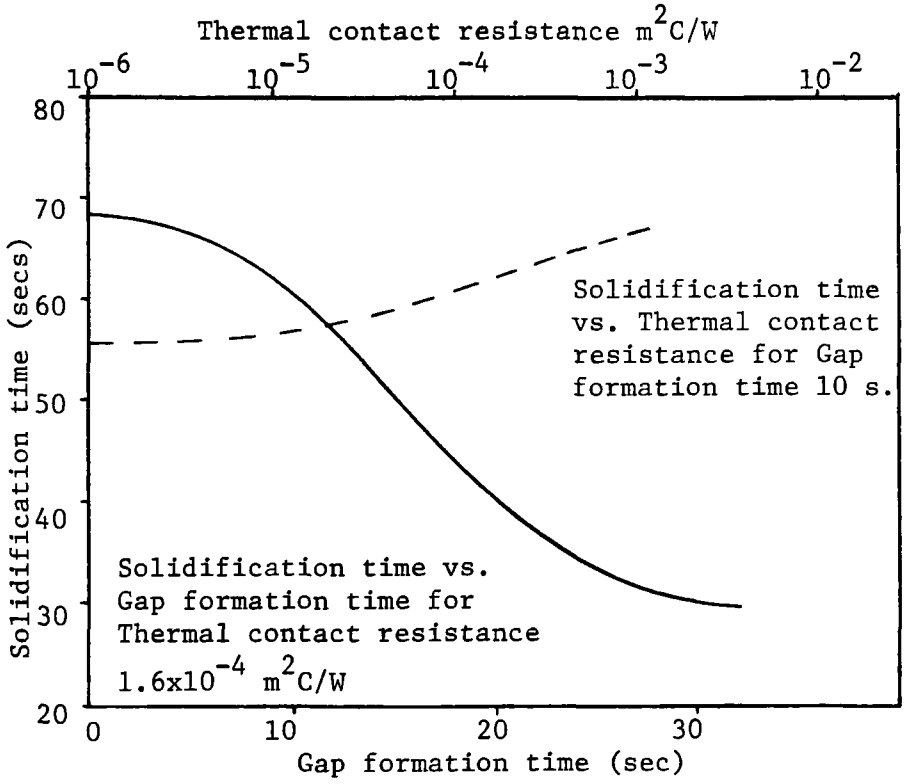

Figure 2.7 Solidification time vs. thermal contact resistance and gap formation time

which illustrates the dependence of the interface heat transfer to the various problem parameters. The values reported by Sully [118] are of particular interest as they are for $0.02\,m$ thick grey cast iron plates vertically cast in permanent cast iron molds. Their experimental heat transfer coefficient values are also plotted in Figure 2.8. The results of Nishida and Matsubara [80], obtained for $0.05\,m$ diameter aluminum castings in a steel mold are also presented. It can be seen that the interface heat transfer coefficient values predicted by the present model are very close to those measured experimentally for similar casting processes.

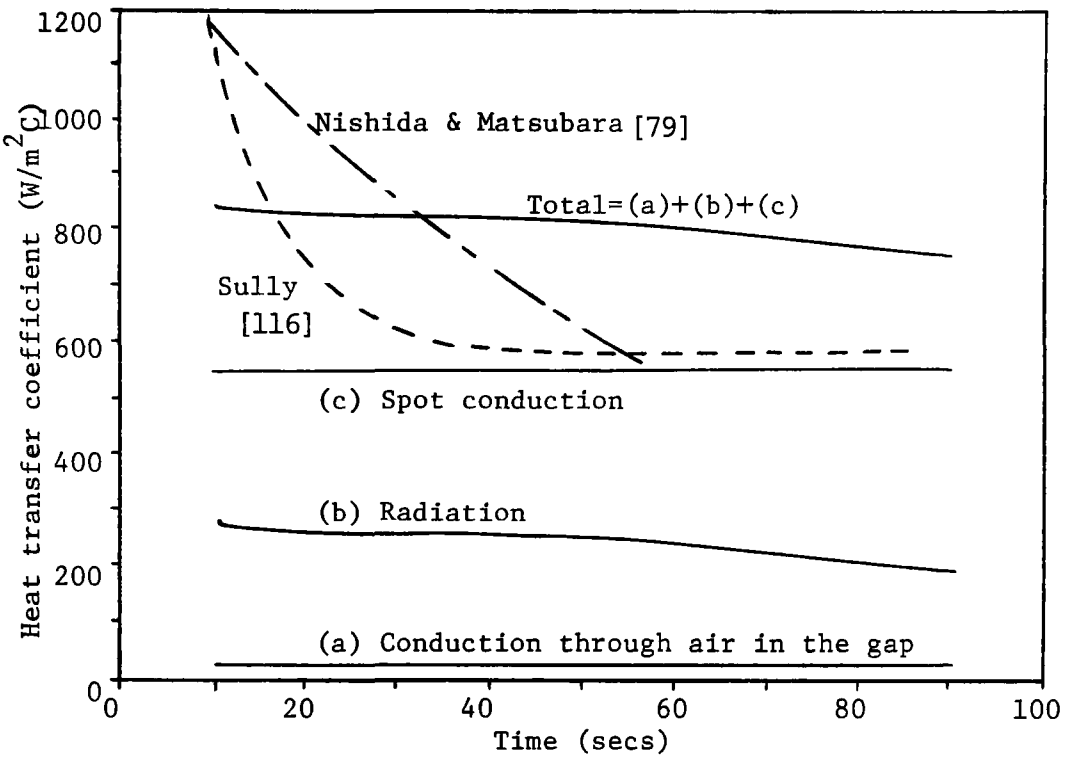

Figure 2.8 Components of the gap heat transfer coefficient

2.4.2 Thermal stress distribution

Figure 2.9 illustrates the stresses present in the mold at times 20 seconds and 50 seconds after pouring. The stress contours for top gating are shown in Figure 2.9 (a) and (c). The asymmetry of the stress contours due to finite pouring time can be observed. Similar results were obtained for the simulation of bottom gating. It is concluded that the reason for this asymmetry is pouring time, rather than gating techniques. Due to a finite pouring time the liquid metal remains in contact with the bottom part of the mold longer than the top, hence mold temperatures and thermal stresses in the bottom region are higher. It can be seen from Figure 2.9 (c) however, that the temperature contours are nearly symmetrical and the pouring time effects are not significant about 50 seconds after pouring.

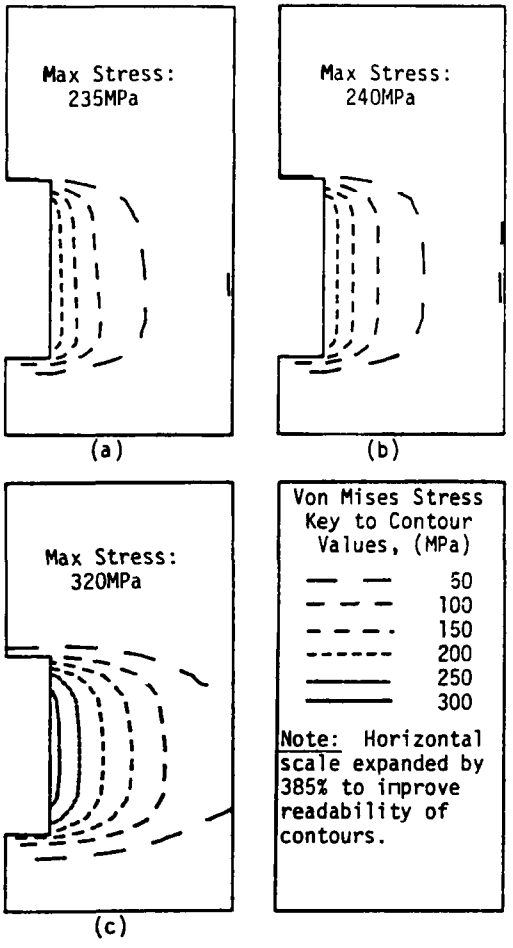

(a) At 20 s. (Gated at the top)
(b) At 20 s. (Zero pouring time)
(c) At 50 s. (Gated at the top)

Figure 2.9 Thermal stress contours

The thermal stresses are computed on the basis of the temperature distributions presented in the previous section. Figure 2.6 shows that the computed mold temperatures are reasonably accurate at the mid-height of the mold cavity, however a similar verification cannot be made at the top and bottom regions. Comparing the stress contours in Figure 2.9 with the thermal gradients in Figure 2.6, it may be seen that higher thermal stresses occur in the regions of high temperatures and high thermal gradients. The peak stresses occur at the inner walls of the mold, about 235 *MPa* at 20 seconds after pouring and approximately 320 *MPa* at 50 seconds after pouring. Gray cast iron has a yield strength of approximately 400 *MPa*, hence the mold stresses are within the elastic range. The exception to this may occur at the corners of the mold cavity where stress concentrations will be present. These stress concentrations are not obvious in Figure 2.9 due to the FEM mesh size used.

Figure 2.9 (b) shows the thermal stress contours obtained if the temperature field is computed using the assumption of instantaneous filling of the mold. It can be seen that as expected the stress contours are symmetrical about the horizontal axis. In the present study the stress distributions for finite and zero mold filling times are very close.

Although the stresses are below the yield stress, cyclic variation of these still cause deterioration of the mold. In order to minimize the cyclic fatigue of the mold, the effect of the initial mold temperature on the peak thermal stress was investigated. It was determined that lowering the initial mold temperature from 250 ^{o}C to 100 ^{o}C caused the peak thermal stresses to drop from 240 *MPa* to 165 *MPa* at 20 seconds after pouring, and from 320 *MPa* to 230 *MPa* at 50 seconds after pouring for finite pouring time calculations. There is a practical limit to lowering the mold temperature however, as the liquid metal fluidity is lowered in cooler molds, resulting in premature solidification and incomplete filling. Practical values of lower initial mold temperatures are now widely used in the industry to prolong mold life. Comparing Figure 2.9 (a) with Figure 2.9 (c) shows that as the mold heats up, the stress contours propagate towards the outer surfaces. This is

expected, as according to Figure 2.6 the temperatures in the interior of the mold rise with time, resulting in higher thermal stresses.

2.5 Conclusions

A model of the heat transfer during casting solidification is developed based on a finite difference technique. Phase change and the variation of properties with temperature are allowed for. Calculated temperatures in the casting and mold are compared against experiments with permanent mold cast iron, and satisfactory agreement is obtained. The importance of keying effects at a side gate or a projecting section (holding the casting against a mold cavity surface and affecting the interface heat transfer) are demonstrated. Thermal stresses in the mold are computed using the finite element method. The importance of using the computed temperature field in the determination of thermal stresses and their implications on mold life is shown.

An analysis of the results indicates that the discrepancies between the computed and experimentally measured temperatures are due to a combination of simplifying assumptions about the interface treatment and liquid metal convection. Mathematical modelling of the liquid metal convection may reduce some uncertainty from the computed results and this task is undertaken in the subsequent chapters. In the next chapter the Finite Volume Method, which is used in this work to compute the liquid metal convection, is described.

Chapter 3

Computation of convection

3.1 Overview

The Control Volume Method is used in this thesis for the modelling of liquid metal convection during pouring and solidification. This chapter presents an overview of the method and introduces the formulation (for example grid arrangement, governing equations and solution algorithm) used in the present study. Details of the computational domains and boundary conditions are discussed where applicable in subsequent chapters. Further details about the method may be found in [36,50,69,83].

The problem of determining motion in a *Newtonian Fluid consists of solving a set of conservation equations for the mass and momentum in the computational domain. The equations are written in tensorial notation for an incompressible fluid as [106,131]

$$\nabla \mathbf{v} = 0 \tag{3.1}$$

$$\rho \frac{D\mathbf{v}}{Dt} = \rho \mathbf{g} - \nabla p + \frac{\partial}{\partial x_j}\Big[\mu\Big(\frac{\partial v_i}{\partial x_j} + \frac{\partial v_j}{\partial x_i}\Big)\Big] \tag{3.2}$$

3.2 Background

In order to select a solution technique, a study was done to determine the suitability of the stream function–vorticity formulation [5,83], the Eulerian Lagrangian approach [14,37,88] and the Control Volume Method [36,50,69,83] to solve the problem under consideration.

In the stream function–vorticity approach the pressure is eliminated and the dependant variables are the stream function and the vorticity. A disadvantage of this formulation is that the boundary conditions are difficult to specify. The pressure, which is required for the free surface treatment (discussed in the next chapter) is not explicitly available. Extension to three dimensions is also not straightforward.

An Eulerian Lagrangian approach developed at Los Alamos (KIVA, CONCHAS and follow-up codes [14,37,88]) is an extension of the MAC method described previously. In this technique the computation is done in an Eulerian frame for the first part of each time step and the mesh is 're-zoned' during the second, Lagrangian phase. The method is explicit and the time steps are limited by the Courant criterion [43]. The codes embodying this technique are at a relatively early stage of development and are quite complex.

The Control Volume Method (TEACH and follow-up codes) is implicit in time and therefore a time step limitation is not required. The formulation is in terms of the primitive variables (velocities and pressure), therefore, application of the boundary conditions is straightforward. The structure of the code is such that modifications and extensions are relatively straightforward. The convection modelling in this study is therefore carried out by the Control Volume Method.

3.3 Turbulence modelling

The unsteady Navier–Stokes equations are valid for both laminar as well as turbulent flows, however, the spatial and time scales for turbulent flows are so small that the solution is beyond the capabilities of the present generation of computers. The usual approach is to time–average the equations which introduces the turbulent or Reynolds' Stresses. Turbulence models provide the equations and necessary assumptions to 'close' the system so that the solution of the equation set can be obtained.

3.3.1 The $K-\epsilon$ turbulence model

The $K-\epsilon$ model developed by Launder and Spalding [63] has been used in this work and requires the solution of conservation equations for the turbulent kinetic energy, K, and energy dissipation, ϵ, given as [63]

$$\frac{\partial \rho K}{\partial t}+\frac{\partial}{\partial x_j}(\rho u_j K)=-\overline{\rho u_i' u_j'}\frac{\partial u_i}{\partial x_j}+\frac{\partial}{\partial x_j}(\frac{\mu_t}{\sigma_K}\frac{\partial K}{\partial x_j})-\rho\epsilon C_D \tag{3.3}$$

and

$$\frac{\partial \rho \epsilon}{\partial t}+\frac{\partial}{\partial x_j}(\rho u_j \epsilon)=-C_1\frac{\epsilon}{K}\overline{\rho u_i' u_j'}\frac{\partial u_i}{\partial x_j}+\frac{\partial}{\partial x_j}(\frac{\mu_t}{\sigma_\epsilon}\frac{\partial \epsilon}{\partial x_j})-C_2\rho\frac{\epsilon^2}{K} \tag{3.4}$$

where the constants C_1, C_2, C_D, σ_K and σ_ϵ are given in Table 3.1 [50,55]. The model relates the Reynolds' Stresses to a turbulent 'eddy' viscosity, μ_t, [5,40,50]

$$-\overline{\rho u_i' u_j'}=\mu_t\left(\frac{\partial u_i}{\partial x_j}+\frac{\partial u_j}{\partial x_i}\right)-\frac{2}{3}\rho K\delta_{i,j} \tag{3.5}$$

where

$$K=\frac{1}{2}\overline{u_i' u_i'} \tag{3.6}$$

The turbulent viscosity is expressed as a function of the fluid density and the local turbulence characteristics [50,55] as

$$\mu_t=C_\mu\rho\sqrt{K}l \tag{3.7}$$

Table 3.1 Constants in the $K-\epsilon$ model

C_1	C_2	C_μ	C_D	$\sigma_{K,t}$	$\sigma_{\epsilon,t}$	$\sigma_{h,t}$
1.44	1.92	0.09	1.0	1.0	1.3	0.9

where C_μ is an empirical constant, $\sqrt{K}$ characterizes the fluctuation velocity and l is the characteristic length scale of the turbulence eddies [58,89]. ϵ is related K by dimensional analysis as [55,94]

$$\epsilon = \frac{K^{3/2}}{l} \tag{3.8}$$

The turbulent viscosity is therefore expressed as

$$\mu_t = C_\mu \rho K^2/\epsilon \tag{3.9}$$

The turbulent diffusive coefficients are related to the turbulent viscosity by [55]

$$\Gamma_{\phi,t} = \frac{\mu_t}{\sigma_{\phi,t}} \tag{3.10}$$

where $\sigma_{\phi,t}$ is the Prandtl/Schmidt number [50]. The effective viscosity and other diffusive coefficients are obtained by combining the laminar and eddy viscosity values

$$\mu_{eff} = \mu_{lam} + \mu_t \tag{3.11}$$

$$\Gamma_{\phi,eff} = \frac{\mu_{lam}}{\sigma_{\phi,t}} + \frac{\mu_t}{\sigma_{\phi,t}} \tag{3.12}$$

3.4 General transport equations

The test problems solved in the subsequent chapters are in the axi-symmetric cylindrical co-ordinate system. The governing equations for this system are [36,50]

continuity equation

$$\frac{\partial}{\partial x}(r\rho u) + \frac{\partial}{\partial r}(r\rho v) = 0 \tag{3.13}$$

x-momentum equation

$$\frac{\partial \rho u}{\partial t} + \frac{1}{r}\left[\frac{\partial}{\partial x}(r\rho uu) + \frac{\partial}{\partial r}(r\rho vu)\right] = - \frac{\partial p}{\partial x} + \rho g_x + \frac{1}{r}\left[\frac{\partial}{\partial x}\left(r\mu_{eff}\frac{\partial u}{\partial x}\right) + \frac{\partial}{\partial r}\left(r\mu_{eff}\frac{\partial u}{\partial r}\right)\right] + S_u \tag{3.14}$$

r-momentum equation

$$\frac{\partial \rho v}{\partial t} + \frac{1}{r}\left[\frac{\partial}{\partial x}(r\rho uv) + \frac{\partial}{\partial r}(r\rho vv)\right] = -\frac{\partial p}{\partial r} + \rho g_r + \frac{1}{r}\left[\frac{\partial}{\partial x}\left(r\mu_{eff}\frac{\partial v}{\partial x}\right) + \frac{\partial}{\partial r}\left(r\mu_{eff}\frac{\partial v}{\partial r}\right)\right] - \mu_{eff}\frac{v}{r^2} + S_v \tag{3.15}$$

where the effective viscosity has been defined previously and additional viscous terms associated with non-uniform viscosity are given as [50]

$$S_u = \frac{\partial}{\partial x}\left(\mu_{eff}\frac{\partial u}{\partial x}\right) + \frac{1}{r}\frac{\partial}{\partial r}\left(r\mu_{eff}\frac{\partial v}{\partial x}\right) \tag{3.16}$$

$$S_v = \frac{\partial}{\partial x}\left(\mu_{eff}\frac{\partial u}{\partial r}\right) + \frac{1}{r}\frac{\partial}{\partial r}\left(r\mu_{eff}\frac{\partial v}{\partial r}\right) - \mu_{eff}\frac{v}{r^2} \tag{3.17}$$

energy equation

$$\frac{\partial \rho h}{\partial t} + \frac{1}{r}\left[\frac{\partial}{\partial x}(r\rho uh) + \frac{\partial}{\partial r}(r\rho vh)\right] = \frac{1}{r}\left[\frac{\partial}{\partial x}\left(r\Gamma_{eff}\frac{\partial h}{\partial x}\right) + \frac{\partial}{\partial r}\left(r\Gamma_{eff}\frac{\partial h}{\partial r}\right)\right] + Q \tag{3.18}$$

where the generation due to viscous dissipation is neglected.

K transport equation

$$\frac{\partial \rho K}{\partial t} + \frac{1}{r}\left[\frac{\partial}{\partial x}(r\rho uK) + \frac{\partial}{\partial r}(r\rho vK)\right] = \frac{1}{r}\left[\frac{\partial}{\partial x}\left(r\frac{\mu_{eff}}{\sigma_K}\frac{\partial K}{\partial x}\right) + \frac{\partial}{\partial r}\left(r\frac{\mu_{eff}}{\sigma_K}\frac{\partial K}{\partial r}\right)\right] + G - C_D\rho\epsilon \tag{3.19}$$

Table 3.2 Diffusive coefficients and source terms

QUANTITY	ϕ	Γ_ϕ	S_ϕ
Continuity	1	0	0
Radial Momentum	v	μ_{eff}	$-(\partial p/\partial r) - (\mu_{eff} v/r^2) + S_v$
Axial Momentum	u	μ_{eff}	$-(\partial p/\partial x) + S_u$
Energy	h	$\Gamma_{h,eff}$	Q
Turbulence Energy	K	μ_{eff}/σ_K	$G - C_D \rho \epsilon$
Energy Dissipation	ϵ	$\mu_{eff}/\sigma_\epsilon$	$C_1 G\epsilon/K - C_2 \rho \epsilon^2/K$

ϵ transport equation

$$\frac{\partial \rho \epsilon}{\partial t} + \frac{1}{r}\left[\frac{\partial}{\partial x}(r\rho u\epsilon) + \frac{\partial}{\partial r}(r\rho v\epsilon)\right] = \frac{1}{r}\left[\frac{\partial}{\partial x}\left(r\frac{\mu_{eff}}{\sigma_\epsilon}\frac{\partial \epsilon}{\partial x}\right) + \frac{\partial}{\partial r}\left(r\frac{\mu_{eff}}{\sigma_\epsilon}\frac{\partial \epsilon}{\partial r}\right)\right] + C_1\frac{\epsilon}{K}G - C_2\rho\frac{\epsilon^2}{K} \quad (3.20)$$

where G represents the generation of the turbulent kinetic energy [55]

$$G = \mu_t\left[2\left\{\left(\frac{\partial u}{\partial x}\right)^2 + \left(\frac{\partial v}{\partial r}\right)^2 + \left(\frac{v}{r}\right)^2\right\} + \left\{\left(\frac{\partial u}{\partial r}\right) + \left(\frac{\partial v}{\partial x}\right)\right\}^2 - \frac{2}{3}\left\{\frac{\partial u}{\partial x} + \frac{1}{r}\frac{\partial}{\partial r}(rv)\right\}\right] \quad (3.21)$$

Equations (3.13) to (3.20) can be expressed in a general transport equation of the form [36,50,69,83]

$$\frac{\partial \rho\phi}{\partial t} + \frac{1}{r}\left[\frac{\partial}{\partial x}(\rho u r\phi) + \frac{\partial}{\partial r}(\rho v r\phi) - \frac{\partial}{\partial x}\left(r\Gamma_\phi\frac{\partial \phi}{\partial x}\right) - \frac{\partial}{\partial r}\left(r\Gamma_\phi\frac{\partial \phi}{\partial r}\right)\right] = S_\phi \quad (3.22)$$

where the diffusive and source terms for different ϕ are given in Table 3.2.

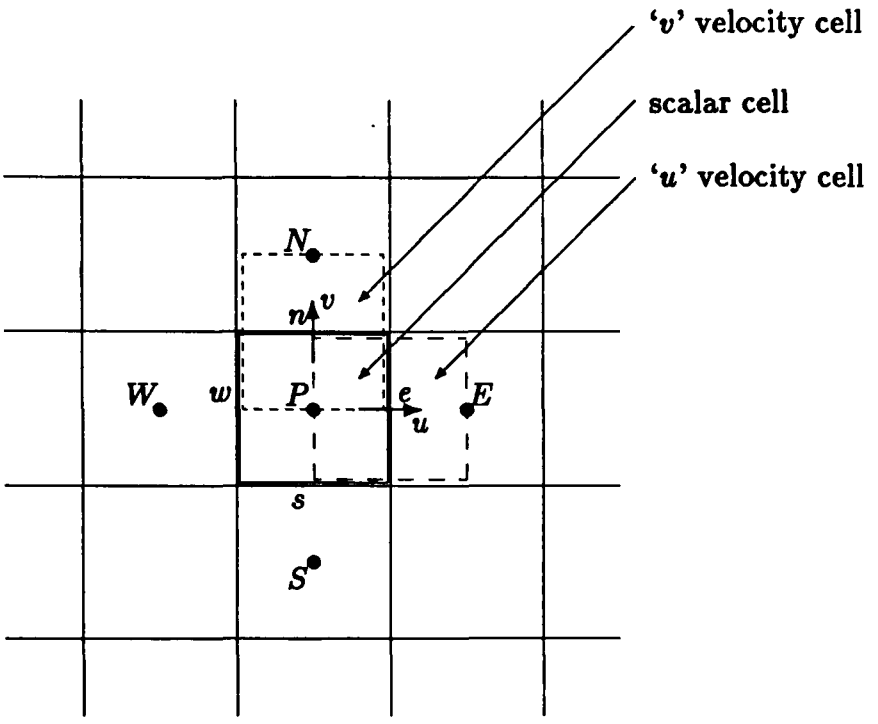

Figure 3.1 Grid arrangement for the Finite Volume Method

3.5 Grid layout

The layout of the computational grid is shown in Figure 3.1. The domain is divided into a rectangular grid of computational cells (called control volumes). The scalar quantities (p, h, K, ϵ) are defined at the *nodes* which are located at the scalar cell geometric centers ($\bullet$). The point 'P' is a node and its north, south, east and west neighbors are 'N', 'S', 'E' and 'W' respectively. The control volume faces are identified by lower case letters ('n','s','e','w'). The velocities are defined at the scalar cell walls at the locations ($\rightarrow$, $\uparrow$) so that they are between the pressures which 'drive the flow', and are explicitly available for the determination of the convective flux at the control volume faces. A similar arrangement is also used in the MAC method, and is required to prevent a physically unrealistic 'wavy' velocity field [83]. The cells corresponding to the velocities are drawn with dashed lines in Figure 3.1. It can be seen that the 'u' velocity grid is *staggered* half a cell width to the east and

the 'v' velocity grid is staggered half a cell height to the north.

The first step in the derivation of the finite volume equations is the integration of *eq*(3.22) over the appropriate control volume (centered around the ϕ):

$$\int\int \left\{ \frac{\partial \rho\phi}{\partial t} + \frac{1}{r}\left[\frac{\partial}{\partial x}(\rho u r\phi) + \frac{\partial}{\partial r}(\rho v r\phi) - \frac{\partial}{\partial x}\left(r\Gamma_\phi \frac{\partial \phi}{\partial x} \right) - \frac{\partial}{\partial r}\left(r\Gamma_\phi \frac{\partial \phi}{\partial r} \right) \right] - S_\phi \right\} r\, dr\, dx = 0 \qquad (3.23)$$

The resulting equation is:

$$\frac{(\rho\phi_P - \rho_o\phi_{P,o})V}{\Delta t} + \left[\rho u\phi - \Gamma_\phi \frac{\partial \phi}{\partial x} \right]_e A_e - \left[\rho u\phi - \Gamma_\phi \frac{\partial \phi}{\partial x} \right]_w A_w + \left[\rho v\phi - \Gamma_\phi \frac{\partial \phi}{\partial r} \right]_n A_n - \left[\rho v\phi - \Gamma_\phi \frac{\partial \phi}{\partial r} \right]_s A_s = [Sp\phi_p + Su]\, V \qquad (3.24)$$

where the lower case subscripts refer to the control volume faces (Figure 3.1). Sp and Su are linearized source terms so that [83]

$$\int\int S_\phi\, r\, dr\, dx = Sp\phi_P + Su \qquad (3.25)$$

A stabilization technique is used in which a false source is added on to each algebraic equation. The magnitude of this false source is:

$$S_{false} = |m_{net}|(\phi_P{}^o - \phi_P) \qquad (3.26)$$

where m_{net} is the net flow out of the cell and the superscript 'o' stands for the previous iteration value. This false source provides additional under-relaxation during the initial cycles and helps stabilize the solution. At convergence ϕ_p and $\phi_p{}^o$ are equal so the false source disappears.

The next step is to evaluate the convective diffusive terms, $[\rho u\phi - \Gamma_\phi \partial\phi/\partial x]$ in *eq*(3.24), at the faces of the cells. The hybrid differencing scheme is used to express these in terms of the nodal ϕ values. This scheme uses central differencing

if the convection through the cell is low ($|Pe| \leq 2$), and upwind differencing if the convection through the cell is high ($|Pe| > 2$). The cell Peclet number, Pe, is defined as

$$Pe = \frac{(\rho u)\Delta x}{\Gamma_\phi} \tag{3.27}$$

The convective diffusive term for the east face of the cell,

$$C_e = \left[\rho u\phi - \Gamma_\phi \frac{\partial \phi}{\partial x}\right]_e \tag{3.28}$$

for example, can be represented by the hybrid difference scheme as

$$C_e = \begin{cases} (\rho u)_e A_e(\phi_P + \phi_E)/2 - \Gamma_\phi A_e(\phi_E - \phi_P)/\Delta x_e & \text{for } |Pe| \leq 2 \\ (\rho u)_e A_e \phi_P & \text{for } Pe > 2 \\ (\rho u)_e A_e \phi_E & \text{for } Pe < -2 \end{cases} \tag{3.29}$$

where the Peclet number is evaluated on the east face of the cell. In a similar manner all the cell facial flux in *eq*(3.24) are expressed in terms of the nodal value ϕ_P and the neighbor values ϕ_N, ϕ_S, ϕ_E and ϕ_W.

After expressing the cell facial flux in *eq*(3.24) in terms of the nodal ϕ values and collecting the coefficients of ϕ_P, ϕ_N, ϕ_S, ϕ_E and ϕ_W the following algebraic equation is obtained

$$a_P\phi_P = a_N\phi_N + a_S\phi_S + a_E\phi_E + a_W\phi_W + Sp\,\phi_P + Su \tag{3.30}$$

where the transient terms have been absorbed in Su and Sp. In the above equation a_P, a_N, a_S, a_E and a_W are the collected coefficients of ϕ_P, ϕ_N, ϕ_S, ϕ_E and ϕ_W. These coefficients represent the influence of the values of the neighboring ϕ s and the source terms on the value of the nodal ϕ value, ϕ_P. The effects of the hybrid differencing scheme are reflected through the values of these coefficients, as they depend on the cell Peclet number. The coefficient coupling ϕ_P with ϕ_E, for example, is written as

$$a_E = \begin{cases} \Gamma_e A_e/\delta x_e - (1/2)\rho u_e A_e & \text{for } |Pe| \leq 2 \\ 0 & \text{for } Pe > 2 \\ -\rho_e u_e A_e & \text{for } Pe < -2 \end{cases} \tag{3.31}$$

The other coefficients can be expressed in a similar manner. The details of the derivation of the coefficients and the hybrid differencing scheme can be found in the text by Patankar [83].

Eq(3.30) is an algebraic equation which links the nodal ϕ value with the values of the neighboring ϕ's. Such equations are established for all the nodal points in the domain. The solution procedure adopted is the 'Line by Line' method which employs the Tri-Diagonal Matrix Algorithm. In this technique the equation set for each row or each column (a line) of grid nodes is set up, assuming the ϕ's in the neighboring lines to be known. This results in a tri-diagonal equation set for each line, which can be solved very efficiently. The solution then proceeds on to the next line and in this manner the entire computational domain is swept in a line by line fashion.

3.6 Solution algorithm

The algebraic equations described in the previous section are established for each of the dependant variables. The solution procedure used is the SIMPLE[1] algorithm. The procedure can be summarized as follows [83]:

1. The momentum equations are solved based on an assumed pressure field.
2. Pressure and velocity corrections are carried out, based on the solution of a pressure correction equation and velocity correction formulae.
3. Conservation equations for the other variables (which are mutually coupled to the velocities) are solved.
4. The corrected pressure field is treated as a newly guessed pressure field and the whole process is repeated until convergence is reached.

[1]Semi-Implicit Method for Pressure Linked Equations

3.7 Convergence criteria

As the solution is obtained by an iterative technique, certain criteria have to be established to determine if the solution has 'converged'.

The criterion is based on the measure of how well the solution satisfies the finite difference equations. The absolute residual error for each variable is obtained as

$$\Theta_\phi = (a_P - Sp)\phi_P - \sum a_i\phi_i - Su$$

and $\sum|\Theta_\phi|$ is obtained for the entire domain at the end of each iteration. The iterations are repeated until $\sum|\Theta_\phi|$ is less than 0.1% of a representative value in the field. This ensures that the finite difference equations are satisfied to a 'reasonable' accuracy.

In another check that is simultaneously made, the field values of the dependant variables are monitored at representative locations during the iterative process. The solution is not accepted as 'converged' if there is significant variation in the values of any variable from one iteration to the next. It should be mentioned that the criterion described in the previous paragraph still *has* to be satisfied, however the second criterion serves as an additional precaution to ensure convergence.

Chapter 4

FILLING OF THE MOLD

4.1 Introduction

Convection during filling of molds has received little attention because of the complexities in the mathematical treatment of free surfaces and domains which change spatially with time. In the metallurgical industry, in addition to the filling of molds, free surface flows also occur in ladles and tundishes [60,61,102,104,119]. Modelling such flows poses considerable problems as the free surface profile has to be continuously tracked and the correct boundary conditions have to be applied at it. Many studies [60,61,102,104,119] assume a pseudo–frictionless flat surface instead of modelling the surface shape. This assumption does not correctly reflect the pressure and velocity distributions in the region of the free surface and the resulting errors have often been attributed to the turbulence modelling.

A new technique is proposed to model flows with free surfaces using the Control Volume Method. Computational work and flow visualization experiments have been carried out to determine the free surface shapes and velocity distributions during the filling of a cylindrical container with water. The inlet to the cylinder is located

centrally at the bottom. The filling process generates an axi-symmetric flow pattern and a free surface profile. The following contributions are reported in this chapter:

1. a technique to model domains which change spatially in time
2. a technique to mathematically treat free surfaces
3. a report of experimental data on the velocity distributions and free surface shapes during the filling of a cylindrical container with water.

The models have been developed and tested for an axi–symmetric two–dimensional domain and can be extended to three dimensions. As discussed in a subsequent section, the free surface treatment techniques developed in this study have already proven to be useful in other areas.

4.2 Experimental work

4.2.1 The water flow system

The test section consists of a plexiglass cylinder connected by a plastic hose with a quick closing valve to a reservoir. A schematic of the apparatus with dimensions is illustrated in Figure 4.1.

4.2.2 The flow visualization particles

Flow visualization is carried out by taking timed exposures of neutrally buoyant particles suspended in the fluid. The concentration of the particles is adjusted to maximize the 'observable' streaks on the photographs. A mild soap mixture is

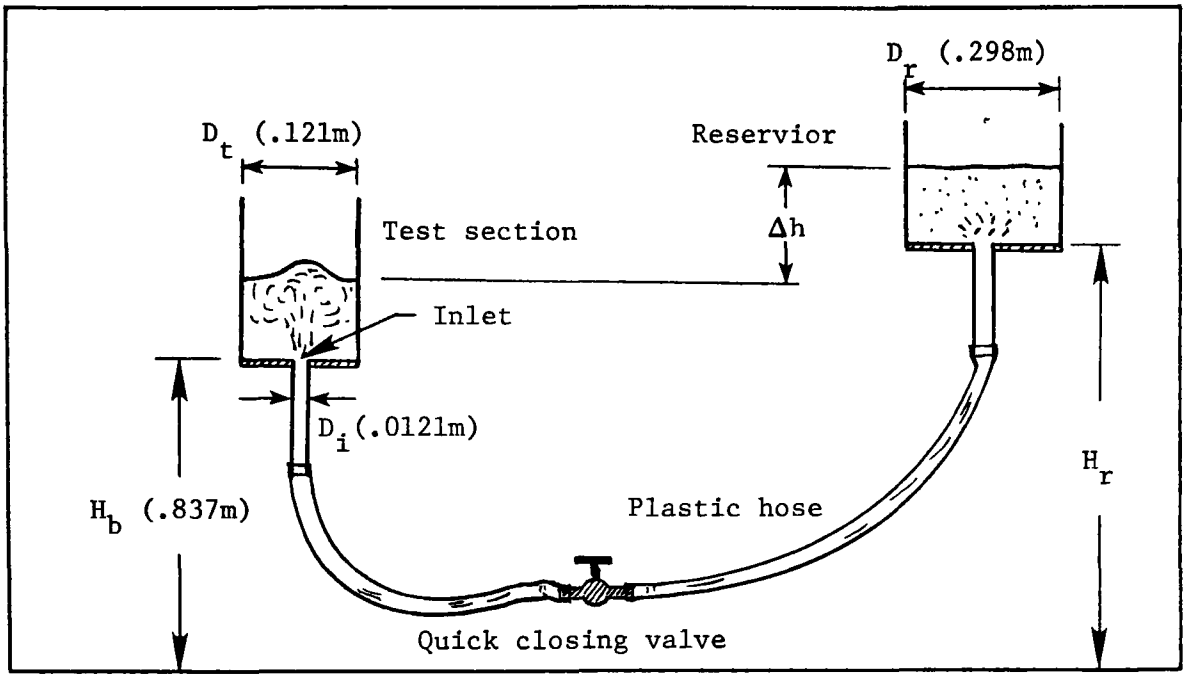

Figure 4.1 Schematic of the water flow system

used to reduce surface tension effects. An average particle size of 1.0 *mm* is used as smaller particles are difficult to detect in the photographs. The smallest flow structure that can be resolved by this technique is about an order of magnitude larger than the particle size [75]. The one–dimensional equation of motion of a neutrally buoyant particle is [93]

$$m_P \frac{du_P}{dt} = C_D A_P \frac{\rho_F}{2}(u_F - u_P)^2 \tag{4.1}$$

where u_P is the particle velocity and u_F is the fluid velocity. *Eq*(4.1) can be simplified using the Stokes Law and rearranged as

$$\frac{du_P}{dt} = \frac{18\mu}{\rho_P d_P^2}(u_F - u_P) \tag{4.2}$$

which has the following solution for constant u_F

$$u_P = u_F[1 - e^{-K(t-t_o)}] + u_{P_o} e^{-K(t-t_o)} \tag{4.3}$$

where $K = 18\mu/\rho_P d_p^2$. Substitution of the test parameters shows that starting from rest, the particles require approximately a quarter of a second to attain 99% of the fluid velocity. In reality the particles move continuously with the fluid and C_D is much higher [93] than predicted by Stokes Law. Also, the lift forces because of velocity gradients are small compared to the drag force for most flows [75]. The particles are therefore assumed to follow the fluid reasonably well in this study.

4.2.3 The photographic recording system

The lighting system (see Figure 4.2) consists of a slide projector mounted vertically on top of and pointing downwards at the test section. An opaque slide with a 2 *mm* by 20 *mm* slit is used to produce a vertical light plane passing through the center of the test section. The illuminated particles remain within 10% of the focal length resulting in a satisfactory focus throughout the test section. The photographs are taken with a Yashika FE 35 *mm* camera equipped with a 50 *mm* lens. Black and White Ilford 125*ASA* film is used.

4.2.4 The test procedure

The projector is adjusted so that the light plane is centered, perpendicular to the test section, and 1 *cm* thick at the focusing plane. The exposure settings on the camera are adjusted according to Table 4.1. Half a stop of overexposure is used to obtain brighter images. A photograph of a reference grid inserted in the test section (full of water) is initially taken so that subsequent photographs can be enlarged to actual size. The test section is drained and the initial water level in the reservoir noted. Water is allowed to flow into the test section, carrying the particles with it. Photographs are taken at appropriate times and the procedure is repeated as necessary.

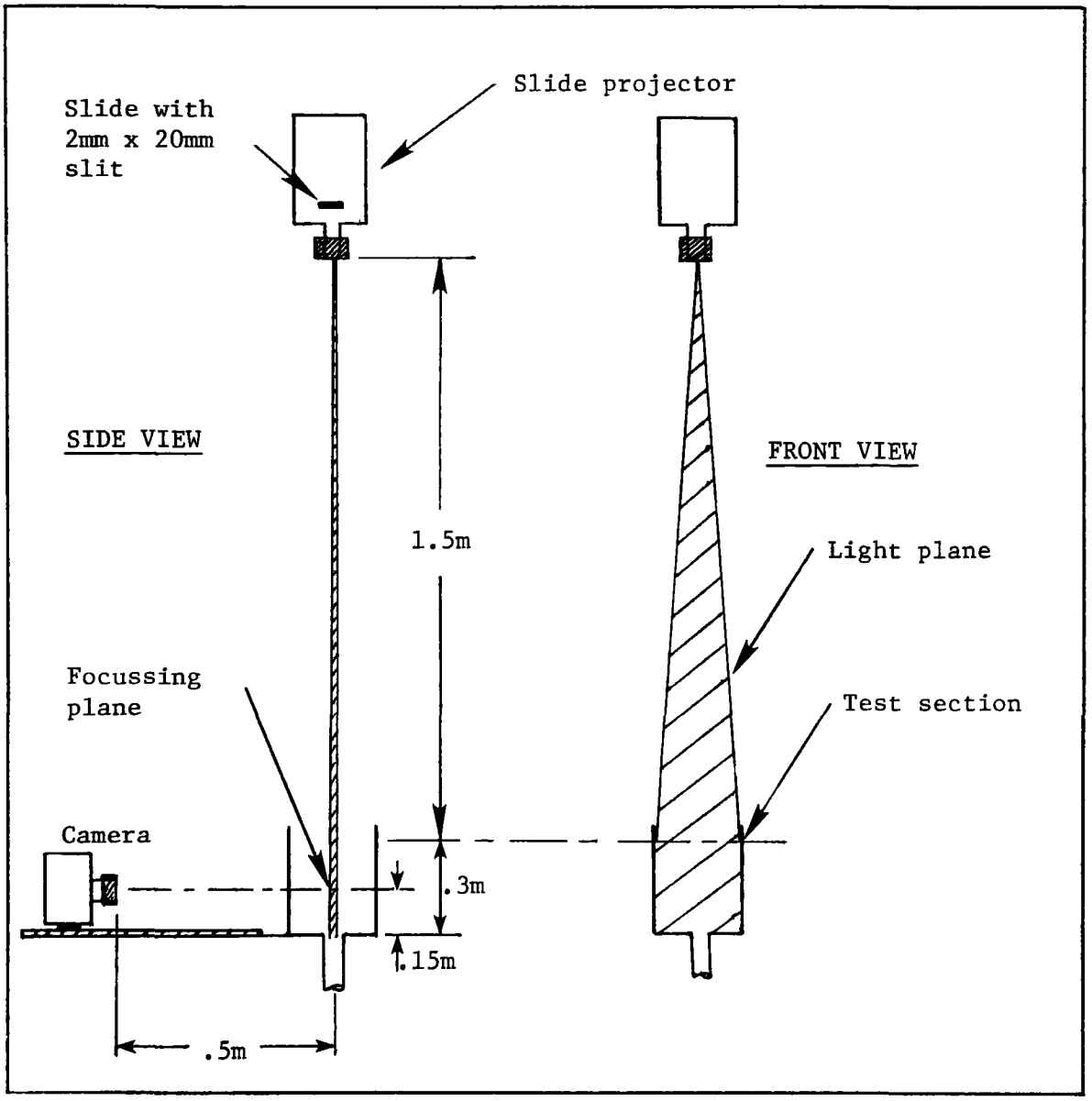

Figure 4.2 Photographic recording system

Table 4.1 Exposure Settings

Range of Particle Velocity	Exposure Time (s)	Aperture
Highest	1/30	f 1.9
High	1/15	2.8
Medium	1/8	4
Slow	1/4	5.6
Slowest	1/2	8

4.2.5 Determination of the inlet velocity

The velocity at the inlet is expressed as a function of the head Δh by

$$U_{in} = \sqrt{\Delta h / C} \tag{4.4}$$

Figure 4.3 shows the correlation between U_{in}^2 and Δh. The constant C is determined from the slope to be 2.235.

4.2.6 Interpretation of the streaklines

The photographs contain a large number of streaklines, however only a small fraction of these can be used to determine the particle velocities. Particles which enter or leave the light plane during the exposure period leave tapered streaklines as shown in Figure 4.4. Also, if the particle has a significant circumferential motion, the streaklines tend to be brighter and thicker. Such streaklines cannot be used to interpret the velocity.

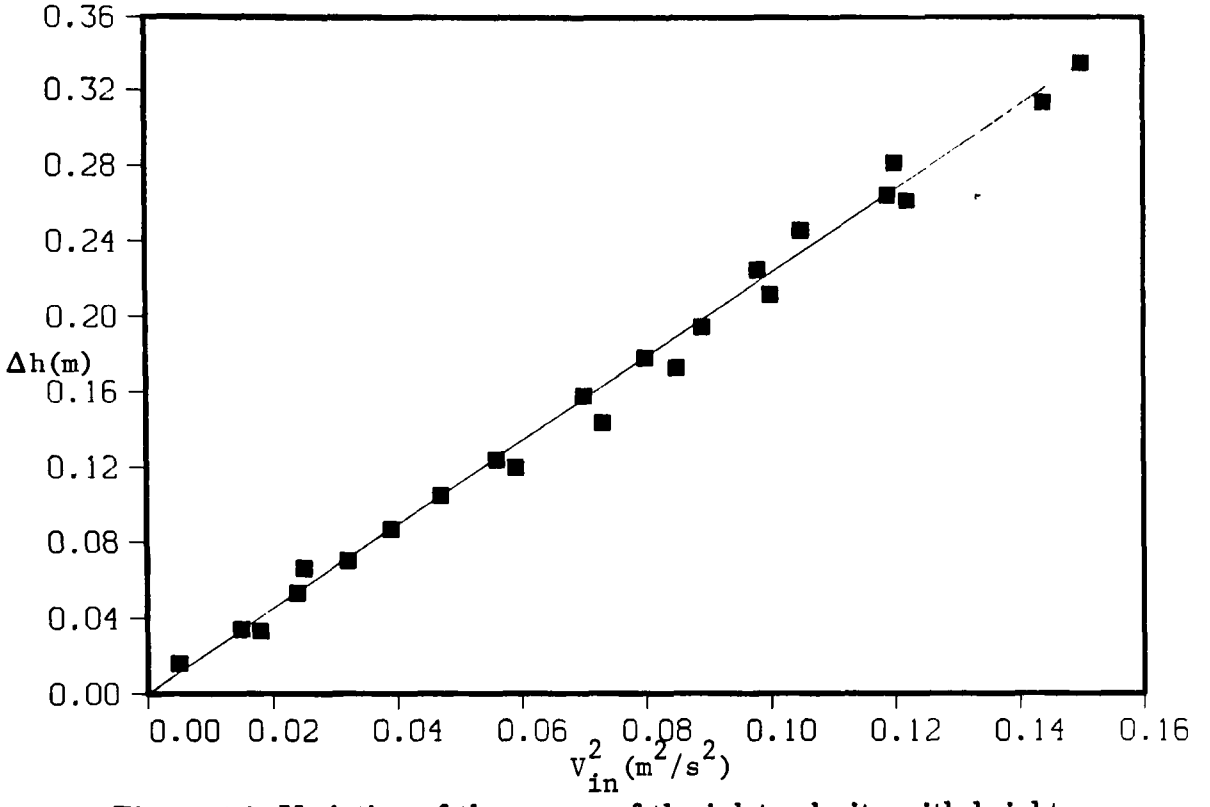

Figure 4.3 Variation of the square of the inlet velocity with height

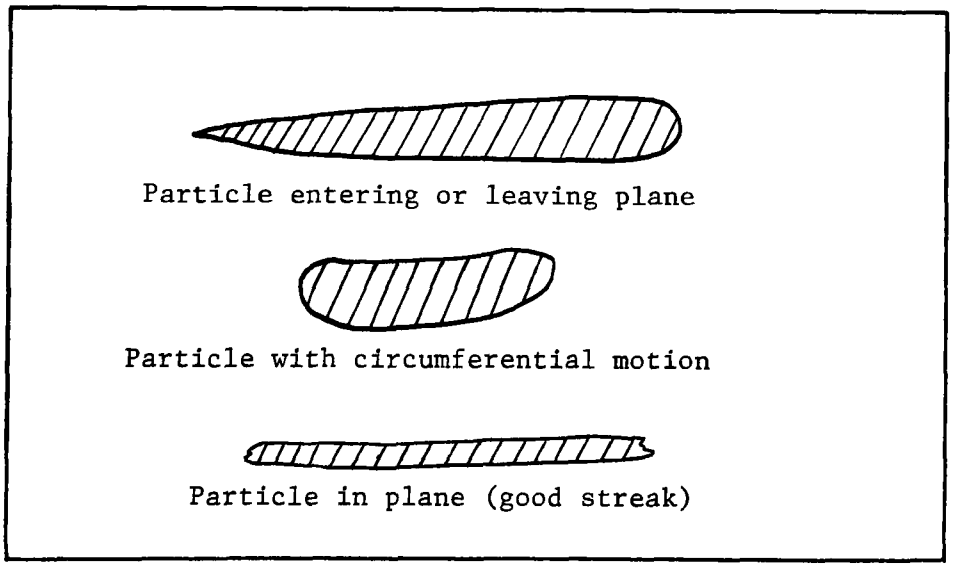

Figure 4.4 Interpretation of the streaklines

4.3 Mathematical modelling

The conservation equations of mass, momentum, energy and turbulence parameters have been presented and the Finite Volume Method has been described in the previous chapter. This section addresses the simulation of the rising level of the fluid and the free surface treatment.

4.3.1 Modelling the filling process

The flow enters centrally from the bottom of the test section in the form of a turbulent jet, as the Reynolds number based on the orifice diameter and average fluid velocity is 2500 [9,82,106,131]. The effects of turbulence are simulated by the $K - \epsilon$ model which is described in the previous chapter.

The level of the fluid rises continuously during filling. A coordinate transformation is employed to continuously conform the mesh to the region of the domain which contains the fluid. This hybrid Eulerian–Lagrangian technique enables the mesh to 'expand' axially as the level of the fluid rises. The method is similar to the approach of Watkins [129] who employed a co-ordinate transformation to compute flows in an engine cylinder. Watkins technique is not applicable to the problem under consideration because of the need to model the free surface. In this study a more 'flexible' transformation is developed which allows only that part of the domain to expand which contains the fluid. The additional flexibility is required because the region of the domain reserved for the treatment of the free surface does not expand during filling.

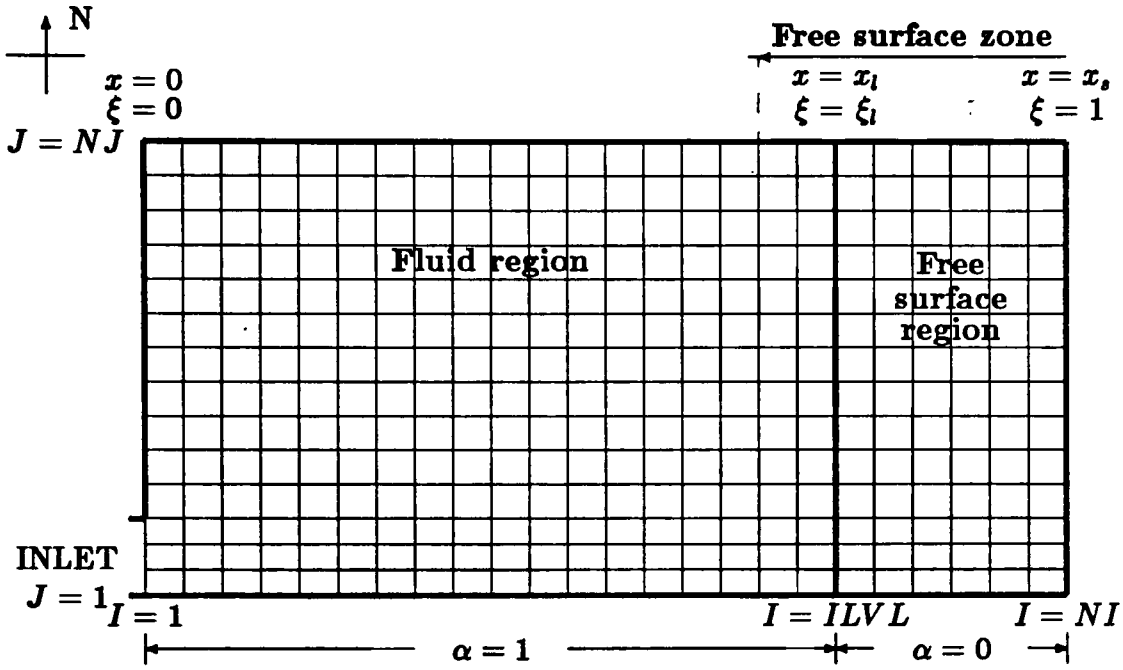

Figure 4.5 Computational domain and mesh

Co-ordinate transformation

The transformation developed in this study maps the domain from the (x, r, t) plane to the (ξ, r, t) plane so that the variable ξ specifying the axial location assumes constant values at the bottom of the cylinder, at the 'mean' fluid level and at the top.

Figure 4.5 shows the computational domain divided into a region which 'expands' ($\alpha = 1$) and a region which does not expand ($\alpha = 0$). The following relations hold between x and ξ

$$\begin{aligned} \xi &= 0 \quad \text{for} \quad x = 0 \\ \xi &= \xi_l \quad \text{for} \quad x = x_l \\ \xi &= 1 \quad \text{for} \quad x = x_s \end{aligned} \tag{4.5}$$

In the region of the domain containing fluid, ($\alpha = 1$)

$$\xi = \frac{\xi_l}{x_l} x \tag{4.6}$$

and in the free surface region, ($\alpha = 0$)

$$\xi = \frac{(\xi_l - 1)}{(x_l - x_s)} x - \frac{x_l(\xi_l - 1)}{(x_l - x_s)} + \xi_l \tag{4.7}$$

Combining *eq*(4.6) with *eq*(4.7) gives

$$\xi = \chi_1 x + \chi_2 \tag{4.8}$$

where

$$\chi_1 = \frac{\alpha \xi_l}{x_l} - \frac{\alpha \xi_l - \xi_l - \alpha + 1}{(x_l - x_s)} \tag{4.9}$$

and

$$\chi_2 = \xi_l - \alpha \xi_l + \frac{\alpha x_l \xi_l - \alpha x_l - x_l \xi_l + x_l}{(x_l - x_s)} \tag{4.10}$$

Differentiating *eq*(4.8) with respect to x

$$\frac{\partial \xi}{\partial x} = x \frac{\partial \chi_1}{\partial x} + \chi_1 + \frac{\partial \chi_2}{\partial x} \tag{4.11}$$

but

$$\frac{\partial \chi_1}{\partial x} = 0 \tag{4.12}$$

and

$$\frac{\partial \chi_2}{\partial x} = 0 \tag{4.13}$$

therefore

$$\frac{\partial \xi}{\partial x} = \chi_1 \tag{4.14}$$

Differentiating *eq*(4.8) with respect to t

$$\frac{\partial \xi}{\partial t} = x \frac{\partial \chi_1}{\partial t} + \frac{\partial \chi_2}{\partial t} \tag{4.15}$$

where

$$\frac{\partial \chi_1}{\partial t} = \frac{(\dot{x}_l - \dot{x}_s)(\alpha\xi_l - \xi_l - \alpha + 1)}{(x_l - x_s)^2} - \frac{\alpha\xi_l\dot{x}_l}{x_l^2} \tag{4.16}$$

and

$$\frac{\partial \chi_2}{\partial t} = \frac{(\dot{x}_l\alpha\xi_l - \alpha\dot{x}_l - \xi_l\dot{x}_l + \dot{x}_l)(x_l - x_s) - (\dot{x}_l - \dot{x}_s)(\alpha\xi_l x_l - \alpha x_l - \xi_l x_l + x_l)}{(x_l - x_s)^2} \tag{4.17}$$

Rearranging *eq*(4.8)

$$x = \frac{\xi - \chi_2}{\chi_1} \tag{4.18}$$

Substituting the above result in *eq*(4.15)

$$\frac{\partial \xi}{\partial t} = \frac{(\xi - \chi_2)}{\chi_1}\frac{\partial \chi_1}{\partial t} + \frac{\partial \chi_2}{\partial t}$$

and rearranging the above equation and using the notation

$$\dot{\chi}_1 = \frac{\partial \chi_1}{\partial t}, \qquad \dot{\chi}_2 = \frac{\partial \chi_2}{\partial t}$$

gives

$$\frac{\partial \xi}{\partial t} = \frac{\dot{\chi}_1}{\chi_1}\xi + \frac{\chi_1\dot{\chi}_2 - \dot{\chi}_1\chi_2}{\chi_1}$$

or

$$\frac{\partial \xi}{\partial t} = \frac{\dot{\chi}_1}{\chi_1}\xi + \chi_1\frac{\partial}{\partial t}\left(\frac{\chi_2}{\chi_1}\right) \tag{4.19}$$

The dependant variables are transformed from the (x, r, t) space to the (ξ, r, t) space, therefore

$$\phi(x, r, t) = \phi'(\xi, r, t)$$

and

$$d\phi = d\phi'$$

therefore

$$\frac{\partial \phi}{\partial r}dr + \frac{\partial \phi}{\partial x}dx + \frac{\partial \phi}{\partial t}dt = \frac{\partial \phi'}{\partial r}dr + \frac{\partial \phi'}{\partial \xi}\frac{\partial \xi}{\partial x}dx + \frac{\partial \phi'}{\partial \xi}\frac{\partial \xi}{\partial t}dt + \frac{\partial \phi'}{\partial t}dt \tag{4.20}$$

Comparing coefficients of dr, dx and dt in the above equation yield

$$\frac{\partial \phi}{\partial r} = \frac{\partial \phi'}{\partial r} \tag{4.21}$$

$$\frac{\partial \phi}{\partial x} = \frac{\partial \phi'}{\partial \xi}\frac{\partial \xi}{\partial x}$$

Substituting $\partial \xi / \partial x$ from $eq(4.14)$ above gives

$$\frac{\partial \phi}{\partial x} = \chi_1 \frac{\partial \phi'}{\partial \xi} \tag{4.22}$$

$$\frac{\partial \phi}{\partial t} = \frac{\partial \phi'}{\partial \xi}\frac{\partial \xi}{\partial t} + \frac{\partial \phi'}{\partial t}$$

Substituting $\partial \xi / \partial t$ from $eq(4.19)$ above gives

$$\frac{\partial \phi}{\partial t} = \frac{\partial \phi'}{\partial t} + \frac{\partial \phi'}{\partial \xi}\left\{\frac{\dot{\chi}_1}{\chi_1}\xi + \chi_1 \frac{\partial}{\partial t}\left(\frac{\chi_2}{\chi_1}\right)\right\} \tag{4.23}$$

The grid velocity U_G is interpolated on the basis of the following conditions

$$\begin{aligned} U_G &= 0 \quad \text{for} \quad \xi = 0 \\ U_G &= \dot{x}_l \quad \text{for} \quad \xi = \xi_l \\ U_G &= \dot{x}_s \quad \text{for} \quad \xi = 1 \end{aligned} \tag{4.24}$$

which yields for $\alpha = 1$

$$U_G = \frac{\dot{x}_l}{\xi_l}\xi$$

and for $\alpha = 0$

$$U_G = \dot{x}_l + \frac{(\dot{x}_l - \dot{x}_s)}{(\xi_l - 1)}(\xi - \xi_l)$$

Combining the above two equations yields the grid velocity in the domain as

$$U_G = \chi_3 \xi + \chi_4 \tag{4.25}$$

and

$$\frac{\partial U_G}{\partial \xi} = \chi_3 \tag{4.26}$$

where

$$\chi_3 = \frac{(1-\alpha)(\dot{x}_l - \dot{x}_s)}{(\xi_l - 1)} + \alpha\frac{\dot{x}_l}{\xi_l} \tag{4.27}$$

$$\chi_4 = (1-\alpha)\dot{x}_l - \xi_l\frac{(1-\alpha)(\dot{x}_l - \dot{x}_s)}{(\xi_l - 1)} \tag{4.28}$$

The velocity relative to the grid, $\overline{u}$, is related to the velocity in the inertial frame, u, by

$$\overline{u} = u - U_G \tag{4.29}$$

Multiplying both sides by $\rho\phi'$

$$\rho\overline{u}\phi' = \rho u\phi' - \rho U_G\phi' \tag{4.30}$$

Taking partial derivatives with respect to ξ

$$\frac{\partial}{\partial\xi}(\rho\overline{u}\phi') = \frac{\partial}{\partial\xi}(\rho u\phi') - \frac{\partial}{\partial\xi}(\rho U_G\phi') \tag{4.31}$$

The last term of the above equation can be written as

$$\frac{\partial}{\partial\xi}(\rho U_G\phi') = U_G\frac{\partial}{\partial\xi}(\rho\phi') + \rho\phi'\frac{\partial}{\partial\xi}U_G$$

or using *eq*(4.26)

$$\frac{\partial}{\partial\xi}(\rho U_G\phi') = U_G\frac{\partial}{\partial\xi}(\rho\phi') + \rho\phi'\chi_3 \tag{4.32}$$

Substituting the above equation for the last term of *eq*(4.31) and rearranging gives

$$\frac{\partial}{\partial\xi}(\rho u\phi') = \frac{\partial}{\partial\xi}(\rho\overline{u}\phi') + U_G\frac{\partial}{\partial\xi}(\rho\phi') + \rho\phi'\chi_3 \tag{4.33}$$

The general transport equation is written in the inertial axi-symmetric cylindrical co-ordinate system as

$$\underbrace{\frac{\partial}{\partial x}(\rho u\phi)}_{a} + \underbrace{\frac{1}{r}\frac{\partial}{\partial r}(r\rho v\phi)}_{b} = \underbrace{\frac{\partial}{\partial x}\left(\Gamma\frac{\partial\phi}{\partial x}\right)}_{c} + \underbrace{\frac{1}{r}\frac{\partial}{\partial r}\left(r\Gamma\frac{\partial\phi}{\partial r}\right)}_{d} + \underbrace{S_\phi}_{e} - \underbrace{\frac{\partial(\rho\phi)}{\partial t}}_{f} \tag{4.34}$$

where Γ is used instead of Γ_ϕ to reduce the number of indices. Each term is identified so that the transformation can be followed more easily. Substituting *eqs*(4.21), (4.22), (4.23) in *eq*(4.34) to get

$$\underbrace{\frac{\partial}{\partial t}(\rho\phi') + \left\{\frac{\dot{\chi}_1}{\chi_1}\xi + \chi_1\frac{\partial}{\partial t}\left(\frac{\chi_2}{\chi_1}\right)\right\}\frac{\partial}{\partial \xi}(\rho\phi')}_{f} + \underbrace{\chi_1\frac{\partial}{\partial \xi}(\rho u\phi')}_{a} +$$

$$\underbrace{\frac{1}{r}\frac{\partial}{\partial r}(r\rho v\phi')}_{b} = \underbrace{\chi_1\frac{\partial}{\partial \xi}\left(\chi_1\Gamma\frac{\partial \phi'}{\partial \xi}\right)}_{c} + \underbrace{\frac{1}{r}\frac{\partial}{\partial r}\left(r\Gamma\frac{\partial \phi'}{\partial r}\right)}_{d} + \underbrace{S_{\phi'}}_{e} \tag{4.35}$$

and using *eq*(4.33)

$$\underbrace{\frac{\partial}{\partial t}(\rho\phi') + \left\{\frac{\dot{\chi}_1}{\chi_1}\xi + \chi_1\frac{\partial}{\partial t}\left(\frac{\chi_2}{\chi_1}\right)\right\}\frac{\partial}{\partial \xi}(\rho\phi')}_{f}$$

$$+ \underbrace{\chi_1 U_G\frac{\partial}{\partial \xi}(\rho\phi') + \chi_1\chi_3\rho\phi' + \chi_1\frac{\partial}{\partial \xi}(\rho\bar{u}\phi')}_{a} + \underbrace{\frac{1}{r}\frac{\partial}{\partial r}(r\rho v\phi')}_{b}$$

$$= \underbrace{\chi_1\frac{\partial}{\partial \xi}\left(\chi_1\Gamma\frac{\partial \phi'}{\partial \xi}\right)}_{c} + \underbrace{\frac{1}{r}\frac{\partial}{\partial r}\left(r\Gamma\frac{\partial \phi'}{\partial r}\right)}_{d} + \underbrace{S_{\phi'}}_{e} \tag{4.36}$$

where the transformed source terms are given in Table 4.2. By substituting $\alpha = 1$ and then $\alpha = 0$ in *eqs*(4.9), (4.16) and (4.27) it can be shown that

$$\chi_1\chi_3 = -\frac{\dot{\chi}_1}{\chi_1} \tag{4.37}$$

The terms '*f*' and '*a*' of *eq*(4.36) are written as

$$\frac{\partial}{\partial t}(\rho\phi') + \left\{\frac{\dot{\chi}_1}{\chi_1}\xi + \chi_1\frac{\partial}{\partial t}\left(\frac{\chi_2}{\chi_1}\right)\right\}\frac{\partial}{\partial \xi}(\rho\phi') + \chi_1 U_G\frac{\partial}{\partial \xi}(\rho\phi') +$$
$$\chi_1\chi_3\rho\phi' + \chi_1\frac{\partial}{\partial \xi}(\rho\bar{u}\phi')$$

Substituting *eq*(4.37) and rearranging

$$\frac{\partial}{\partial t}(\rho\phi') + (\rho\phi')\left\{\frac{-\dot{\chi}_1}{\chi_1}\right\} + \left\{\frac{\dot{\chi}_1}{\chi_1}\xi + \chi_1\frac{\partial}{\partial t}\left(\frac{\chi_2}{\chi_1}\right)\right\}\frac{\partial}{\partial \xi}(\rho\phi') +$$
$$\chi_1 U_G\frac{\partial}{\partial \xi}(\rho\phi') + \chi_1\frac{\partial}{\partial \xi}(\rho\bar{u}\phi') \tag{4.38}$$

Table 4.2 Transformed source terms in the ξ, r, t system

QUANTITY	ϕ	$S_{\phi'}$
Continuity	1	0
Radial Momentum	v	$-(\partial p/\partial r) - (\mu_{eff} v/r^2)$ $+\chi_1 \frac{\partial}{\partial \xi}\left(\mu_{eff}\frac{\partial u}{\partial r}\right) + \frac{1}{r}\frac{\partial}{\partial r}\left(r\mu_{eff}\frac{\partial v}{\partial r}\right) - \mu_{eff}\frac{v}{r^2}$
Axial Momentum	u	$-\chi_1(\partial p/\partial \xi)$ $+\chi_1 \frac{\partial}{\partial \xi}\left(\chi_1\mu_{eff}\frac{\partial u}{\partial \xi}\right) + \frac{1}{r}\frac{\partial}{\partial r}\left(r\mu_{eff}\chi_1\frac{\partial v}{\partial \xi}\right)$
Energy	h	Discussed in the next chapter
Turbulence Energy	K	$G - C_D\rho\epsilon$
Energy Dissipation	ϵ	$C_1 G\epsilon/K - C_2\rho\epsilon^2/K$

At this point attention is focused on only the first two terms of the above expression. These can be rewritten as

$$\chi_1\left[\frac{1}{\chi_1}\frac{\partial}{\partial t}(\rho\phi') + (\rho\phi')\left\{\frac{0-\dot{\chi}_1}{\chi_1^2}\right\}\right]$$

which is the expansion of

$$\chi_1\frac{\partial}{\partial t}\left(\frac{\rho\phi'}{\chi_1}\right)$$

Therefore

$$\frac{\partial}{\partial t}(\rho\phi') + (\rho\phi')\left\{\frac{-\dot{\chi}_1}{\chi_1}\right\} = \chi_1\frac{\partial}{\partial t}\left(\frac{\rho\phi'}{\chi_1}\right)$$

Substituting *eq*(4.37) and the above equation in *eq*(4.36) gives

$$\left\{\frac{\dot{\chi}_1}{\chi_1}\xi + \chi_1\frac{\partial}{\partial t}\left(\frac{\chi_2}{\chi_1}\right)\right\}\frac{\partial}{\partial \xi}(\rho\phi') + \chi_1 U_G\frac{\partial}{\partial \xi}(\rho\phi') + \chi_1\frac{\partial}{\partial t}\left(\frac{\rho\phi'}{\chi_1}\right) + \chi_1\frac{\partial}{\partial \xi}(\rho\overline{u}\phi') +$$
$$\frac{1}{r}\frac{\partial}{\partial r}(r\rho v\phi') = \chi_1\frac{\partial}{\partial \xi}\left(\chi_1\Gamma\frac{\partial \phi'}{\partial \xi}\right) + \frac{1}{r}\frac{\partial}{\partial r}\left(r\Gamma\frac{\partial \phi'}{\partial r}\right) + S_{\phi'} \qquad (4.39)$$

Attention is now focused on the first two terms of *eq*(4.39)

$$\left\{\frac{\dot{\chi}_1}{\chi_1}\xi + \chi_1\frac{\partial}{\partial t}\left(\frac{\chi_2}{\chi_1}\right)\right\}\frac{\partial}{\partial \xi}(\rho\phi') + \chi_1 U_G\frac{\partial}{\partial \xi}(\rho\phi')$$

which can be written as

$$\chi_1 \left\{ \frac{\dot{\chi}_1}{\chi_1^2}\xi + \frac{\partial}{\partial t}\left(\frac{\chi_2}{\chi_1}\right) \right\} \frac{\partial}{\partial \xi}(\rho\phi') + \chi_1 U_G \frac{\partial}{\partial \xi}(\rho\phi')$$

Substituting $-\dot{\chi}_1/\chi_1$ from *eq*(4.37) in the above expression yields

$$-\chi_1 \left\{ \chi_3\xi - \frac{\partial}{\partial t}\left(\frac{\chi_2}{\chi_1}\right) \right\} \frac{\partial}{\partial \xi}(\rho\phi') + \chi_1 U_G \frac{\partial}{\partial \xi}(\rho\phi') \tag{4.40}$$

Recall *eq*(4.25) as

$$U_G = \chi_3\xi + \chi_4$$

Comparing the above equation with expression (4.40) it may be seen that if it can be proven that

$$\chi_4 = -\frac{\partial}{\partial t}\left(\frac{\chi_2}{\chi_1}\right)$$

then expression (4.40) will vanish. The value of χ_4 is given by *eq*(4.28) as

$$\chi_4 = (1-\alpha)\dot{x}_l - \xi_l \frac{(1-\alpha)(\dot{x}_l - \dot{x}_s)}{(\xi_l - 1)}$$

Let

$$A = -\frac{\partial}{\partial t}\left(\frac{\chi_2}{\chi_1}\right) = \frac{\dot{\chi}_1\chi_2 - \dot{\chi}_2\chi_1}{\chi_1^2} \tag{4.41}$$

Substituting $\alpha = 1$ in *eqs*(4.9), (4.10), (4.16) and (4.17) yields

$$\chi_1 = \frac{\xi_l}{x_l} \quad \text{and} \quad \dot{\chi}_1 = \frac{\xi_l \dot{x}_l}{x_l^2}$$

$$\chi_2 = 0 \quad \text{and} \quad \dot{\chi}_2 = 0$$

Substituting the above equations in *eq*(4.41) gives, for $\alpha = 1$

$$A = 0$$

Also, from *eq*(4.28) it is obvious that for $\alpha = 1$

$$\chi_4 = 0$$

Therefore

$$A = \chi_4$$

Substituting $\alpha = 0$ in *eqs*(4.9), (4.10), (4.16), (4.17) and (4.28) yields

$$\chi_1 = \frac{(\xi_l - 1)}{(x_l - x_s)}$$

$$\dot{\chi}_1 = \frac{(1 - \xi_l)(\dot{x}_l - \dot{x}_s)}{(x_l - x_s)^2}$$

$$\chi_2 = \xi_l - \frac{x_l(\xi_l - 1)}{(x_l - x_s)}$$

$$\dot{\chi}_2 = (1 - \xi_l)\frac{\dot{x}_l(x_l - x_s) - x_l(\dot{x}_l - \dot{x}_s)}{(x_l - x_s)^2}$$

$$\chi_4 = \dot{x}_l - \frac{\xi_l(\dot{x}_l - \dot{x}_s)}{(\xi_l - 1)} = \frac{(\xi_l \dot{x}_s - \dot{x}_l)}{(\xi_l - 1)} \tag{4.42}$$

Recall *eq*(4.41):

$$A = -\frac{\partial}{\partial t}\left(\frac{\chi_2}{\chi_1}\right) = \frac{\dot{\chi}_1\chi_2 - \dot{\chi}_2\chi_1}{\chi_1^2}$$

Substitution of χ_1, χ_2, $\dot{\chi}_1$ and $\dot{\chi}_2$ in the above equation and algebraic manipulation yields

$$A = \frac{-\dot{x}_l x_l - \dot{x}_s x_s \xi_l + x_l \dot{x}_s \xi_l + \dot{x}_l x_s}{(x_l - x_s)(\xi_l - 1)}$$

where the numerator can be factored as $(x_l - x_s)(\xi_l \dot{x}_s - \dot{x}_l)$ and further simplification yields

$$A = \frac{(\xi_l \dot{x}_s - \dot{x}_l)}{(\xi_l - 1)} \tag{4.43}$$

which is identical to *eq*(4.42). It has therefore been shown that for the entire domain ($\alpha = 1$ and $\alpha = 0$)

$$\chi_4 = -\frac{\partial}{\partial t}\left(\frac{\chi_2}{\chi_1}\right) \tag{4.44}$$

Hence expression (4.40) vanishes and *eq*(4.39) simplifies to

$$\chi_1 \frac{\partial}{\partial t}\left(\frac{\rho\phi'}{\chi_1}\right) + \chi_1 \frac{\partial}{\partial \xi}(\rho\bar{u}\phi') + \frac{1}{r}\frac{\partial}{\partial r}(r\rho v\phi') = \chi_1 \frac{\partial}{\partial \xi}\left(\chi_1 \Gamma \frac{\partial \phi'}{\partial \xi}\right) + \frac{1}{r}\frac{\partial}{\partial r}\left(r\Gamma \frac{\partial \phi'}{\partial r}\right) + S_{\phi'}$$

Dropping the bar and the prime and dividing by χ_1 the following form is obtained which is the final form of the general transport equation in the transformed coordinate system.

$$\frac{\partial}{\partial t}\left(\frac{\rho\phi}{\chi_1}\right)+\frac{\partial}{\partial \xi}(\rho U\phi) \;+\; \frac{1}{\chi_1 r}\frac{\partial}{\partial r}(r\rho v\phi)-\frac{\partial}{\partial \xi}\left(\chi_1\Gamma\frac{\partial \phi}{\partial \xi}\right)- \frac{1}{\chi_1 r}\frac{\partial}{\partial r}\left(r\Gamma\frac{\partial \phi}{\partial r}\right)-\frac{S_\phi}{\chi_1}=0 \tag{4.45}$$

Integration of the transformed equation

Eq(4.45) is integrated over a cylindrical cell of dimensions $r\,dr\,d\xi\,(1)$. The factor (1) stands for the angular dimension of the cell, which is specified as 1 radian. The volume of the cell is given by $r\,dr\,d\xi\,(1)/\chi_1$ as ξ is dimensionless. χ_1 is defined by *eq*(4.9). *Eq*(4.45) is integrated over the control volume

$$\begin{aligned}&\int\int\frac{\partial}{\partial t}\left(\frac{\rho\phi}{\chi_1}\right)r\,dr\,d\xi\,(1)+\int\int\frac{\partial}{\partial \xi}(\rho u\phi)r\,dr\,d\xi\,(1)+\\&\int\int\frac{1}{\chi_1 r}\frac{\partial}{\partial r}(r\rho v\phi)r\,dr\,d\xi\,(1)-\int\int\frac{\partial}{\partial \xi}\left(\chi_1\Gamma\frac{\partial \phi}{\partial \xi}\right)r\,dr\,d\xi\,(1)-\\&\int\int\frac{1}{\chi_1 r}\frac{\partial}{\partial r}\left(r\Gamma\frac{\partial \phi}{\partial r}\right)r\,dr\,d\xi\,(1)-\int\int\frac{S_\phi}{\chi_1}r\,dr\,d\xi\,(1)=0\end{aligned} \tag{4.46}$$

which yields

$$\begin{aligned}&\frac{(\rho\phi/\chi_1-\rho^o\phi^o/\chi_1^o)V}{\Delta t}+(\rho u\phi)_e\,a_e-(\rho u\phi)_w\,a_w+(\rho v\phi)_n\,a_n-(\rho v\phi)_s\,a_s-\\&\left(\chi_1\Gamma\frac{\partial \phi}{\partial \xi}\right)a_e+\left(\chi_1\Gamma\frac{\partial \phi}{\partial \xi}\right)a_w-\left(\Gamma\frac{\partial \phi}{\partial r}\right)a_n+\left(\Gamma\frac{\partial \phi}{\partial r}\right)a_s-S\frac{V}{\chi_1}=0\end{aligned} \tag{4.47}$$

The above equation is the integrated form of the transport equation, *eq*(4.45). The coefficients a_e, a_w, a_n and a_s represent the areas of the east, west, north and south walls of the cell. The east and west cell wall areas are given by

$$a_e=a_w=r\,\Delta r\,(1) \tag{4.48}$$

and the north and south cell wall areas are given by

$$a_n = \frac{\Delta\xi}{\chi_1} r_n(1) \tag{4.49}$$

$$a_s = \frac{\Delta\xi}{\chi_1} r_s(1) \tag{4.50}$$

and the cell volume is given by

$$V = r\,\Delta r\,\Delta\xi\,(1)/\chi_1 \tag{4.51}$$

The integrated form of the mass conservation equation is obtained by substituting $\phi = 1$ and $S = 0$ in *eq*(4.47).

$$\frac{(\rho/\chi_1 - \rho^o/\chi_1^o)V}{\Delta t} + (\rho u)_e\, a_e - (\rho u)_w\, a_w + (\rho v)_n\, a_n - (\rho v)_s\, a_s = 0 \tag{4.52}$$

Multiplying *eq*(4.52) by ϕ_p and subtracting from *eq*(4.47) yields the final form of the integrated equation which is discretized using the hybrid difference scheme.

$$\begin{aligned}
&\frac{(\phi_p - \phi_p^o)(\rho^o V/\chi_1^o)}{\Delta t} + a_e(\rho u)_e(\phi_e - \phi_p) - \\
&a_w(\rho u)_w(\phi_w - \phi_p) + a_n(\rho v)_n(\phi_n - \phi_p) - a_s(\rho v)_s(\phi_s - \phi_p) - \\
&\left(\frac{\chi_1\Gamma}{\Delta\xi}\right) a_e(\phi_e - \phi_p) + \left(\frac{\chi_1\Gamma}{\Delta\xi}\right) a_w(\phi_w - \phi_p) - \left(\frac{\Gamma}{\Delta r}\right) a_n(\phi_n - \phi_p) + \\
&\left(\frac{\Gamma}{\Delta r}\right) a_s(\phi_s - \phi_p) - S\frac{V}{\chi_1} = 0
\end{aligned} \tag{4.53}$$

Treatment of the axial momentum

Computation of the axial momentum requires special consideration to account for the additional Lagrangian component of the axial velocity. When the 'u' velocity is being solved for, the discretized Eulerian equation is written as

$$a_p u_p = \Sigma a_i u_i + a_p^o u_p^o + Su \tag{4.54}$$

Rearranging *eq*(4.29) gives

$$u = \overline{u} + U_G$$

Substitute in *eq*(4.54)

$$a_p(\overline{u}_p + U_{G_p}) = \Sigma a_i(\overline{u}_i + U_{G_i}) + a_p^o(\overline{u}_p^o + U_{G_p}^o) + Su \quad (4.55)$$

$$a_p\overline{u}_p = \Sigma a_i\overline{u}_i + a_p^o\overline{u}_p^o + \overline{Su} \quad (4.56)$$

where $\overline{Su}$ is defined as

$$\overline{Su} = Su + \{-a_pU_{G_p} + a_nU_{G_n} + a_sU_{G_s} + a_eU_{G_e} + a_wU_{G_w} + a_p^oU_{G_p}^o\}$$

but

$$a_p = a_n + a_s + a_e + a_w + a_p^o$$

which is substituted to yield

$$\begin{aligned}\overline{Su} = Su \quad + \quad & \{a_nU_{G_n} + a_sU_{G_s} + a_eU_{G_e} + a_wU_{G_w} - \\ & a_nU_{G_p} - a_sU_{G_p} - a_eU_{G_p} - a_wU_{G_p} - a_p^oU_{G_p} + a_p^oU_{G_p}^o\}\end{aligned} \quad (4.57)$$

but

$$U_{G_n} = U_{G_s} = U_{G_p}$$

which results in the simplification

$$\overline{Su} = Su + \{a_e(U_{G_e} - U_{G_p}) + a_w(U_{G_w} - U_{G_p}) + a_p^o(U_{G_p}^o - U_{G_p})\} \quad (4.58)$$

The source term of the axial velocity therefore has extra terms as outlined in the above equation to account for the Lagrangian effects.

4.3.2 Free surface treatment

The surface treatment zone

The transformation developed in the previous section is quite general, so that if required the mesh can simultaneously and arbitrarily expand in the region where

$\alpha = 1$ and contract where $\alpha = 0$. The mesh used is shown in Figure 4.5. The 'Fluid' and 'Free Surface' regions are separated by the wall between the cell layers '$I = ILVL$' and '$I = ILVL + 1$'. The Free Surface Zone is the region of the domain where the surface profile is expected to occur in the solution. The surface is tracked *only* in this region as it is computationally inefficient to carry out the search in the regions known to be 'full' of fluid. The Free Surface Zone overlaps a small portion of the Fluid Region to ensure that the lower regions of the free surface are tracked accurately.

Derivation of the free surface boundary conditions

The boundary conditions at the free surface are that the normal and tangential stresses are zero [62,44]. The stress tensor for an incompressible fluid is

$$\tau_{i,j} = -P\delta_{i,j} + \mu\left(\frac{\partial u_j}{\partial x_i} + \frac{\partial u_i}{\partial x_j}\right) \tag{4.59}$$

which also represents the flowrate of the ith component of the momentum in the jth direction. The flux normal to the free surface is zero, therefore the free surface condition is [44]

$$\tau_{i,j}n_j = 0 \tag{4.60}$$

where 'n_j' is a unit normal to the free surface. For a two–dimensional case the above condition expands to [44]

$$P - 2\mu\left\{n_x n_x\frac{\partial u}{\partial x} + n_x n_r\left(\frac{\partial u}{\partial r} + \frac{\partial v}{\partial x}\right) + n_r n_r\frac{\partial v}{\partial r}\right\} = 0 \tag{4.61}$$

$$\mu\left\{2n_x m_x\frac{\partial u}{\partial x} + (n_x m_r + n_r m_x)\left(\frac{\partial u}{\partial r} + \frac{\partial v}{\partial x}\right) + 2n_r m_r\frac{\partial v}{\partial r}\right\} = 0 \tag{4.62}$$

where 'n_x' and 'n_r' are the 'x' and 'r' components of the normal 'n' to the surface

$$x = \eta(r,t) \tag{4.63}$$

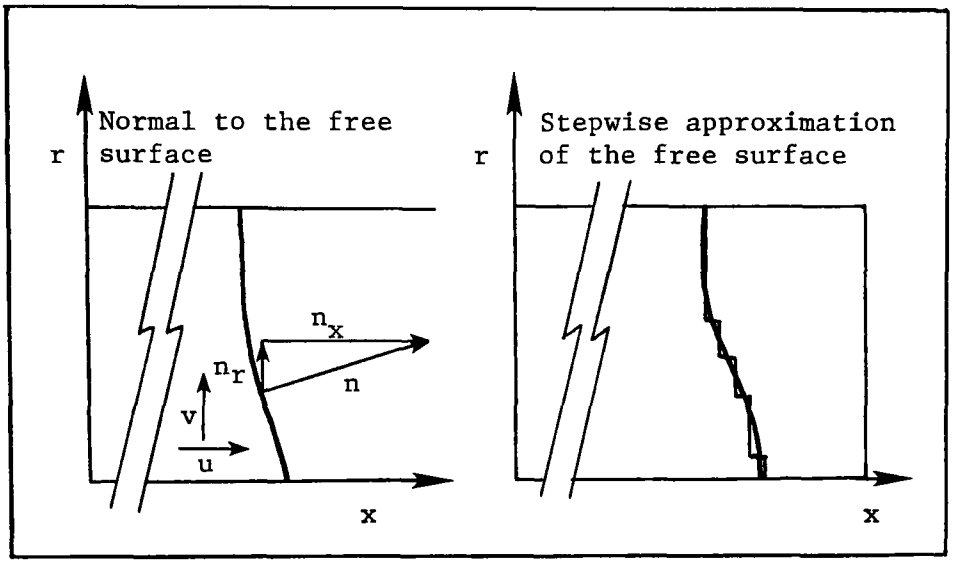

Figure 4.6 Free surface shape and approximation

shown in Figure 4.6. The tangential components are perpendicular to the normal components and given as

$$m_x = n_r; \qquad m_r = n_x \tag{4.64}$$

By geometrical considerations it can be shown that [44]

$$n_x = \left\{1 + \left(\frac{\partial \eta}{\partial r}\right)^2\right\}^{-1/2} \tag{4.65}$$

and

$$n_r = \frac{\partial \eta}{\partial r}\left\{1 + \left(\frac{\partial \eta}{\partial r}\right)^2\right\}^{-1/2} \tag{4.66}$$

Assuming that the slope of the surface defined by *eq*(4.63) is small

$$\frac{\partial \eta}{\partial r} \approx 0 \tag{4.67}$$

eq(4.65) and (4.66) reduce to

$$n_r \approx 0; \quad \textit{and} \quad n_x \approx 1 \tag{4.68}$$

which simplifies *eq*(4.61) and (4.62) to

$$P - 2\mu \left\{ \frac{\partial u}{\partial x} \right\} = 0 \tag{4.69}$$

$$\mu \left(\frac{\partial u}{\partial r} + \frac{\partial v}{\partial x} \right) = 0 \tag{4.70}$$

It has been shown [38,44] that for fluids with low viscosity (for example, water) the viscous term in *eq*(4.69) can be neglected and the boundary condition for pressure is simply [44]

$$P \approx 0 \tag{4.71}$$

It has been assumed that the slope of the surface is small. It can be seen from Figure 4.6 that in order to have a zero flux across the surface, u has to be approximately zero at the surface. If $u \approx 0$ at the surface then it's variation along the surface is also very small, *i.e.*, $\partial u/\partial r \approx 0$. This simplifies *eq*(4.70) to [44]

$$\frac{\partial v}{\partial x} \approx 0 \tag{4.72}$$

The simplified free surface conditions are therefore given by *eq*(4.71) for the normal stress and *eq*(4.72) for the tangential stress.

Imposition of the boundary conditions near the free surface

Techniques have been developed to impose the free surface boundary conditions (specified by *eq*(4.71) and *eq*(4.72)) using the Finite Volume Method. The free surface shape is approximated in a 'step-wise manner' and special boundary conditions are imposed at the cells in the vicinity of the free surface. Figure 4.6 shows a typical free surface profile and a step-wise approximation of the free surface.

The scalar cells in the Free Surface Zone are identified by an index, '$ISUR$', the value of which determines whether the cell is 'empty' or 'full' or if the free surface

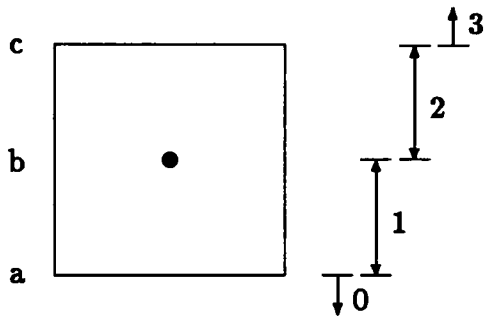

FLUID LEVEL	$ISUR_p$	BOUNDARY CONDITION
level < a	0	Impose zero U, V, P, no continuity.
a ≤ level < b	1	Impose zero U, V, $P_s = \frac{1}{2}\rho u_s \lvert u_s \rvert$ Free slip for V_{i-1}, no continuity.
b ≤ level < c	2	Impose $P_s = \frac{1}{2}\rho u_s \lvert u_s \rvert$, free slip for V_i No continuity.
level > c	3	No boundary conditions required.

Figure 4.7 Indices for the free surface cells

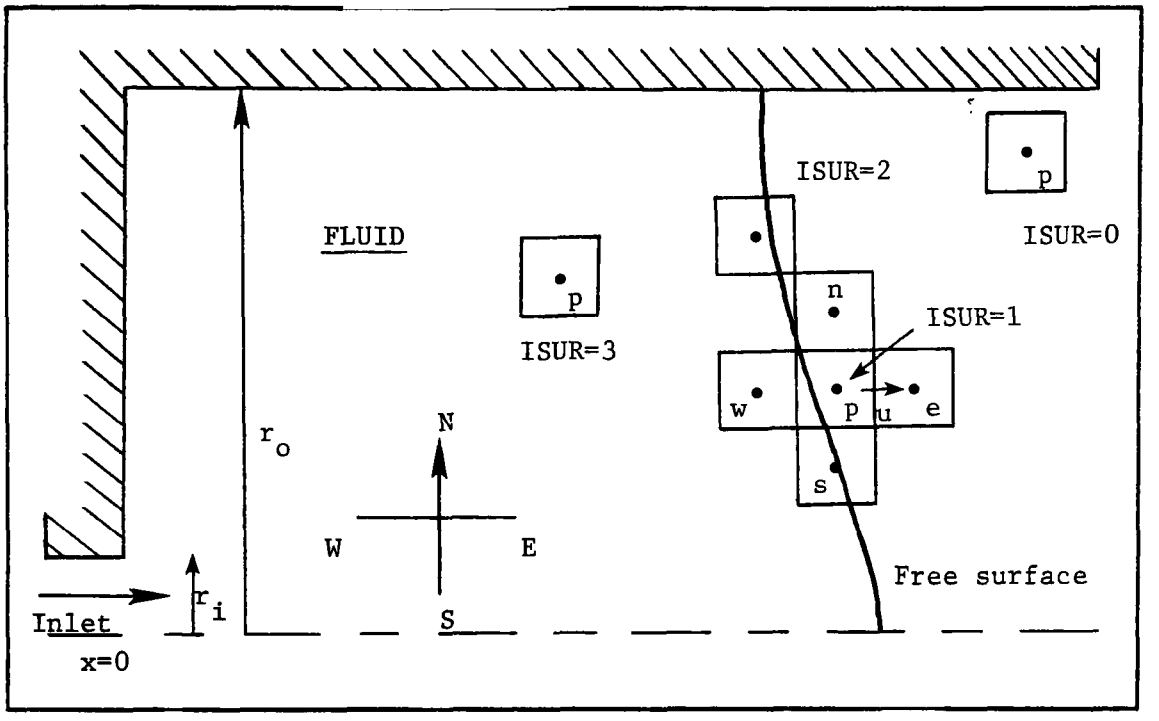

Figure 4.8 Cells in the free surface zone

passes through it. Figure 4.7 shows a typical scalar cell in the Free Surface Zone and tabulates the value of '*ISUR*' as a function of the fluid level in the cell and the applicable boundary conditions. Attention should be focused only on the first two columns; the boundary conditions are summarized in the third column and will be discussed in subsequent paragraphs. If '*ISUR*' is assigned a value of '0' the scalar cell is 'empty' *i.e.* the free surface is *below* the cell. If '$ISUR = 1$' the cell is less than or equal to half full; if '$ISUR = 2$' the cell is more than half full. The free surface passes through the scalar cell when $ISUR$ has a value of 1 or 2. If '$ISUR = 3$' the cell is completely full of fluid *i.e.* the free surface is *above* the cell. The boundary conditions for the variable ϕ are applied by the manipulation of the terms in the algebraic equation

$$(a_p - Sp)\phi_p = a_n\phi_n + a_s\phi_s + a_e\phi_e + a_w\phi_w + Su \tag{4.73}$$

BOUNDARY CONDITIONS FOR $ISUR_p = 0$

A value of $ISUR_p = 0$ implies that the scalar cell p is empty and the free surface is below (or to the west of) the cell. Figure 4.8 shows a typical cell with $ISUR_p = 0$. The cell is decoupled from the domain by setting a_n, a_s, a_e and a_w to zero in *eq*(4.73) for all the ϕ's. It is possible that the west neighbor of the cell may contain the free surface; therefore the coefficient a_e of the west neighbor ϕ_w is also set to zero. The field value of ϕ_p is set to zero in the final solution by setting

$$Su = 0; \quad \text{and} \quad Sp = -B \tag{4.74}$$

where B is a very large number, typically of the order of 10^{30}.

BOUNDARY CONDITIONS FOR $ISUR_p = 3$

A value of $ISUR_p = 3$ implies that the scalar cell p is full and the free surface is above (or to the east of) the cell. Figure 4.8 illustrates a cell with $ISUR_p = 3$. In this case computations are carried out as usual and no additional boundary conditions are required.

BOUNDARY CONDITIONS FOR $ISUR_p = 1$

A value of $ISUR_p = 1$ implies that the scalar cell p is less than half full and the free surface is below (or to the west of) the node. The boundary conditions for this case are described in the following paragraphs and reference is made to Figure 4.9(a) in the discussion.

u velocity conditions

It can be seen from Figures 4.8 and 4.9(a) that the 'u_p' velocity cell corresponding to the node 'p' does not contain any fluid, therefore it is decoupled from the domain by setting a_n, a_s, a_e and a_w to zero in *eq*(4.73) for $\phi = u_p$. The 'u_w' cell to the west contains the free surface; the coefficient a_e of the west neighbor is also set to zero. This constitutes a zero flux condition on the east boundary of the 'u_w' cell through

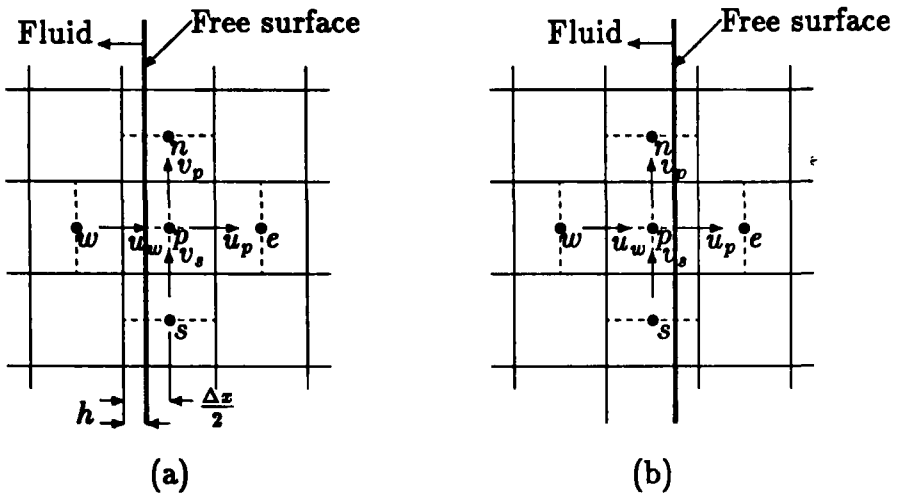

Figure 4.9 Free surface treatment

which the free surface passes. The field value of u_p is set to zero in the final solution by setting

$$Su = 0; \quad \text{and} \quad Sp = -B \tag{4.75}$$

v velocity conditions

It can be seen from Figure 4.9(a) that the 'v_p' velocity cell corresponding to the node p is mostly empty. The velocity v_p is therefore not computed, and the cell is decoupled from the domain by setting a_n, a_s, a_e and a_w to zero in *eq*(4.73) for $\phi = v$. The v_w cell to the west is full and for the computation of v it is assumed that the free surface is passing through the east wall of this cell. The zero shear stress condition specified by *eq*(4.72) is imposed by setting the coefficient a_e of the cell corresponding to v_w to zero. The field value of v_p is set to zero in the final solution by setting

$$Su = 0; \quad \text{and} \quad Sp = -B \tag{4.76}$$

Scalar conditions

Computation is carried out for the scalar variable, ϕ_p, however, the flux through the east boundary is set to zero by setting $a_e = 0$ as the neighboring cell to the

east is empty. Also the coefficient a_w of the east neighbor ϕ_e is set to zero. The coefficients a_n and a_s are unaltered.

Pressure conditions

The free surface passes through the scalar cell to the west of the node p. The actual location and orientation of the free surface is not known. For the present treatment it is assumed that the free surface profile is horizontal within each cell. The distance of the free surface from the western wall of the cell as specified by 'h' in Figure 4.9(a) is unknown. If the velocity u_w is known then the momentum (in the vertical direction) of the fluid at the western wall can be expressed as

$$\varphi = \frac{1}{2}\rho u_w |u_w| \tag{4.77}$$

Assuming that the fluid rises vertically upwards (towards the east direction in Figure 4.9) until its kinetic energy is converted to potential energy, the distance 'h' can be computed from

$$h = \frac{1}{\rho g}\varphi \tag{4.78}$$

The static pressure at the western wall of the cell is expressed by the hydrostatic component

$$P_{hyd} = \varphi = \rho g h \tag{4.79}$$

as the free surface pressure is zero by *eq*(4.71). This pressure can be attained by imposing the nodal pressure

$$P_p = \varphi - \rho g \frac{\Delta x}{2} \tag{4.80}$$

where $\Delta x/2$ is the distance from the node p to the west wall of the cell. The above pressure condition assures satisfaction of *eq*(4.71) at the free surface.

In the Finite Volume Method the pressure field is repeatedly corrected through the iterative process by a pressure corrections (PP) which are added to the nodal pressures (P). The pressure at node 'p' is defined by *eq*(4.80), therefore further

pressure correction at this node is not required. The pressure correction at node 'p' is set to zero by setting a_n, a_s, a_e and a_w to zero in *eq*(4.73) for $\phi = PP$.

BOUNDARY CONDITIONS FOR $ISUR_p = 2$

A value of $ISUR_p = 2$ implies that the scalar cell p is more than half full and the free surface is above (or to the east of) the node. The boundary conditions for this case are described in the following paragraphs and reference is made to Figure 4.9(b) in the discussion.

u velocity conditions

It can be seen from Figure 4.9(b) that the 'u_p' velocity cell corresponding to the node 'p' contains fluid but the east neighbor 'u_e' does not contain any fluid. The zero flux condition is therefore applied to the east wall of the cell 'p' by setting the coefficient a_e to zero.

v velocity conditions

The v_p cell is almost full and for the computation of v it is assumed that the free surface is passing through the east wall of this cell. The zero shear stress condition specified by *eq*(4.72) is imposed by setting the coefficient a_e to zero.

Scalar conditions

Computation is carried out for the scalar variable, ϕ_p, however, the flux through the east boundary is set to zero by setting $a_e = 0$ as the neighboring cell to the east is empty. Also the coefficient a_w of the east neighbor ϕ_e is set to zero.

Pressure conditions

The free surface passes through the scalar cell to the east of the node p, therefore the node is within the fluid. The actual location and orientation of the free surface is not known. It is assumed that the free surface profile is horizontal and 'close' to the east boundary of the cell. This assumption is not unreasonable as the mesh

is quite fine in the Free Surface Region. The pressure condition is imposed on the node 'e' corresponding to the east neighbor of the cell, such that the pressure at the surface is zero as specified by $eq(4.71)$. The following pressure is imposed

$$P_e = \frac{1}{2}\rho u_p|u_p| - \rho g\frac{\Delta x}{2} \tag{4.81}$$

The pressure correction at node 'e' is set to zero by setting a_n, a_s, a_e and a_w to zero in $eq(4.73)$ for $\phi = PP$. The pressure at node 'e' is defined by $eq(4.81)$, therefore, further pressure correction at this node is not required.

Tracking the free surface

The gravitational acceleration is accounted for in the computations, therefore the nodal pressures include the hydrostatic component. The free surface is tracked during the iterative process by searching for the 'zero' pressure profile in the domain. At the beginning of each iteration the nodes in the free surface zone are indexed on the basis of the spatial location of the free surface. The free surface shape for the initial iteration of each time step can be obtained from either

1. An assumption of a flat surface
2. Experimental data
3. A previous time step solution.

The algorithm to track the free surface is explained with reference to the flow-chart in Figure 4.10. Each item in the flowchart is numbered and explained in the following. The search is carried out for each row of scalar cells scanning from the south to the north end of the domain.

1. The procedure employed is the same for each J, and repeated for $J = 2$ to $J = NJ - 1$.

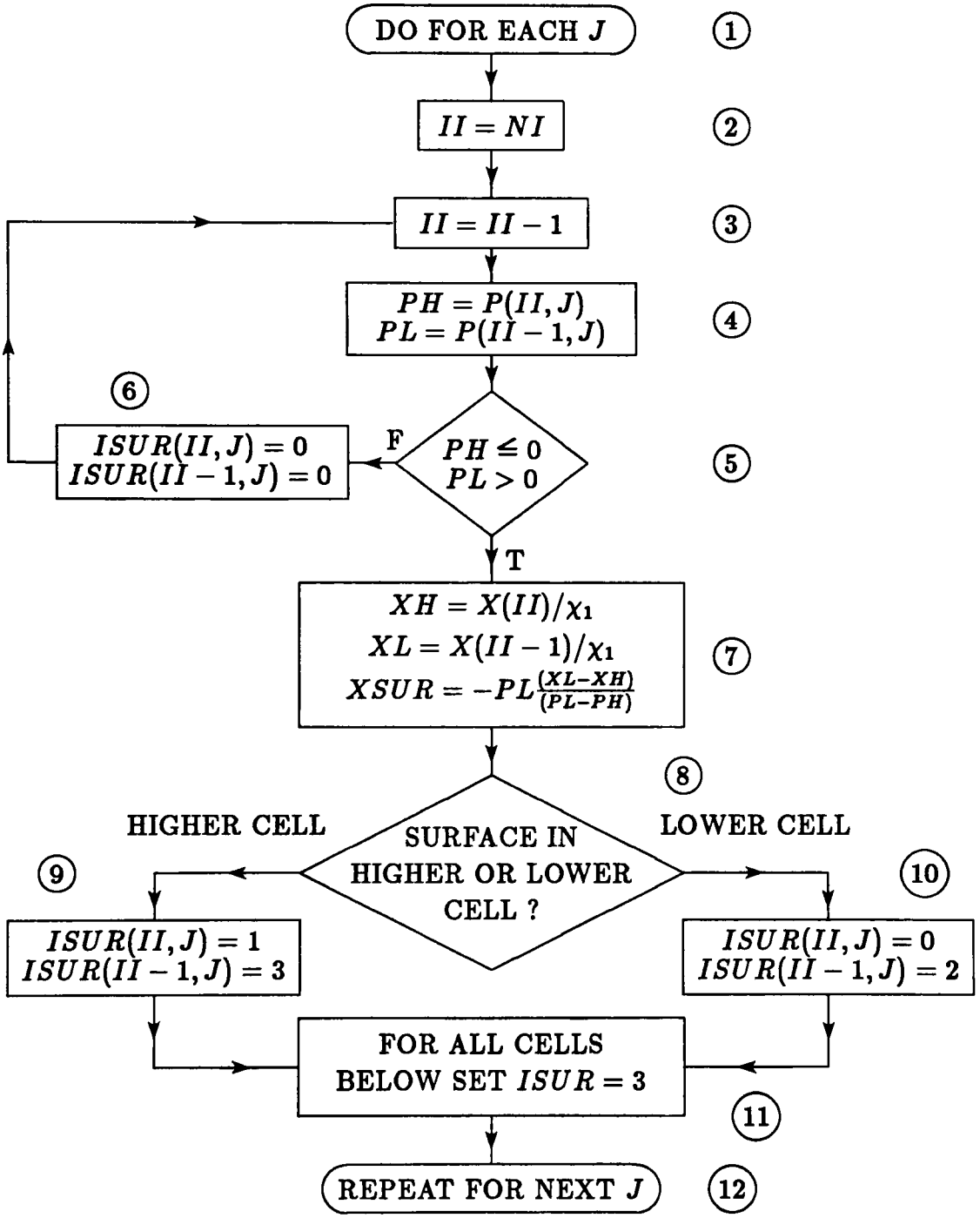

Figure 4.10 Free surface tracking algorithm

2. The variable 'II' is initialized to NI. This variable is used as the 'I' coordinate of the node pair $\{(II, J), (II-1, J)\}$ between which the free surface is searched.

3. II is reduced by one. The first node pair between which the search is made is $\{(NI-1, J), (NI-2, J)\}$. If this step is called after step (6), the search is repeated for the next pair one node to the west.

4. The temporary variables 'PH' and 'PL' are defined. 'PH' is the pressure at the 'higher' node in the pair, and 'PL' is the pressure at the 'lower' node.

5. The presence or absence of the free surface is detected between the nodes by checking the pressures PH and PL. If both PH and PL are zero then the free surface is below (or to the west of) the node pair. If the free surface is between the nodes then $PH \leq 0$ and $PL > 0$.

6. If the free surface is to the west of the node pair then both the cells (II, J) and $(II-1, J)$ are empty, therefore $ISUR(II, J) = 0$ and $ISUR(II-1, J) = 0$. Step (3) is carried out next so that the next cell pair to the west is searched for the free surface.

7. If the free surface is isolated between the nodes (II, J) and $(II-1, J)$ from step (5), then its location is determined by a linear interpolation between the pressures PH, PL, as the surface pressure is zero (from eq(4.71)).

8. Once the location of the free surface is known, geometric considerations are used to determine if the free surface is in the higher cell (II) or the lower cell $(II-1)$. If the free surface is in the higher cell, then step (9) is followed, and if it is in the lower cell then step (10) is followed.

9. If the surface is in the higher cell, then it is between the west wall of the cell and the node (II). Also, the lower cell is full of fluid. In this case $ISUR(II, J) = 1$ and $ISUR(II-1, J) = 3$.

10. If the free surface is in the lower cell, then it is between the node $(II-1, J)$ and the east wall of the cell. Also the higher cell is empty. In this case $ISUR(II, J) = 0$ and $ISUR(II-1, J) = 2$.

11. All the cells to the west of the pair containing the free surface are assumed to be full, therefore they are all assigned an index of $ISUR = 3$. These indices are only assigned to the cells in the free surface zone in order to conserve CPU time and memory requirements.

12. The next row to the north $(J = J + 1)$ is searched for the free surface profile starting from step (1).

The free surface shape is updated on the basis of the nodal pressures by the steps outlined above. As convergence is approached the nodal pressures and the nodal indices become more and more 'compatible' and eventually at convergence further corrections of the nodal indices (or the free surface shape) are not required.

In the Finite Volume Method, the conservation of mass and other properties is verified on a cell by cell basis and the conservation of mass is used for the computation of the pressure correction. This verification is not carried out in empty cells and cells through which the free surface is passing because the actual location and orientation of the surface is not known. It should be emphasized that global conservation as well as conservation in the full cells *is* satisfied.

Some Numerical Considerations

The free surface simulation adds further coupling to an already complex problem and certain precautions have to be taken in order to aid convergence. As outlined in steps (4) and (5) of the above procedure, the free surface location is determined from the pressures 'PH' and 'PL'. The values of these pressures are under-relaxed

as shown in the following equations

$$PH = \varsigma P(II, J) + (1 - \varsigma)P_o(II, J) \tag{4.82}$$

$$PL = \varsigma P(II - 1, J) + (1 - \varsigma)P_o(II - 1, J) \tag{4.83}$$

where ς is an under-relaxation factor having a value of approximately 0.5 and P_o is the previous iteration value of the pressure P. A similar under-relaxation is used for the velocity u_w in the computation of the kinetic energy of the fluid by eqs (4.77) and (4.81). Therefore

$$u_w = \varsigma u_w + (1 - \varsigma)u_{w_o} \tag{4.84}$$

and

$$u_p = \varsigma u_p + (1 - \varsigma)u_{p_o} \tag{4.85}$$

where u_{w_o} and u_{p_o} are the previous iteration velocities. These under-relaxation procedures are required to reduce the sensitivity of the free surface shape to wide variations in the predicted pressure and velocity fields during the initial iterations.

The under-relaxation factors for the dependant variables also have to be adjusted as the solution progresses through the time steps. This is required because of the changes in the physical size of the domain and in the flow pattern with time.

Other boundary conditions

The boundary conditions applied at the side walls and bottom surface are zero normal and tangential velocities. Therefore, for the north and west boundaries of the domain shown in Figure 4.8

$$V|_{r=r_o} = 0 \qquad U|_{r=r_o} = 0 \tag{4.86}$$

$$V|_{z=0} = 0, \text{ for } r_o \geq r > r_i \qquad U|_{z=0} = 0, \text{ for } r_o \geq r > r_i \tag{4.87}$$

A zero gradient and zero normal flux condition is applied at the south boundary of the domain (Figure 4.8), which models the axis of symmetry.

$$V|_{r=0} = 0 \qquad \frac{\partial U}{\partial r}|_{r=0} = 0 \tag{4.88}$$

The inlet condition is imposed at the west boundary for $r \leq r_i$. The inlet velocity varies with the level of the fluid in the test section. Therefore,

$$U|_{r \leq r_i} = U_{in} \tag{4.89}$$

where U_{in} is specified by eq(4.4). The velocity profile is assumed to be uniform at the inlet.

The properties of pure water at $25°C$ ($\rho = 997 kg/m^3$, $\mu = 8.94 \times 10^{-4}$) are used.

4.4 Discussion

4.4.1 Experimental and computed results

Figures 4.11 to 4.15 illustrate the computed results at different times during the simulation of the filling process. The inlet jet penetrates from the bottom of the test section, flows towards the top and forms a spout at the free surface. The fluid then flows radially outwards and forms a vortex under the free surface. The height of the spout decreases with the increase in the level of the fluid in the test section. This is to be expected as a greater portion of the momentum of the jet is redistributed in the fluid with the increase of the level. The free surface shape is predicted to be fairly flat with the exception of the spout during the initial stages of filling. Figure 4.16 shows the computed and experimental free surface shapes. It can be seen that in general, the proposed method predicts the free surface shape

quite well. The predictions at the initial time steps are less accurate because of the incorrect initial condition of a flat surface profile.

Contour plots of the turbulent kinetic energy and effective viscosity are also shown in Figures 4.11 to 4.15. The turbulent kinetic energy contours have been normalized to U_{in}^2 where U_{in} is the inlet velocity. The highest values of the turbulent kinetic energy were in the regions where the jet spread into the fluid and in the vortex. The effective viscosity contours have been normalized to the laminar viscosity. The effective viscosity is high in the regions of steep velocity gradients and is between two to three orders of magnitude greater than the laminar viscosity.

Figures 4.17 to 4.24 show the computed velocity distributions and the photographs obtained during the filling process. Computations were done using both the free slip condition and the free surface treatment described in this chapter. The plotting scales of the computed velocities are the same as those on the experimental photographs, so that an arrow and a streakline of the same length represent the same velocity magnitude. The following observations can be made from these figures:

(a) In general, for both the free surface and the free slip conditions, the computed location of the vortex appears to be closer to the surface than observed in the experiments. Figure 4.25 shows the computed and measured radial locations of the vortex. It may be seen that the computations with the free slip condition incorrectly predict the vortex to be further from the axis than observed experimentally. The radial position of the vortex is predicted very well when the free surface condition is used. The inlet jet impinges on the pseudo–frictionless wall when the free slip condition is used, which causes the jet to be thicker and forces the fluid radially outwards. This results in an overestimation of the radial velocities and causes the vortex to be radially further from the axis than observed experimentally or computed with the free surface condition. Figure 4.25 shows that the vortex radial location is predicted very accurately when the free surface condition is used.

(b) The angle of the jet appears to be too large if the free slip condition is used, because the fluid is more constrained and higher pressures occur at the surface. In the case of the free surface condition, however, a zero pressure is maintained at the boundary, which is a less restrictive condition. The jet angle appears to be much closer to the experimental observations, as shown in Figures 4.17, 4.22, 4.23 and 4.24. The jet angle cannot be determined because of the recirculatory flow pattern, however a quantitative estimate *can* be obtained from the radial position of the vortex. Figure 4.25 shows that the radial position of the vortex (and therefore the jet angle) is consistently well predicted when the free surface condition is used. The larger jet angle causes the vortex to be at a greater radial distance when the free slip condition is used. The velocities which are predicted in the region of the spout also appear to be quite good, as evident in Figure 4.18.

(c) The higher radial velocities near the surface with the free slip condition also result in higher axial velocities near the walls and radial velocities at the bottom. These higher velocities are apparent in Figures 4.17, 4.23 and 4.24, and would produce erroneous results in heat transfer computations. These higher velocities are a major source of discrepancy (reported in the literature [7,60,61,120,96]) between computed and experimental results.

(d) In general it appears that the computed velocities are somewhat lower in magnitude as compared with the experimental observations. A reason for this may be the effects of false diffusion of the momentum, as most of the flow in the vortex is inclined to the mesh. This has the same effect as an artificial viscosity which redistributes the momentum. The false diffusion can somewhat suppress the overestimated velocities obtained with the free slip condition, with the result that in some cases the free slip condition appears to produce better results in some regions of the domain due to compensation of errors.

4.4.2 Other applications

The free surface treatment developed in this chapter has already proven to be useful in other applications.

A technique to impose pressure boundary conditions when using the Finite Volume Method was developed for the free surface treatment. This technique was transferred and used [109,117] in modelling external flows with a zero pressure gradient. The results appear to be more accurate than those obtained using the usual free slip assumption.

The free surface treatment developed in this study is presently being applied by Sahajwalla [96] to model the flow in a water bath due to an upwardly injected air jet. The work is relevant to the study of gas stirring in steel–making ladles. Figure 4.26 shows typical velocity distributions computed using the free slip condition and the free surface treatment. It can be seen that the free surface treatment significantly affects the velocity distribution both in the bath and in the region of the spout. The flow in the region of the spout has great significance in steelmaking, as it is a region of strong metal-slag-air mixing which accelerates steel-slag reactions and oxygen absorption by the bath [96]. It can be clearly seen that the free slip condition is inadequate to study the flow in the region of the spout. The velocity distribution in the bath is also different because of the free surface, and this can have a significant effect on the homogenization times.

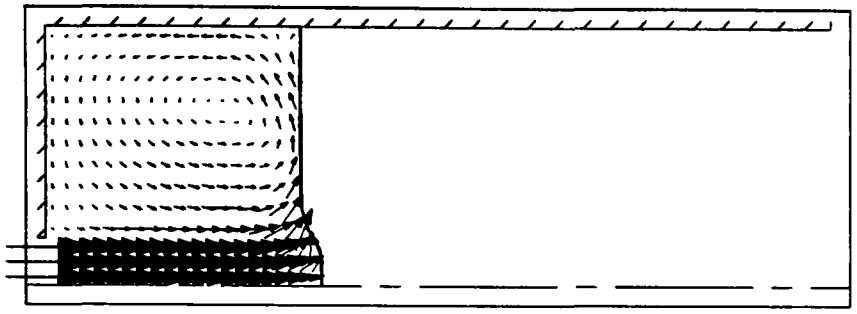

VELOCITY

0.788m/s per inch

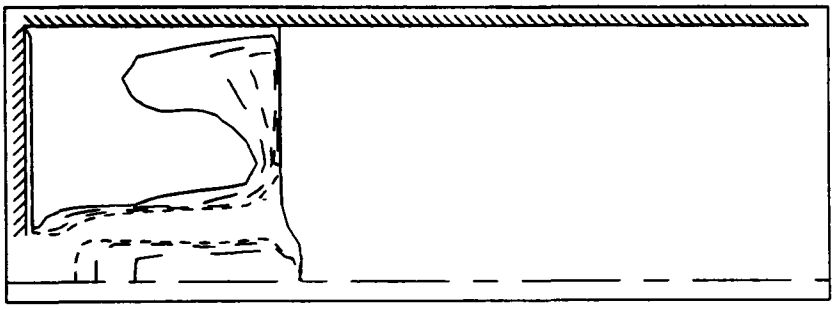

TURB. KIN. ENERGY

KEY TO CONTOUR VALUES

0.00819
0.0163
0.0245
0.0327

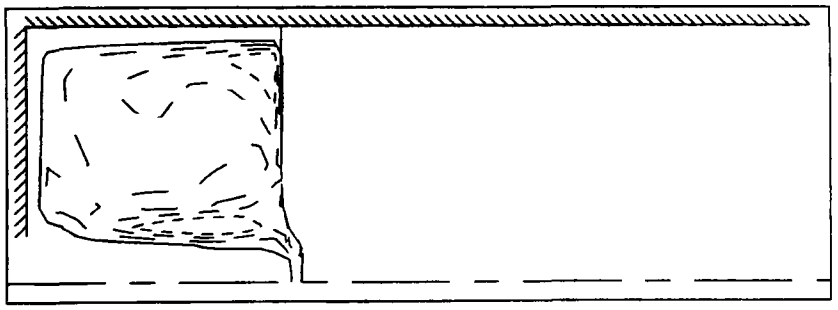

EFF./LAM. VISCOSITY

KEY TO CONTOUR VALUES

11.94
22.89
33.84
44.79

Figure 4.11 Velocity, turbulent energy and effective viscosity at time = 4 s, level = 0.592 m

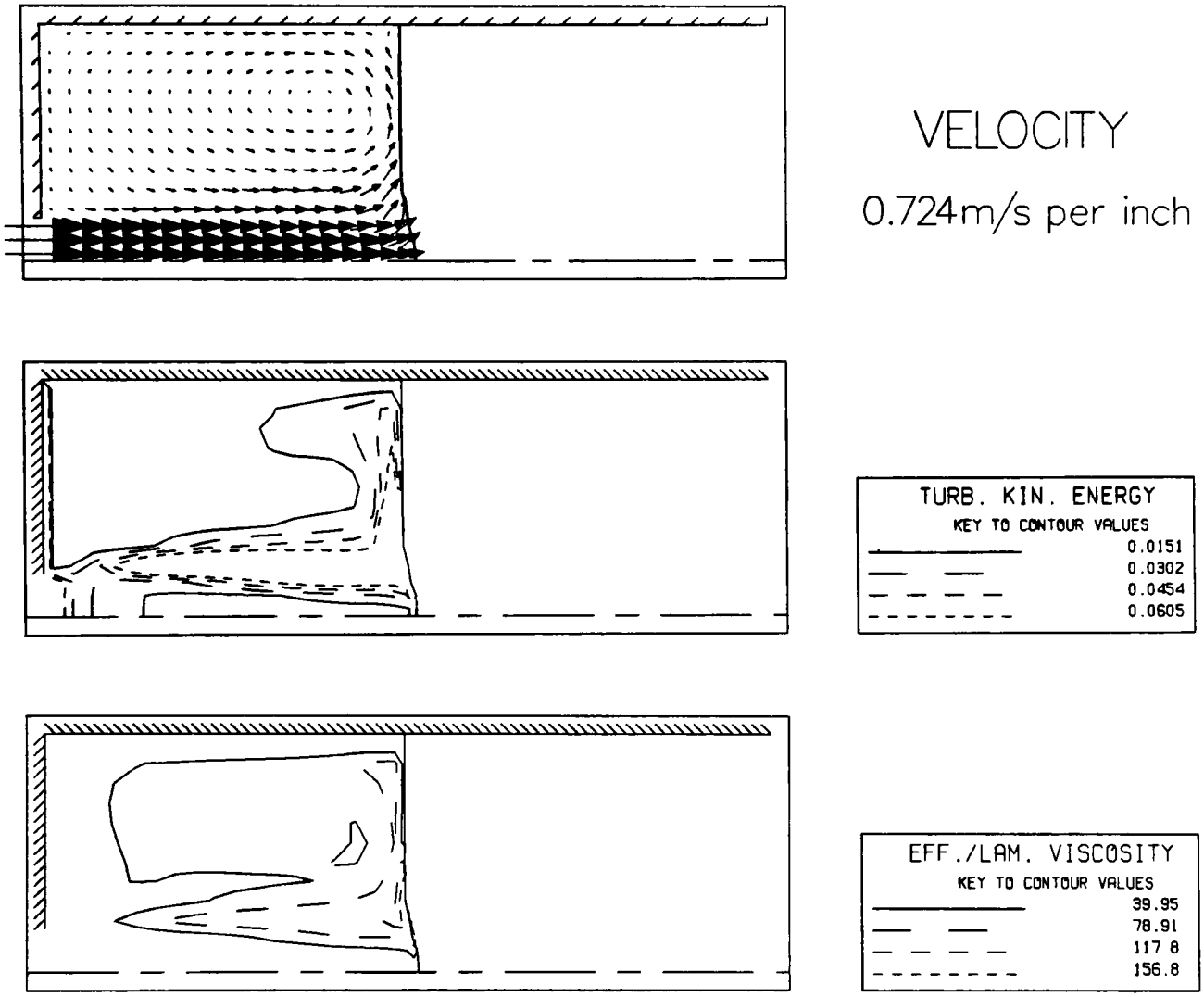

Figure 4.12 Velocity, turbulent energy and effective viscosity at time = 7.5 s, level = 0.090 m

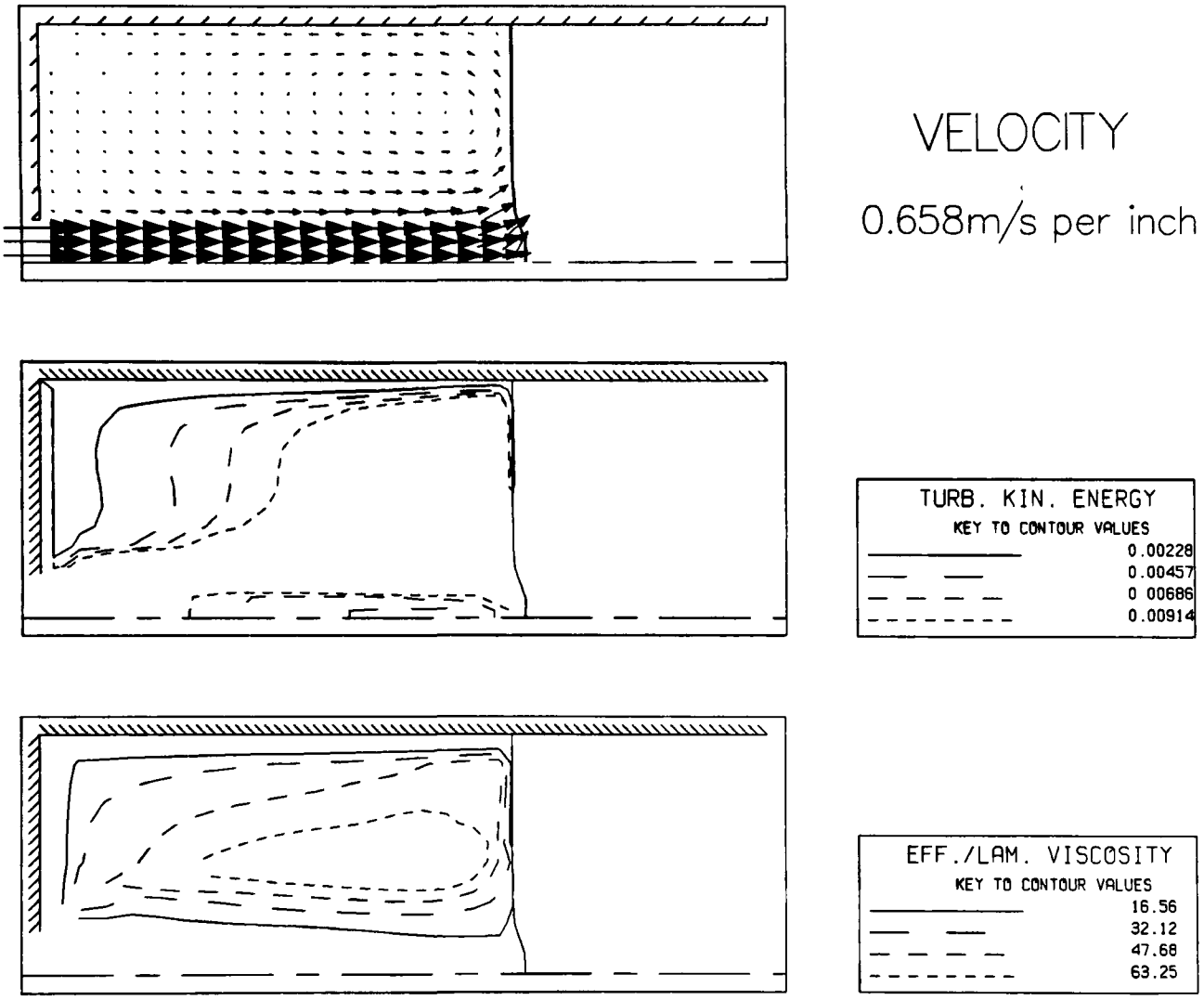

Figure 4.13 Velocity, turbulent energy and effective viscosity at time = 11 s, level = 0.119 m

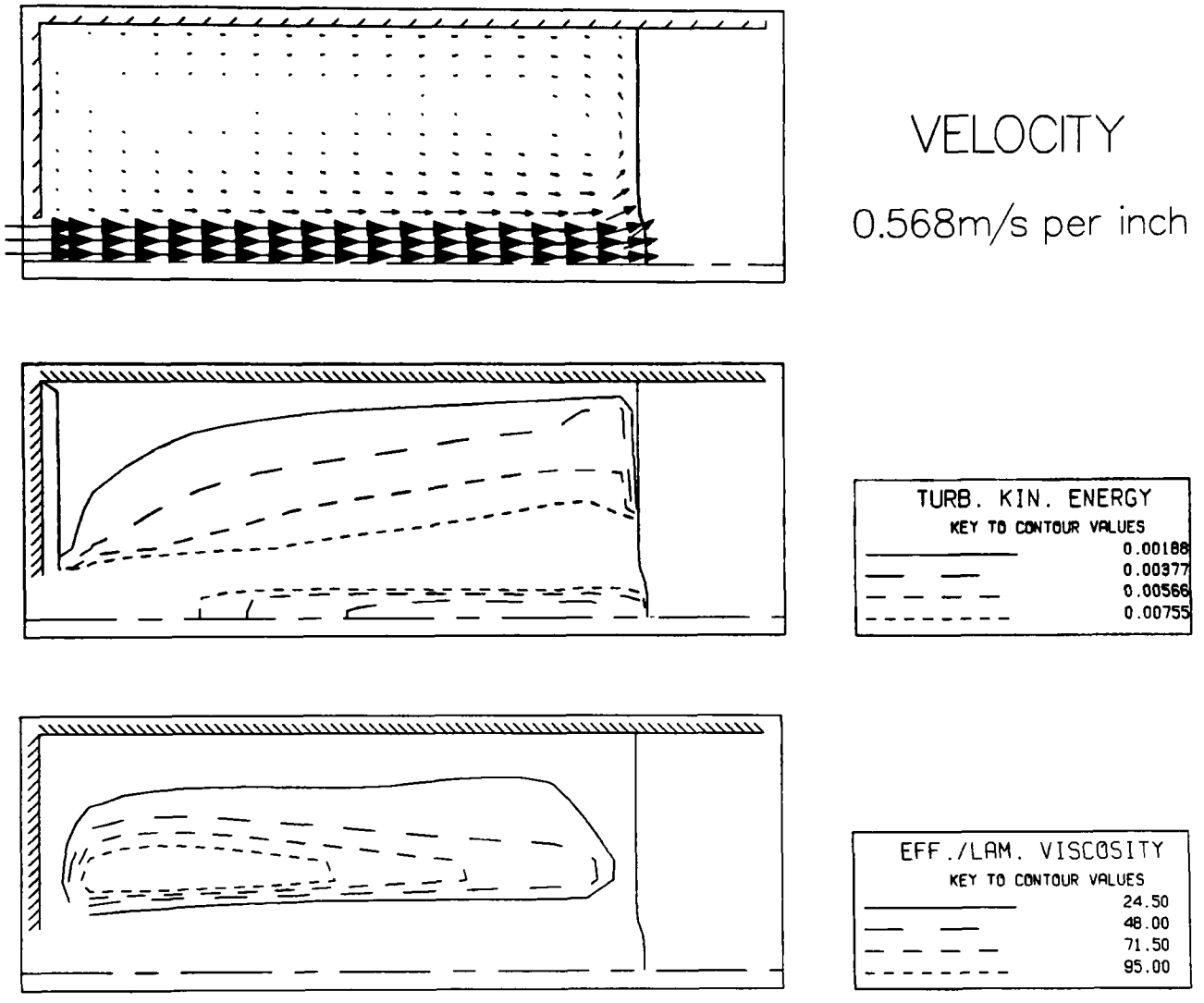

Figure 4.14 Velocity, turbulent energy and effective viscosity at time = 15.5 s, level = 0.151 m

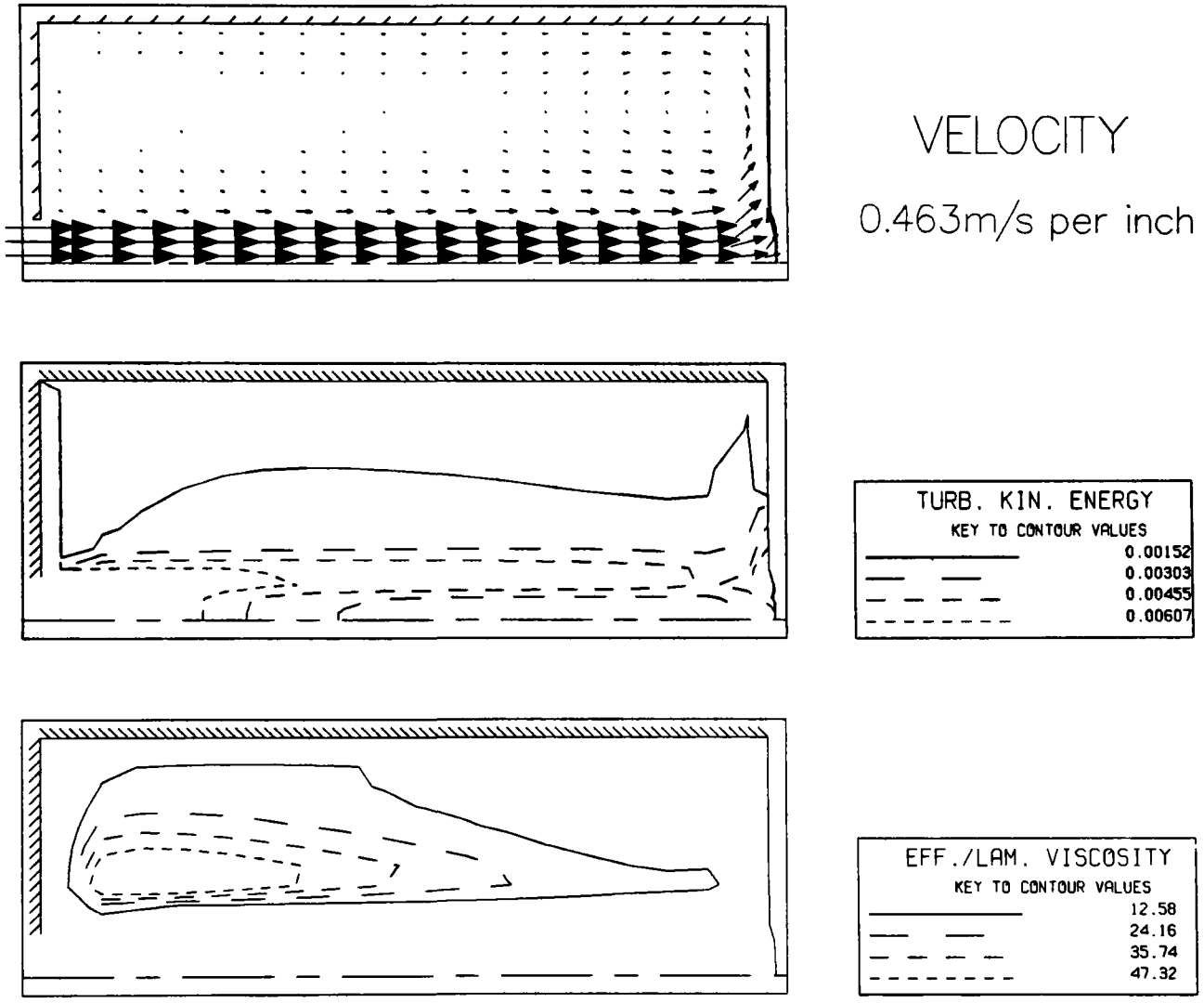

Figure 4.15 Velocity, turbulent energy and effective viscosity at time = 21 s, level = 0.183 m

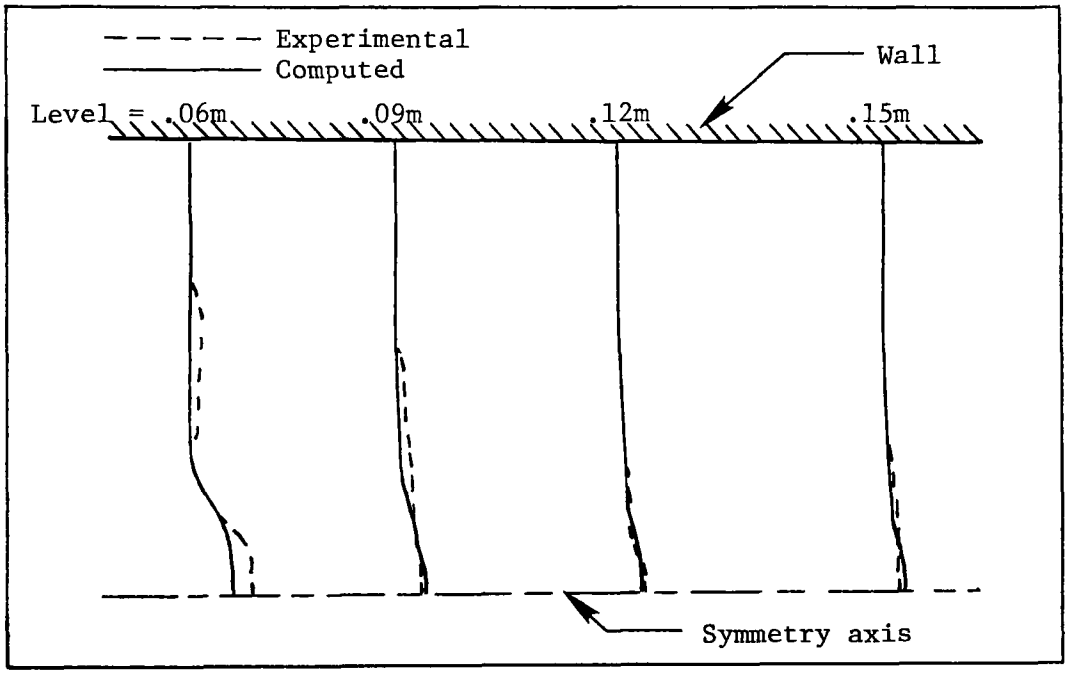

Figure 4.16 Experimental and computed free surface profiles

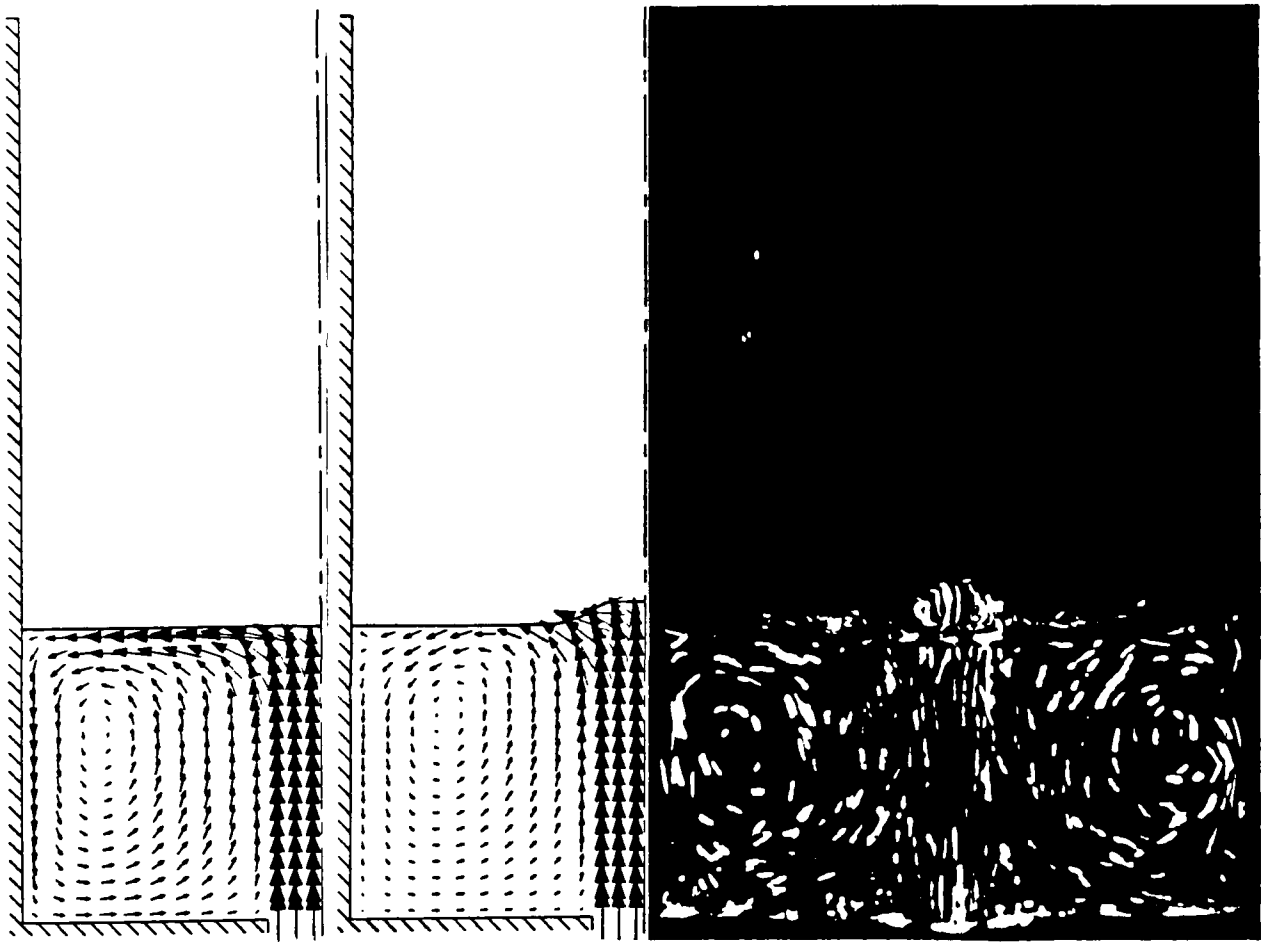

Figure 4.17 Experimental streakline photographs and computed velocity fields at time = 4 s, level = 0.059 m, scale = 0.15 $m/s\,cm$

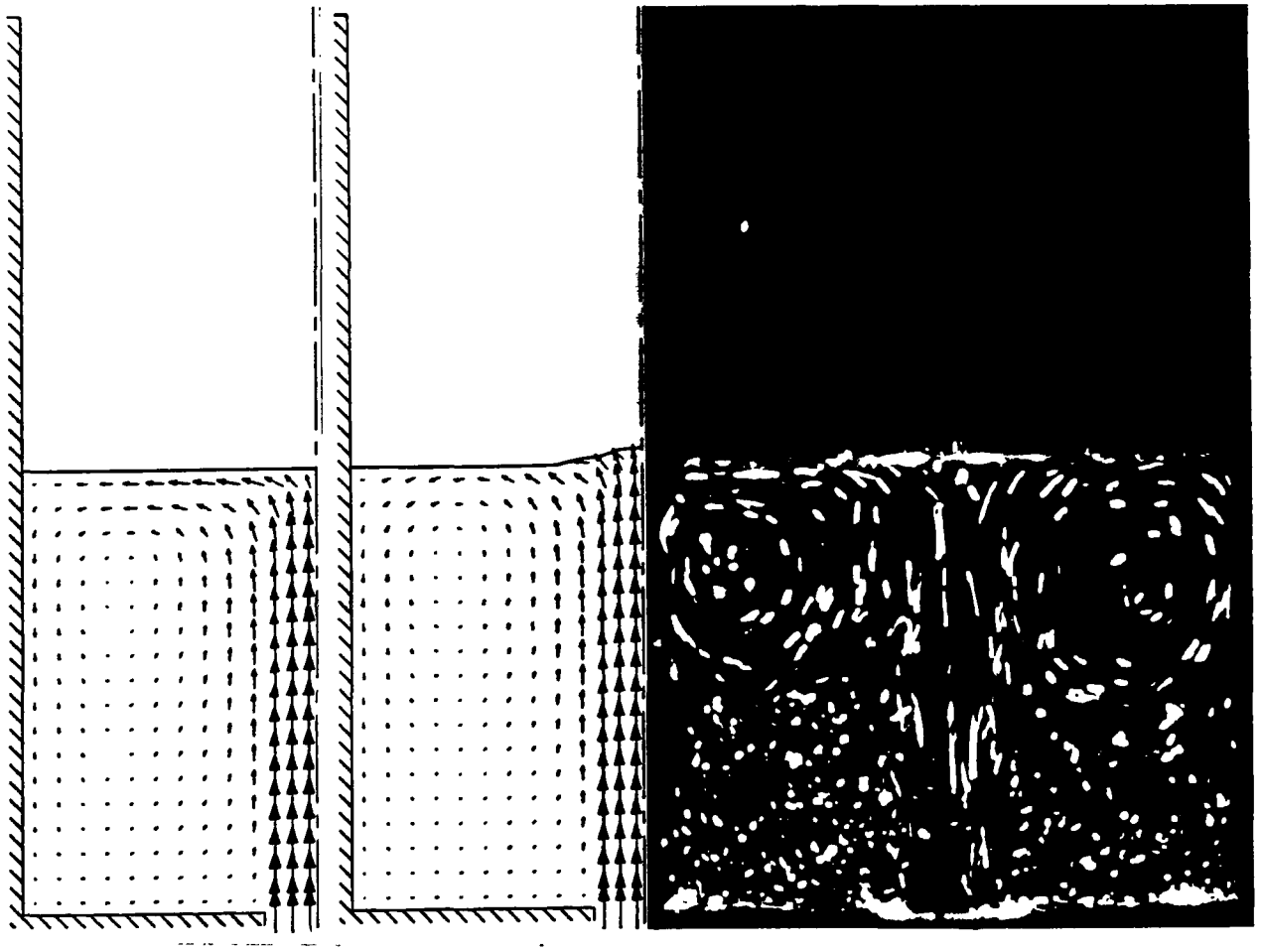

Figure 4.18 Experimental streakline photographs and computed velocity fields at time = 7.5 s, level = 0.090 m, scale = 0.3 $m/s\,cm$

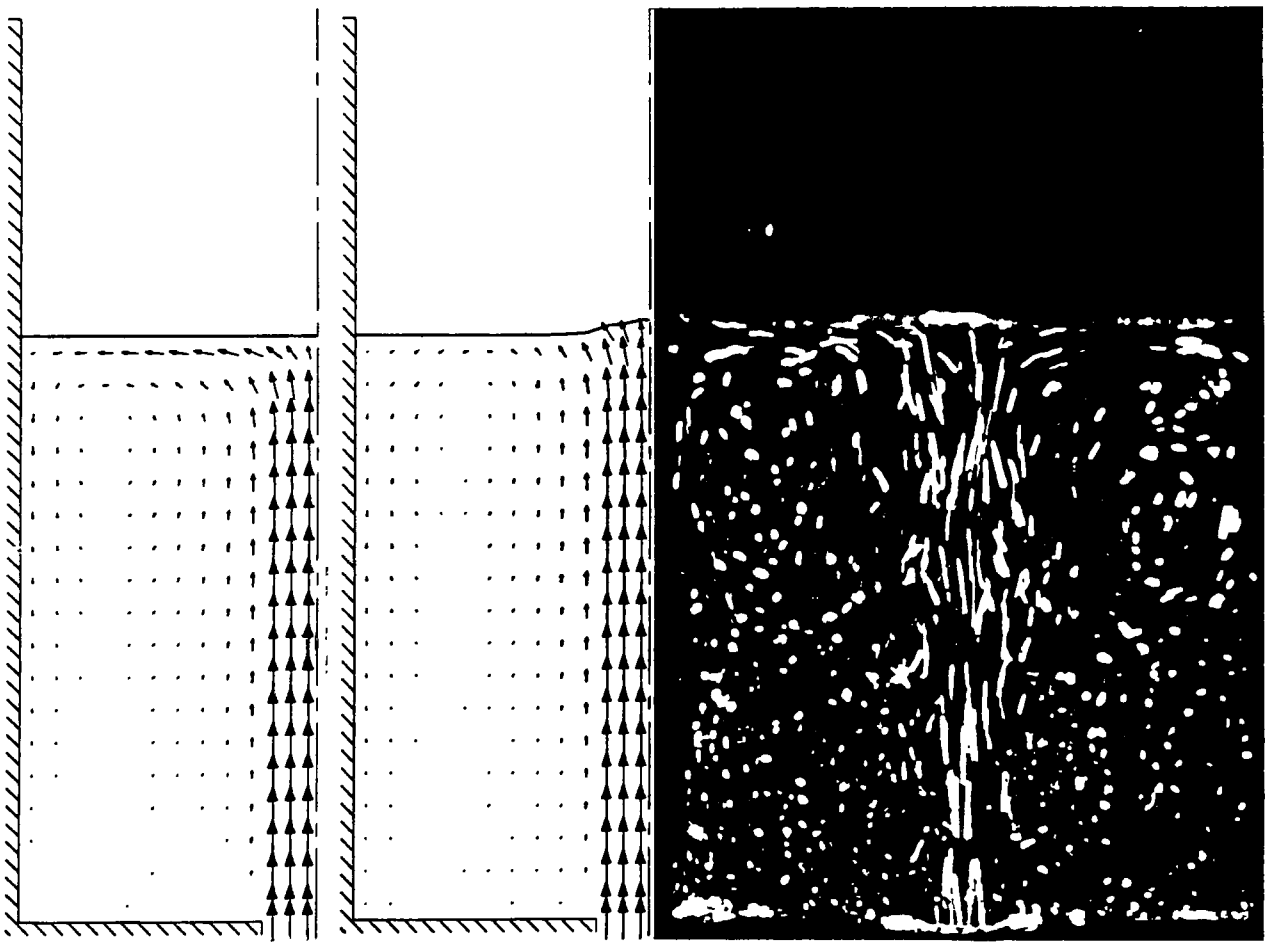

Figure 4.19 Experimental streakline photographs and computed velocity fields at time = 11 s, level = 0.119 m, scale = 0.3 $m/s\,cm$

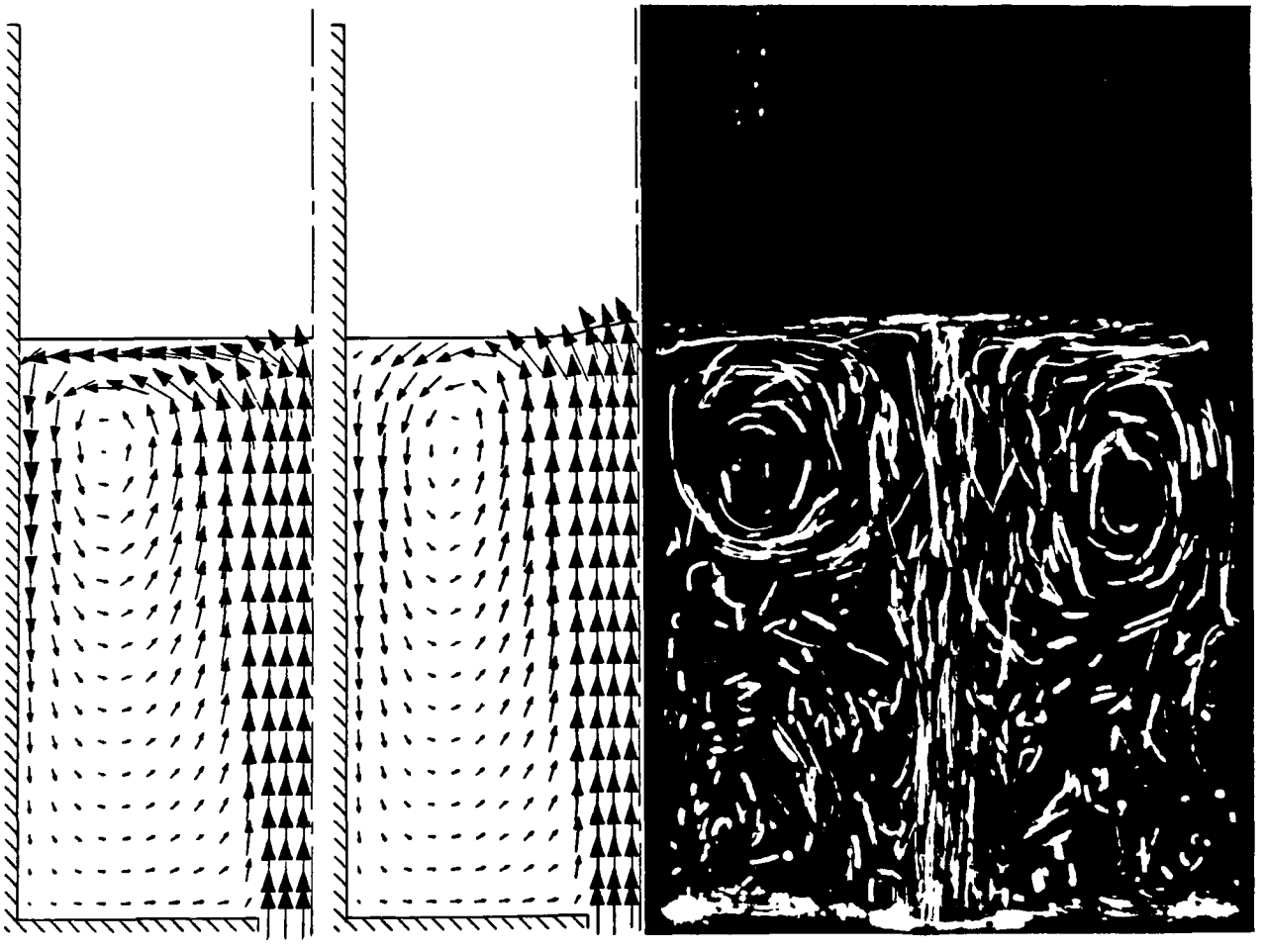

Figure 4.20 Experimental streakline photographs and computed velocity fields at time = 11 s, level = 0.119 m, scale = 0.04 $m/s\,cm$

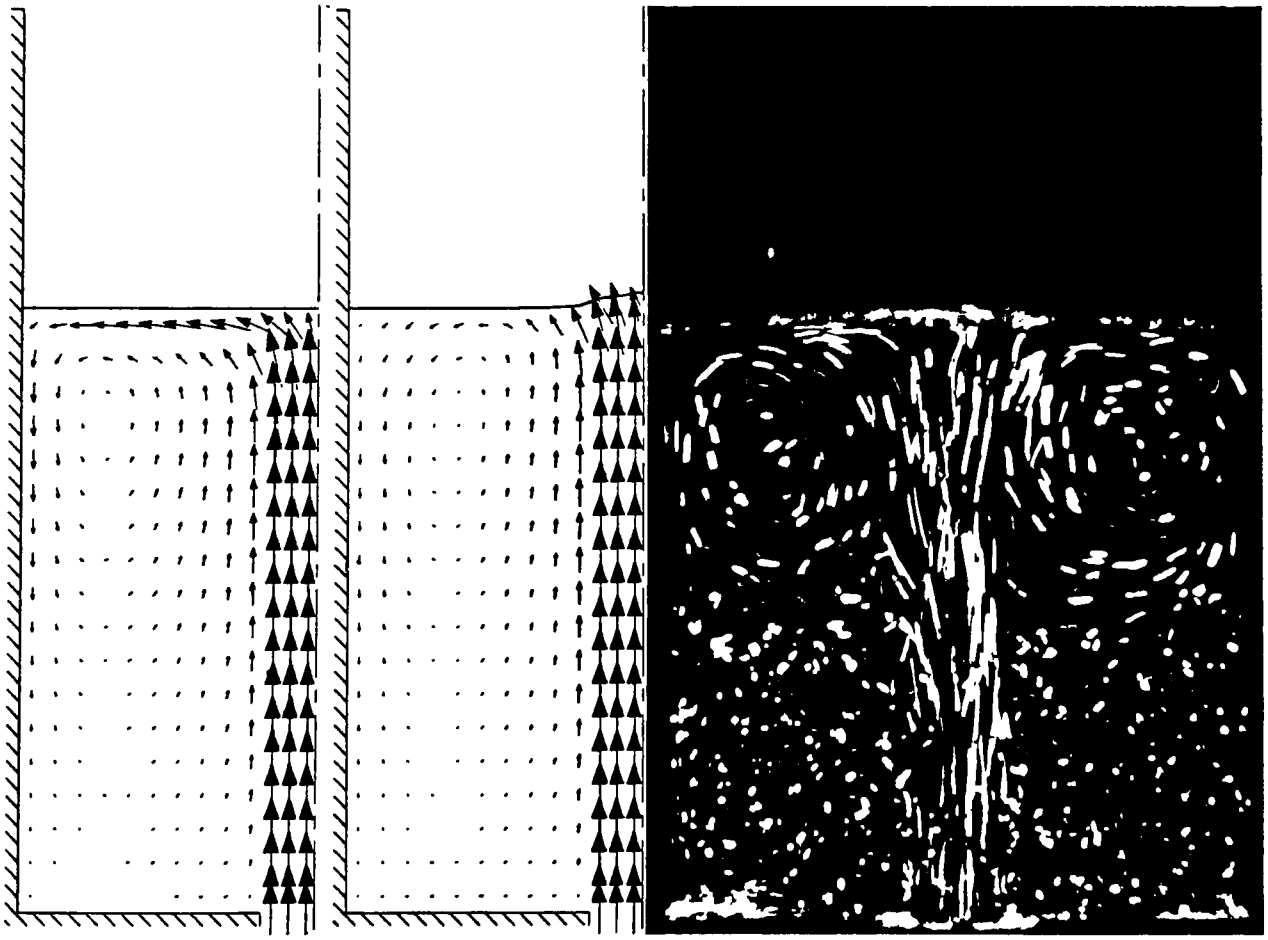

Figure 4.21 Experimental streakline photographs and computed velocity fields at time = 11.5 s, level = 0.122 m, scale = 0.15 $m/s\,cm$

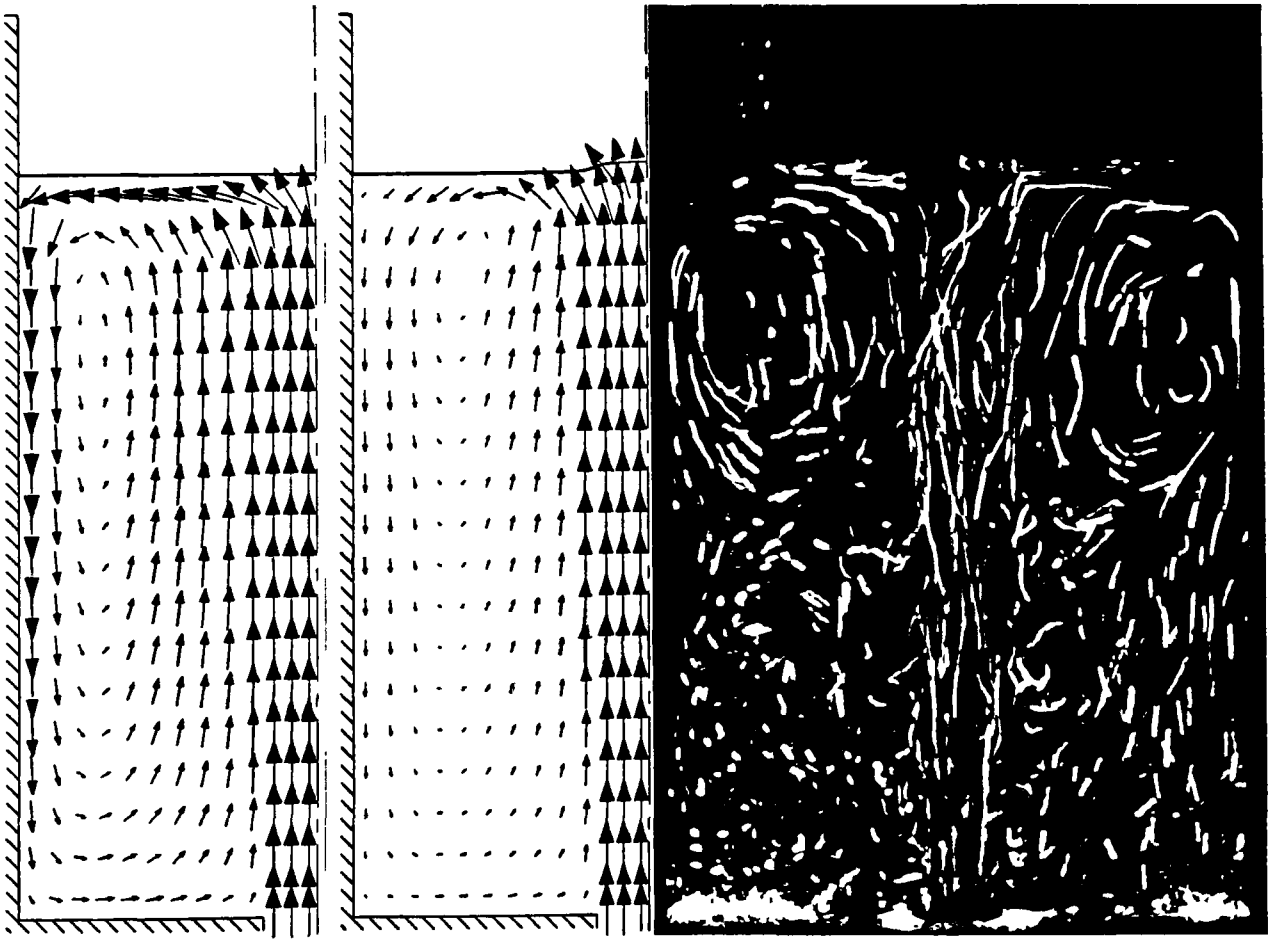

Figure 4.22 Experimental streakline photographs and computed velocity fields at time = 15.5 s, level = 0.151 m, scale = 0.04 $m/s\,cm$

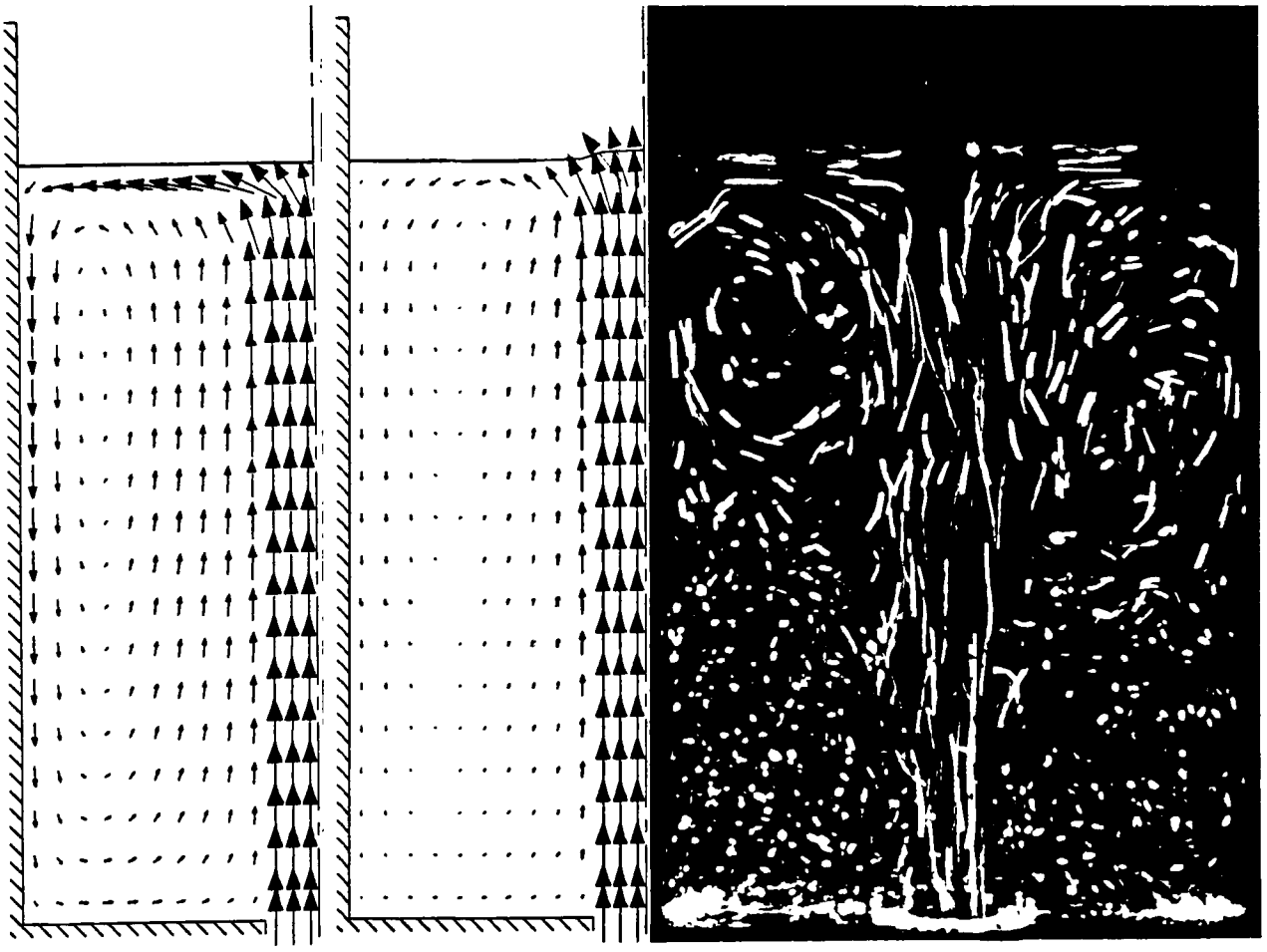

Figure 4.23 Experimental streakline photographs and computed velocity fields at time = 16 s, level = 0.154 m, scale = 0.08 $m/s\,cm$

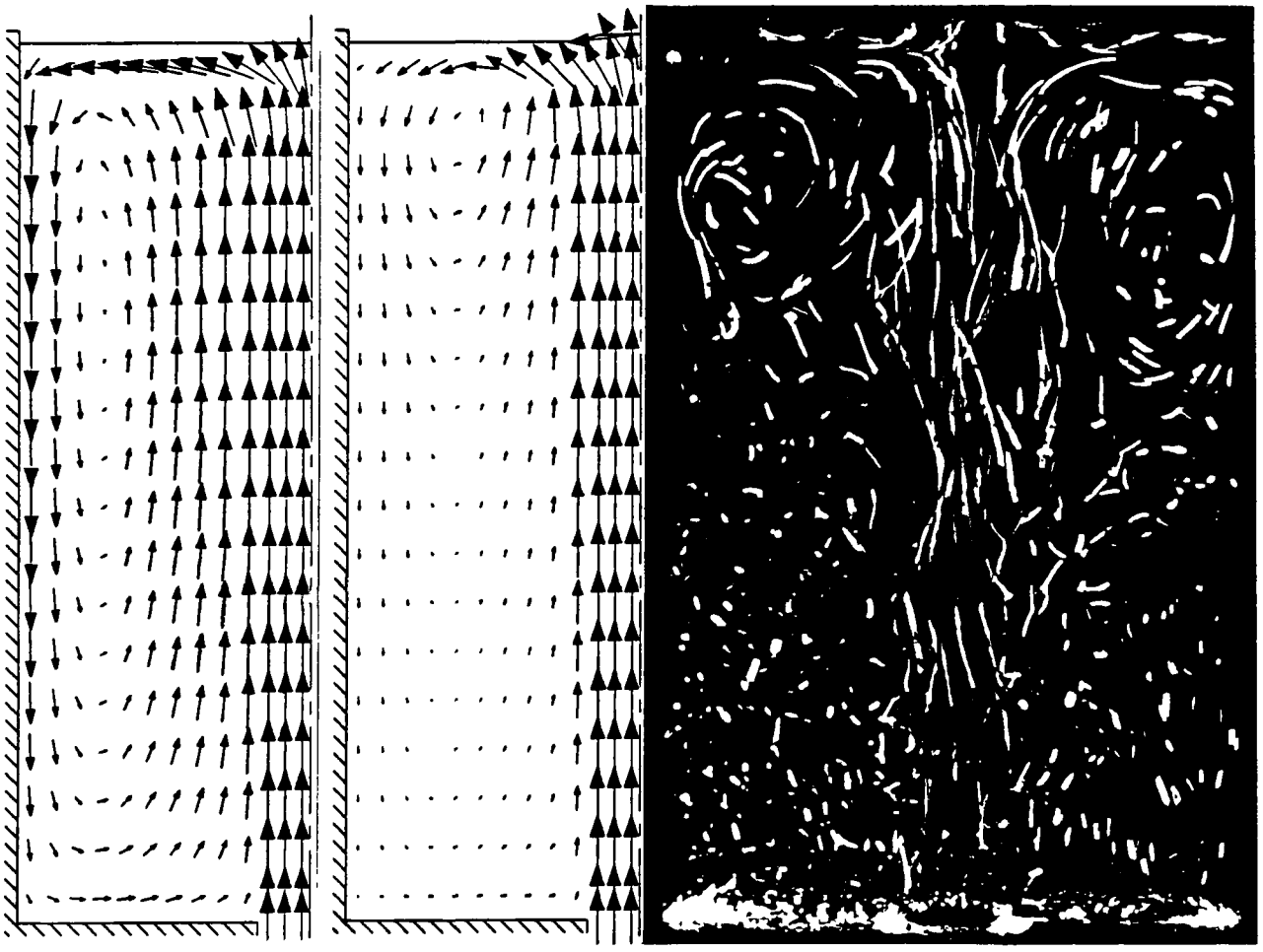

Figure 4.24 Experimental streakline photographs and computed velocity fields at time = 20.5 s, level = 0.180 m, scale = 0.04 $m/s\,cm$

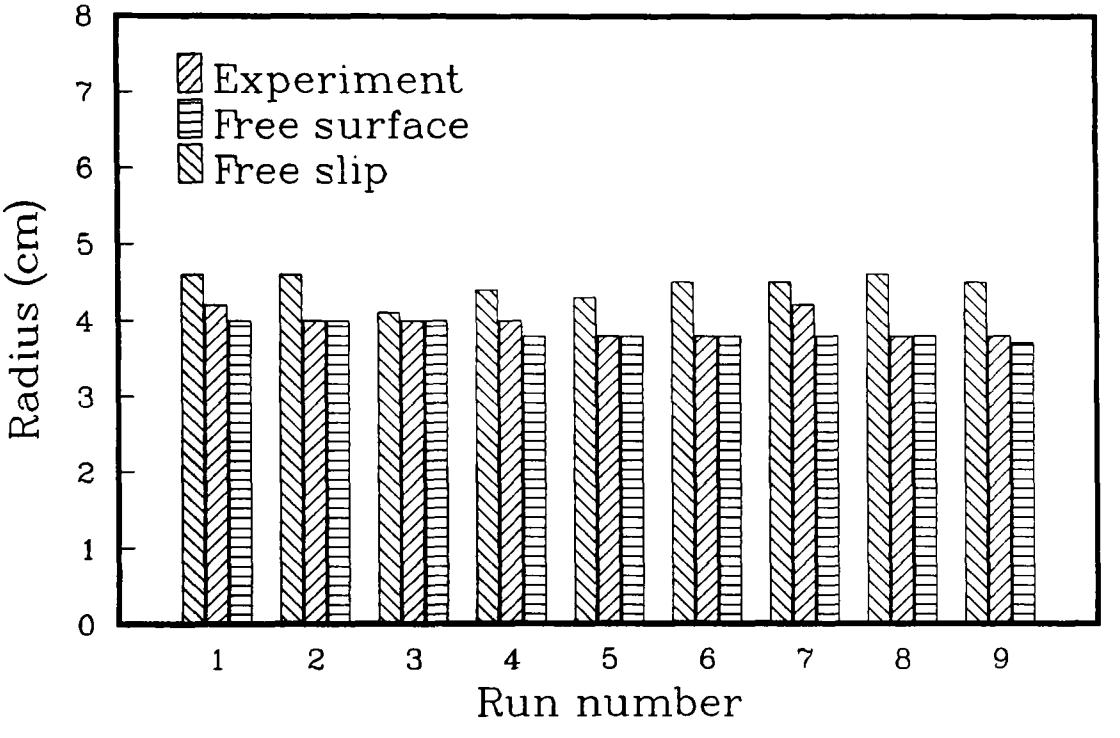

Figure 4.25 Computed and measured radial position of the vortex

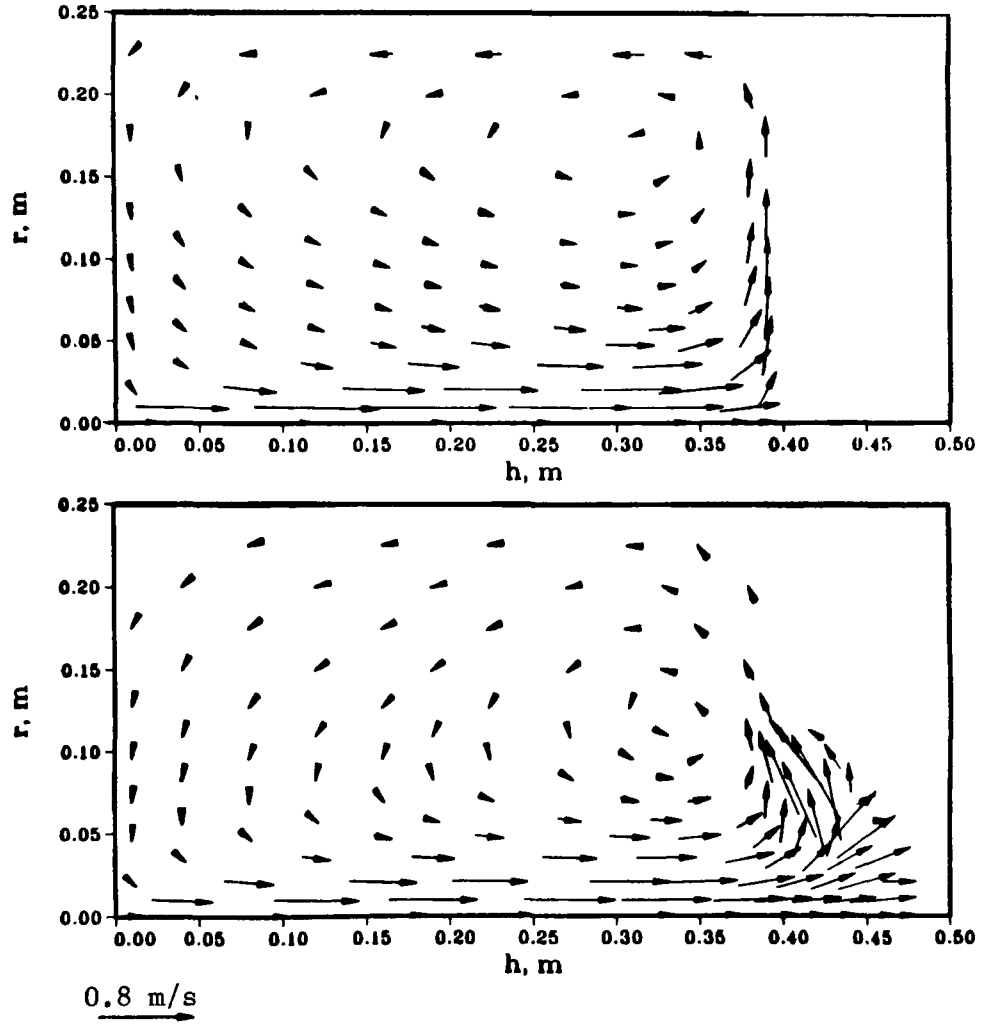

Figure 4.26 Velocity distribution in a water bath stirred by an air jet

Chapter 5

MODELLING A CASTING CYCLE

5.1 Introduction

Simulation of the liquid metal convection during the filling of molds and solidification has received less attention than conduction because of the complexity of solving the required conservation equations in a domain bounded by a free surface and a moving solid–liquid interface. This chapter describes computational and mathematical work carried out to investigate liquid metal convection and heat transfer during the casting of a cylindrical cast iron ingot. Some sections of this work have been published [1,97,98]. The following contributions are reported:

1. Simulation of liquid metal flow and heat transfer during pouring.
2. Simulation of liquid metal solidification in the presence of natural convection.
3. Comparison of the computed results against experimental data.

4. Mathematical formulation of the flow through solid liquid mushy zones.

5. Mathematical formulation for binary latent heat release using the source based method.

5.2 Experimental work

The test problem considered[1] is the solidification of a cylindrical grey iron casting of length 0.154 m and diameter 0.1072 m. A schematic diagram of the mold is shown in Figure 5.1. The mold consists of a 0.0668 m thick cast iron cylinder resting on a sand base. A gating system in the base allows the liquid metal to enter the mold cavity axially at the center. A 0.054 m cast iron cover plate shielded by a 0.0127 m layer of sand forms the upper part of the mold. The mold cavity surfaces are sprayed with an approximately 0.4 *mil* thick layer of a commercial ceramic mold-coating material, followed by a graphite layer and acetylene flame sooting before each pour. A high carbon equivalent cast iron (see Table 2.1) is used to minimize shrinkage and the associated uncertainty in the heat transfer at the mold casting interface. Pour time is approximately 7 seconds. Temperatures are measured with chromel-alumel thermocouples with 40 *mil* (1.02 *mm*) O.D. stainless steel sheaths, inserted in close–fitting holes at the positions shown in Figure 5.1. The thermocouples in the casting are shielded by thin walled silica tubes of 3.2 *mm* O.D. The response time of the thermocouples is approximately 3 seconds [24]. Temperatures are recorded with a Sciemetic Labmate Model 7000 data logger with an accuracy of approximately $\pm 2\,^{\circ}C$. The alloy is melted in an induction furnace, tapped into a ladle and poured into the mold. Sectioning of the castings after solidification indicates that the thermocouples do not move during the experimental procedure [24].

[1]The experimental work reported in this section was done in collaboration with the personnel of CANMET/PMRL at the Department of Energy, Mines and Resources, Government of Canada.

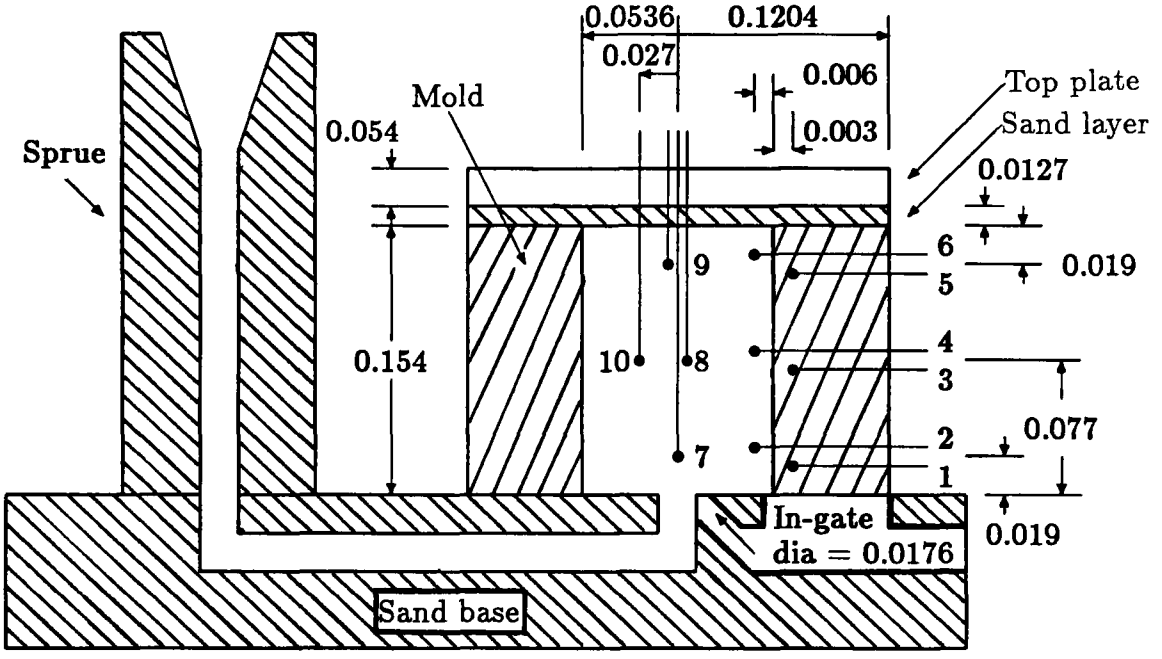

Figure 5.1 Schematic of the cylindrical mold showing thermocouple positions and gating arrangement (figure not to scale, all dimensions in m)

Table 5.1 Experimental parameters

Pouring time	7.0 s
Ambient temperature	25 ^oC
Pouring temperature	1275 ^oC
Mold temperature, (T_{mold})	110 ^oC

5.3 Mathematical modelling

This section presents mathematical models to simulate different aspects of the casting cycle described previously. The Finite Volume Method (see Chapter 3) is used and the cast iron properties are described in Table 2.1. Temperature dependence of the liquid metal properties is neglected because pouring takes place only 25 ^oC above the liquidus temperature. The properties of sand used are [105] $\rho = 1600\,kg/m^3$, $c = 532\,J/kg^oC$, $k = 0.523\,W/m^oC$. The experimental parameters are specified in Table 5.1.

The casting process is divided into the filling and solidification stages as described in Chapter 1. The liquid metal flow during the filling stage is simulated using the Eulerian–Lagrangian technique described in the previous chapter. Solidification is modelled in the presence of natural convection. Heat transfer in the mold is simulated using a separate, fixed grid. Two different mesh (see Figure 5.2) are used to verify grid independence of the results. The computation of the mold and casting are coupled at the mold casting interface using a heat flux condition described subsequently.

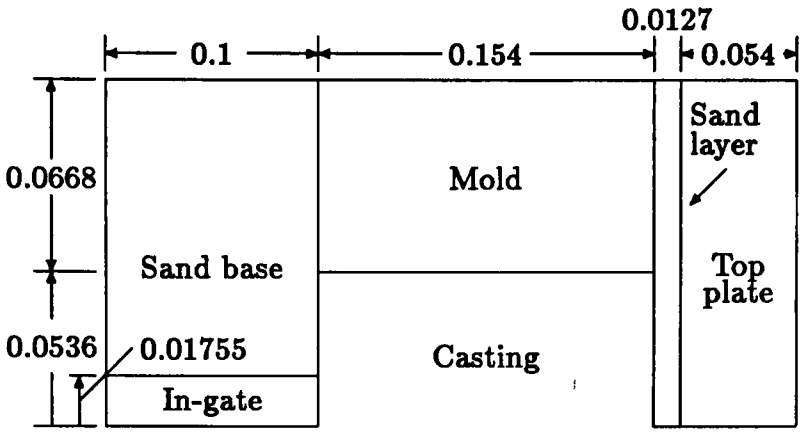

(a) Computational domain

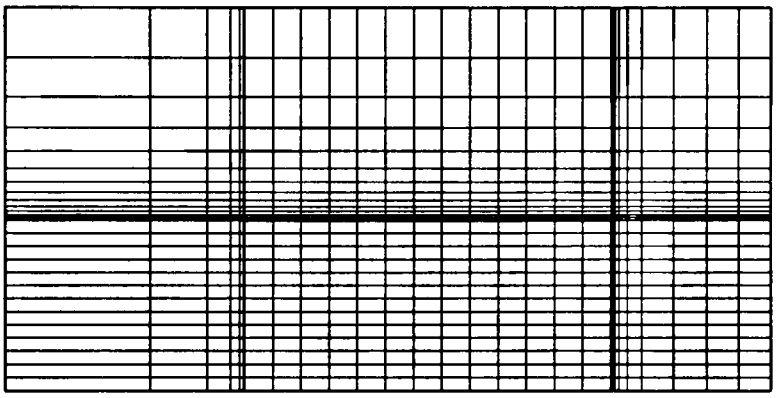

(b) Coarse mesh 30 × 28

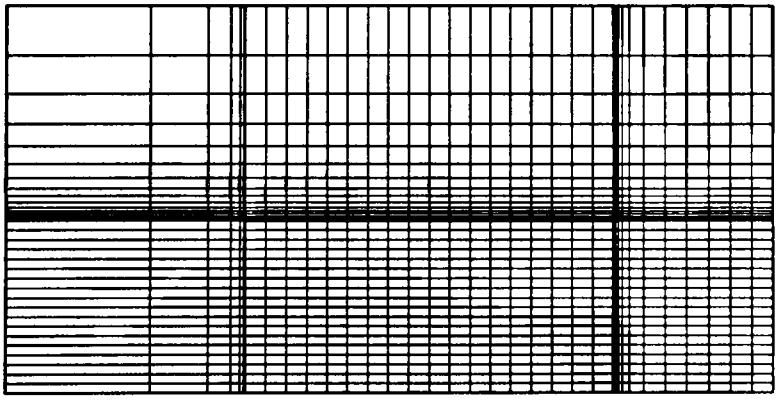

(c) Fine mesh 40 × 38

Figure 5.2 Computational domain and mesh used; figure (a) not to scale; all dimensions in m; note very fine grid near the mold casting interface

5.3.1 Modelling filling of the mold

The flow enters the mold from an in-gate located centrally in the sand base, in the form of a turbulent jet, as the Reynolds number based on the gate diameter and average fluid velocity is 5000 [9,82,106,131]. The effects of turbulence are simulated by the $K - \epsilon$ model (see Chapter 3).

The level of the fluid rises continuously during filling. The hybrid Eulerian–Lagrangian technique and the free surface treatment (developed in Chapter 4) are used to conform the mesh to the liquid metal. The mesh used are shown in Figure 5.2. Details of the mathematical formulation are presented in Chapter 4. The energy conservation equation is also solved, in addition to the equations for the conservation of mass, momentum, turbulent kinetic energy and energy dissipation. The formulation for the latent heat treatment and the boundary conditions for the energy equation are discussed subsequently. The following assumptions are made in the mathematical simulation of the filling process:

1. *The filling rate is uniform.* The liquid metal is poured into the sprue by an operator as uniformly as possible. The most 'reasonable' assumption which can be made is that of uniform filling.

2. *The mold cavity initially (at time t=0) contains a stagnant pool of liquid metal of depth 0.0154 m (10% of the casting height).* This assumption is required because the grid in the casting region is initially 'compressed' such that its axial dimension is 10% of the casting height and a zero initial velocity field is used. The initial predictions of the velocity field are therefore not expected to be accurate. The flow pattern is strongly influenced by the inlet jet however, and the effects of the incorrect initial condition are not expected to be significant after a few time steps. It should be noted that the same assumption is made during the simulation of the filling of the cylindrical test section in Chapter 4, and later agreement with experimental data shows this

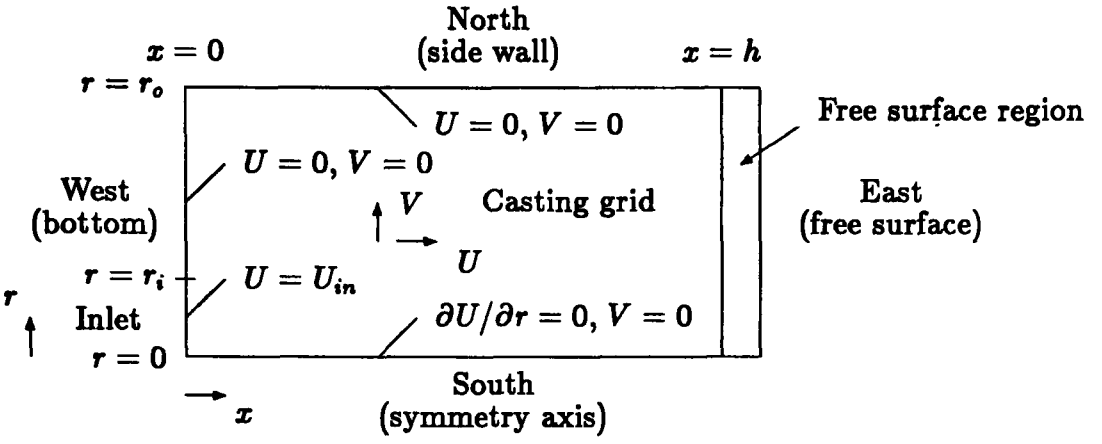

Figure 5.3 Boundary conditions for the casting region

assumption to be valid.

Boundary conditions for the casting region

West boundary

The west boundary models the bottom of the mold cavity. Wall conditions are applied for $r > r_i$, and zero velocities are imposed. Therefore (see Figure 5.3)

$$V|_{x=0} = 0, \text{ for } r_o \geq r > r_i \qquad U|_{x=0} = 0, \text{ for } r_o \geq r > r_i \tag{5.1}$$

The inlet condition is imposed for $r \leq r_i$. The inlet velocity is calculated on the basis of a uniform filling rate assumption

$$U_{in}|_{r \leq r_i} = \frac{Vol}{t_{fill} \pi r_i^2} \tag{5.2}$$

where Vol is the volume of the mold cavity and t_{fill} is the filling time. The velocity profile is assumed to be uniform at the inlet.

North boundary

The North boundary (Figure 5.3) models the side wall of the mold cavity. Wall conditions (zero velocities) are applied

$$V|_{r=r_o} = 0, \text{ for } 0 \leq x \leq h \qquad U|_{r=r_o} = 0, \text{ for } 0 \leq x \leq h \tag{5.3}$$

South boundary

A zero gradient and zero normal flux condition is applied at the South boundary of the domain (Figure 5.3), which models the axis of symmetry.

$$V|_{r=0} = 0, \text{ for } 0 \leq x \leq h \qquad \frac{\partial U}{\partial r}|_{r=0} = 0, \text{ for } 0 \leq x \leq h \tag{5.4}$$

East boundary

The free surface treatment is applied to the East boundary of the domain during the filling period. Once filling is complete, the wall condition is used on the East boundary.

5.3.2 Modelling heat transfer in the mold

Heat transfer in the mold and sand base is by conduction. The governing equation for heat conduction through an isotropic material in an axi-symmetric two dimensional cylindrical coordinate system is written as

$$\frac{\partial \rho h}{\partial t} = \frac{1}{r}\left[\frac{\partial}{\partial x}\left(r\Gamma_{eff}\frac{\partial h}{\partial x}\right) + \frac{\partial}{\partial r}\left(r\Gamma_{eff}\frac{\partial h}{\partial r}\right)\right] \tag{5.5}$$

The Finite Volume Method (Chapter 3) is used as the solution technique. The solution is obtained on the fixed mesh shown in Figure 5.2. The boundary conditions (see Figure 5.4) are as follows:

West boundary

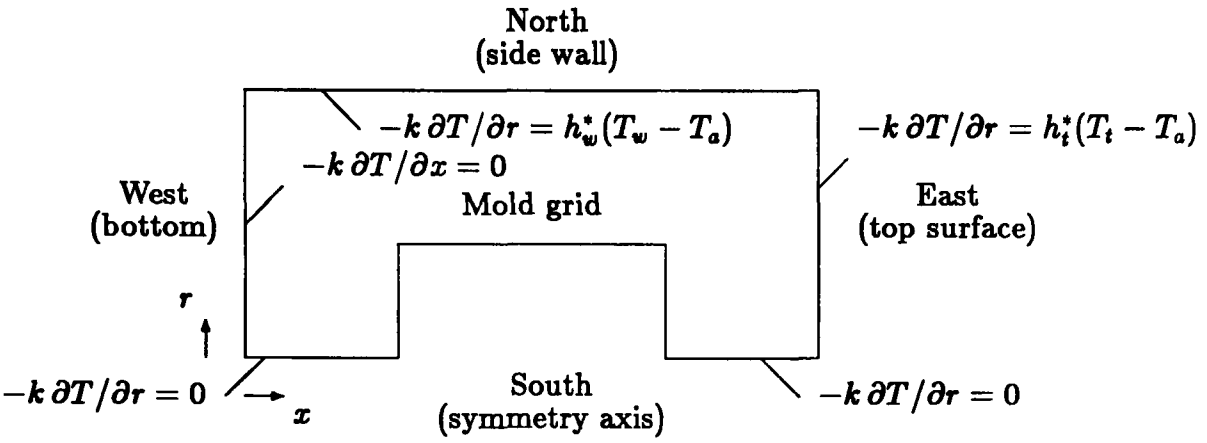

Figure 5.4 Boundary conditions for the mold region

An adiabatic condition is used on the West boundary, which represents the bottom of the sand base. The thermal diffusivity of sand is approximately an order of magnitude less than that of cast iron [105], therefore the heat loss from the bottom of the sand base to the floor is assumed to be negligible. The boundary condition at the base is expressed as

$$-k\frac{\partial T}{\partial x}|_{bottom} = 0 \tag{5.6}$$

South boundary

The South boundary represents the axis of symmetry. The zero flux (adiabatic) condition is applied

$$-k\frac{\partial T}{\partial r}|_{axis} = 0 \tag{5.7}$$

East and North boundaries

The East and North boundaries represent the top and the side walls of the mold, respectively. Heat is lost from these boundaries by free convection and radiation. The boundary conditions are written as follows.

$$-k\frac{\partial T}{\partial x}|_{top} = h_t^*(T_t - T_a) \tag{5.8}$$

$$-k\frac{\partial T}{\partial r}|_{wall} = h_w^*(T_w - T_a) \tag{5.9}$$

where h_t^* and h_w^* are the equivalent heat transfer coefficients for the natural convection [47] and radiation losses from the top and side walls of the mold.

5.3.3 Modelling heat transfer in the casting

Heat transfer in the casting is by conduction and convection in the presence of solidification and latent heat release. In the present work the numerical modelling is done using the Finite Volume Method (Chapter 3).

Computation of convection after filling

The natural convection is computed using the Boussinesq approximation [51]. The additional body force (B) due to thermal gradients is calculated as follows

$$B = (1-\varsigma)B_o + \varsigma\rho g\beta\, Vol\,(T - T_{ref}) \tag{5.10}$$

where B_o is the previous iteration value of B and ς is an under-relaxation factor (approximately 0.7). The upper limit of the Grashof number [47]

$$Gr = \frac{g\beta(T_{pour} - T_s)r_o^3}{\nu^2} \tag{5.11}$$

based on the casting radius and the maximum temperature gradient across the liquid is 8.3×10^6. The Prandtl number of cast iron is approximately 0.2. The product of the Grashof and Prandtl numbers is therefore about 1.66×10^6, which suggests that the natural convection is in the laminar flow regime [47]. The flow during filling is turbulent as shown previously, and the $k-\epsilon$ model is used to simulate the turbulence. The transition from the turbulent to laminar flow takes place gradually as the turbulence kinetic energy is dissipated. The standard $k-\epsilon$ model is valid

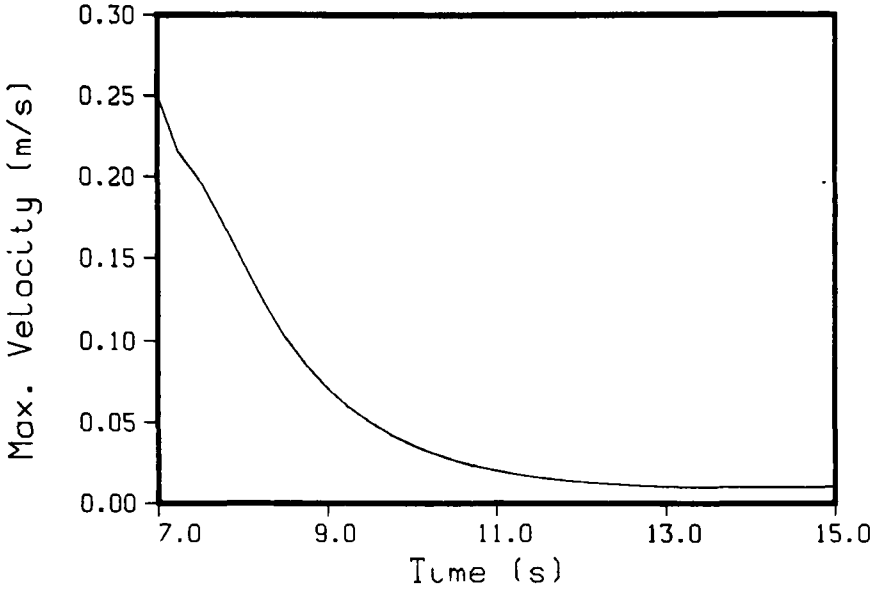

Figure 5.5 Decay of maximum velocity after filling is completed

only for flows with a relatively high level of turbulence [50], therefore at a time 't_t' into the process, an assumption of an abrupt transition from turbulent to laminar flow is made and the computation of turbulence is terminated. Figure 5.5 illustrates that the maximum velocity in the domain decays by an order of magnitude (to the same range as the laminar natural convection velocities) approximately 3 seconds after filling is completed. A transition time $t_t = 10\,s$ (3 seconds after filling) is therefore chosen initially. It is shown subsequently that the computed results are relatively independent of t_t, suggesting the turbulence decays rapidly after filling is completed, and its effects are not significant at later periods.

Latent heat release during solidification

The latent heat release during solidification is taken into account by a source based method. In this technique the latent heat is introduced in the source term of the discretized equation (see *eq*(3.30))

$$a_P\phi_P = a_n\phi_n + a_s\phi_s + a_e\phi_e + a_w\phi_w + Sp\,\phi_P + Su \qquad (5.12)$$

When the above equation is written for $\phi = h$, the discretized form of the energy equation is obtained, for iteration, i, as

$$a_P h_{P_i} = \sum ah + a_P^o[h_P^o + (H_P^o - H_{P_i})] \tag{5.13}$$

where H is the nodal latent heat content and $\sum ah$ is the sum of the products of a and h for the neighboring cells. During the solidification stage the value of H_{P_i} is unknown in $eq(5.13)$ and a model for the latent heat content with temperature is required for its determination. The technique was originally proposed by Voller *et. al.*[127,128], with the equation to update H_{P_i} for isothermal solidification as

$$H_{P_i} = H_{P_{i-1}} + \frac{a_P}{a_P^o} h_{p_i} \tag{5.14}$$

In the present work an equation is derived to treat binary alloys which release part of the latent heat between the liquidus and solidus temperatures and the rest at the solidus temperature. The derivation is also applicable to solidification over a mushy range, as this is a special case of binary phase change. The formulation has been published [1,97] and is presented in the following.

Let the total heat of fusion be L and the heat of fusion at the solidus temperature be L_2. Assuming a linear relation between the temperature (or sensible enthalpy, h) and latent heat release, the following relation between sensible enthalpy and nodal latent heat content H is obtained.

$$h_{P_i} = \varphi_1 H_{P_i} + \varphi_2 \tag{5.15}$$

where

$$\varphi_1 = \frac{h_l - h_s}{L - L_2} \tag{5.16}$$

$$\varphi_2 = h_l - \varphi_1 L \tag{5.17}$$

Rewriting $eq(5.13)$ for the $(i-1)$th iteration involves only replacing the subscript i by $(i-1)$

$$a_P h_{P_{(i-1)}} = \sum ah + a_P^o[h_P^o + (H_P^o - H_{P_{(i-1)}})] \tag{5.18}$$

At the ith iteration the nodal sensible enthalpy has to account for the nodal latent heat, and therefore $eq(5.15)$ has to be satisfied simultaneously with $eq(5.13)$. Substituting h_{P_i} from $eq(5.15)$ into $eq(5.13)$ and eliminating $\sum ah$ with $eq(5.18)$ yields

$$H_{P_i} = \frac{1}{a_P{}^o + a_P\varphi_1}(a_P{}^o H_{P(i-1)} + a_P h_{(i-1)} - a_P\varphi_2) \tag{5.19}$$

This equation defines H_{P_i} in terms of known previous iteration parameters and is applicable only within the liquidus–solidus temperature range. In the derivation of this equation it is assumed that $\sum ah$ does not change between iterations. This assumption becomes increasingly accurate as the iterative process approaches convergence.

The nodal sensible enthalpy remains constant at h_s while latent heat is released at the solidification temperature. Substituting $h_{P_i} = h_s$ in $eq(5.13)$ and eliminating $\sum ah$ with $eq(5.18)$ yields

$$H_{P_i} = H_{P(i-1)} + \varsigma\frac{a_P}{a_P{}^o}(h_{(i-1)} - h_s) \tag{5.20}$$

The above equation defines H_{P_i} in terms of previous iteration parameters for isothermal solidification. The same assumption to eliminate $\sum ah$ has been made, as in $eq(5.19)$. The term ς is an under–relaxation factor (about 0.8) to aid convergence. The latent heat release is taken into account in the solution of $eq(5.13)$. The term H_{P_i} is evaluated by $eq(5.19)$ if $h_s < h \leq h_l$ and $eq(5.20)$ if $h = h_s$.

In this technique the latent heat content is directly coupled to the nodal temperature through the source term of the energy equation, and fairly accurate results for non–isothermal solidification of metals are obtained. The formulation suffers from a characteristic limitation of some weak methods, *i. e.* it produces an oscillating solution for isothermal solidification [87]. The overall accuracy of this method is comparable to the enthalpy formulation [122]. An advantage of this method is that the value of the solid fraction is explicitly available through the function $(1-H_P/L)$.

This is required to couple solidification to other phenomena, for example suppression of flow velocities or special interface boundary conditions.

Treatment of the momentum equations

Treatments of the momentum equations to simulate flow during solidification are reviewed in Chapter 1. The Fixed Velocity Method is appropriate for pure materials, which solidify isothermally (with a macroscopically planer solid–liquid interface [31]).

In the present work the solidification of Cast Iron of near eutectic composition is being simulated. A mushy region exists between the liquidus and the solidus temperatures and at the solidus temperature while latent heat is being released. The morphology of the mushy region is very difficult to describe accurately, as it is a function of composition, cooling rate and segregation [24,77,78]. The transport mechanisms in this region are very complex; at high solid fraction the mushy region may behave as a porous medium and at low solid fraction the flow may carry freshly nucleated solid particles in suspension. There may be an additional drag between the liquid and the solid particles. The flow may also be non–Newtonian because of the interaction of the liquid metal and solid particles.

In the present work a new model is presented to treat the flow in the mushy region. The model is based on the following assumptions.

1. *The mushy region consists of two zones; the nucleation zone and the porous medium zone* (Figure 5.6). This assumption is made because the morphology of the mushy region changes significantly with the solid fraction and an accurate treatment cannot be provided assuming a single type of structure. In the actual solidification process nucleation starts around the inoculant particles suspended in the liquid. The number of nucleation sites as well as the size of the newly solidified particles increase with the solid fraction. The formation

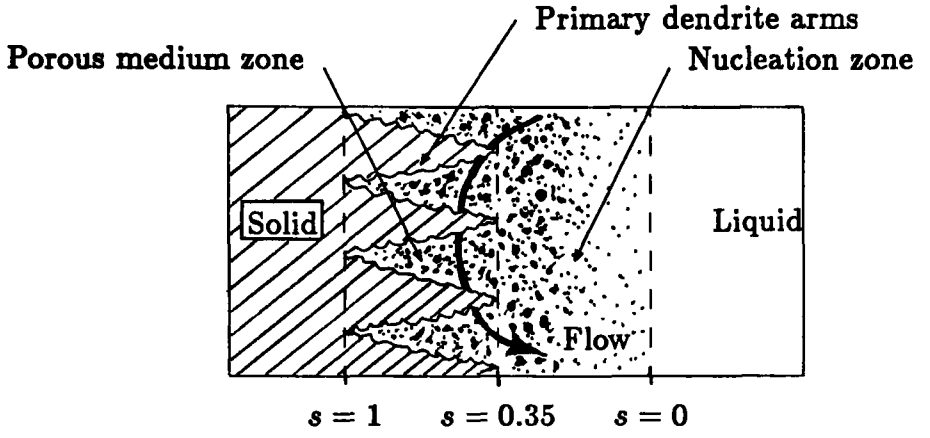

Figure 5.6 Morphology of the mushy region

of dendrites also begins at some point with increasing solid fraction. Primary dendrite arm lengths of approximately $0.5 \times 10^{-4} m$ were measured, by microscopic examination of etched solidified samples [24]. The concentration of the dendrites increases with the solid fraction until solidification is completed.

2. *The flow in the nucleation zone is Newtonian.* This assumption is probably not completely valid because of the large number of solid particles in suspension, and the variation of viscosity near the phase change point. The transition from Newtonian to non–Newtonian flow in suspensions has been observed to take place for values of solid fraction between 0.25 to 0.40 [32] on the basis of experimental data for a number of different types of suspensions from a number of different sources.

3. *The resistance to the flow in the nucleation zone is due to drag, flow area obstruction, and inelastic collisions of the nuclei.*

4. *The shape of the nuclei particles is spherical.* This assumption is made because the actual shape of the nuclei is a function of composition and solid fraction and is not known. The experimental correlation used for the fluid viscosity in the nucleation zone is valid for spherical solid particles.

5. *The suspended particles are rigid spheres, with a radius which is large com-*

pared to the radius of the solvent molecules yet small in comparison with the characteristic dimensions of the domain. This assumption is valid, as the maximum diameter of the solidified nuclei is close to the nucleation cell diameter, measured to be approximately $1.0 \times 10^{-4} m$, by microscopic examination of etched solidified samples [24].

6. *The transition from the nucleation zone to the porous medium zone takes place at a solid fraction* $s_t = 0.35$. This transition criterion is based on experimental data of liquid metal penetration in mushy zones. Penetration is defined as the depth in the mushy zone, measured from the liquidus interface, to the point at which significant liquid metal flow occurs. Penetration depth studies are done by radioactive tracer techniques in which radioactive tracer particles are introduced in the melt, and after some time the solidifying sample is quenched. The liquid metal penetration is then determined from the distribution of the tracer particles in the quenched sample. A number of experimental studies [33,34,86,113] have shown that the liquid metal penetration in mushy zones is significantly reduced for solid fraction greater than 0.34–0.37. This suggests that the morphology of the mushy region changes significantly in the solid fraction range 0.34–0.37. In the present work it is assumed that at $s_t = 0.35$ the morphology of the mushy region changes from that of a nucleation zone to a porous medium zone.

7. *The flow in the porous medium zone is Newtonian and obeys D'Arcy's Law.* This law is widely used to compute flow in porous media.

The treatment of the momentum equations according to the model described above is as follows:

The solid fraction of each cell is monitored. If the solid fraction is zero, the cell is in the liquid phase and no special treatment is necessary.

If the solid fraction is greater than 0 and less than 0.35, the cell is assumed to be in

the nucleation zone. In this case the fluid is assumed to be a suspension in which the solidified spherical nuclei are distributed homogeneously in the liquid metal. The viscosity of suspensions of solid spherical particles can be written [32] as a function of the solid fraction as

$$\mu = \mu_l e^{2.5s/(1-ks)} \tag{5.21}$$

The above equation is derived on the basis of semi-empirical models relating the effective viscosity of the suspension to the concentration of the suspended particles by polynomials. Such models appear to be well accepted and widely used to predict the flow behavior of suspensions [32]. In the above equation k is an experimental parameter. The above equation has been reported to fit experimental data well with $1.35 < k < 1.9$ [32]. In the present work $k = 1.4$ has been used. Equation 5.21 is used to determine the fluid viscosity in the nucleation zone.

If the solid fraction is greater than 0.35 but less than 1.0, the cell is in the porous medium zone. The D'Arcy law is valid for flow in a porous media

$$U = -\frac{K_p}{\mu(1-s)}\nabla P \tag{5.22}$$

where K_p is the specific permeability of the solid-liquid zone. Poirier [86] has correlated permeability data from a number of sources for various solid fractions and dendrite arm spacings. The data base used was mainly of $Pb - Sn$ alloys and borneol-paraffin organics having the same dendritic morphology as that for metallic alloys. The following correlation was proposed for the permeability (for flow normal to the primary dendrite arms) on the basis of a multilinear regression analysis of the data

$$K_p = 1.73 \times 10^{-3}(d_1/d_2)^{1.09} d_2^2 (1-s)^3/s^{0.749} \tag{5.23}$$

The data base for the correlation is for the range $0.34 < s < 0.81$. In the present work it is assumed that the dendritic morphology of cast iron is similar to that of other metallic alloys. The correlation expressed by the above equation is assumed to be valid also for $s > 0.81$. It is assumed that the correlation is also valid for flow

which is not normal to the primary dendrite arms. This assumption will not induce significant error as the bulk of the flow is normal to the primary dendrite arms, as shown in Figure 5.6.

The pressure loss in the porous medium can be written by rearranging $eq(5.22)$ so that

$$\nabla P = -\frac{\mu(1-s)}{K_p}U \tag{5.24}$$

This pressure loss is incorporated in the source term of the momentum equation so that

$$B = -\frac{\mu(1-s)}{K_p}$$

$$Sp = Sp + \{\varsigma B + (1-\varsigma)B_o\} \tag{5.25}$$

where B_o is the previous iteration value and ς is an under-relaxation factor (about 0.3). The permeability K_p is determined using $eq(5.23)$ with the primary and secondary dendrite arm spacings

$$d_1 = 228 \times 10^{-6} m$$

$$d_2 = 100 \times 10^{-6} m$$

obtained from Flemings [31], for iron, for an average cooling rate determined by

$$\frac{(T_{pour} - T_{solidus})}{\text{Solidification time}} = 0.34^o C/s$$

The fluid velocities in the fully solidified region ($s = 1$) are set to zero by setting a_p, a_n, a_s, a_e, a_w and Su to zero in $eq(\ 3.30)$ and setting $Sp = 10^{30}$ for $\phi = u, v$.

5.3.4 Coupling the casting and mold computations

The computations for the casting and mold are carried out on separate grids as shown in Figure 5.2, and coupled at the mold casting interface. A heat flux condition

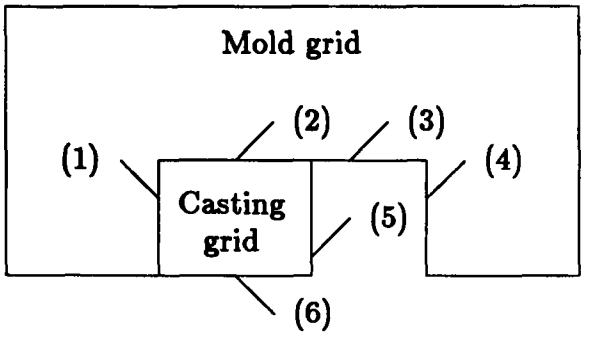

Figure 5.7 Mold casting coupling during filling

is used for both the mold and casting regions at the interface. This condition is discussed in the following for the filling and solidification stages.

Coupling during the filling process

Figure 5.7 shows the grid during the filling process, with different segments of the interface identified from (1) to (6). The heat transfer across each of these segments is discussed in the following.

(1) This segment couples the bottom of the casting to the sand base. The grid is arranged such that the radial dimension of the casting and mold cells for each 'J' are equal. This creates a one–to–one correspondence between the cells of the casting and the sand base, as shown in Figure 5.8(a). The heat flux imposed at the casting cell is therefore

$$H_{c,b} = \frac{(T_c - T_m)}{(\Delta x_c/k_c + \Delta x_m/k_m + R_b)} \tag{5.26}$$

and the heat flux imposed at the mold is

$$H_{m,b} = -H_{c,b} \tag{5.27}$$

(2) This segment couples the side wall of the casting to the mold. The axial dimension of the casting grid varies during the filling process, therefore, it is not possible

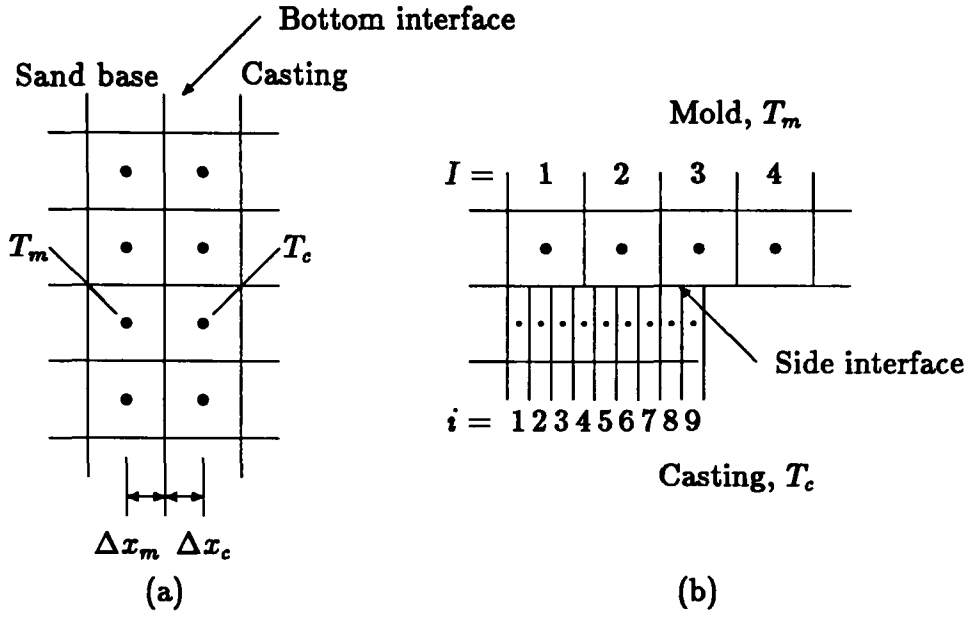

Figure 5.8 Mold casting interface during filling

to establish a one–to–one correspondence between the cells of the casting and the mold.

Figure 5.8(b) shows a section of this segment with the mold and the casting grids. In this case, at the beginning of each time step, a correspondence is determined between the casting and the mold cells by geometrical considerations. This is done by assigning a set of casting cells to each mold cell such that the ratio of the mold cell interfacial area to the casting cell set interfacial area is as close to unity as possible. For example, in Figure 5.8(b), the interface casting cells for $i = 1, 2, 3$ correspond to the mold cell for $I = 1$, casting cells for $i = 4, 5, 6, 7$ correspond to the mold cell for $I = 2$, and casting cells for $i = 8, 9$ correspond to the mold cell for $I = 3$.

At each iteration, the average temperature is determined for each set of casting cells that corresponds to one mold cell. In the example (see Figure 5.8(b)), the average casting wall temperature T_c, is determined separately for the casting cells

for $i = 1,2,3$, for $i = 4,5,6,7$ and for $i = 8,9$. The different components of the interface heat transfer are conduction at spot contacts

$$Con = \frac{\eta_w}{(\Delta r_c/k_c + \Delta r_m/k_m + R_s)}$$

conduction through the air in the gap

$$Con_a = (1 - \eta_w)k_a/\delta$$

and radiation

$$Rad = (1 - \eta_w)\sigma\epsilon\{T_c + 273.15 + T_m + 273.15\}\{(T_c + 273.15)^2 + (T_m + 273.15)^2\}$$

where η_w is the fraction of the wall interfacial area at which the mold and casting are in contact. The heat flux from the casting is computed as

$$H_{c,w} = (T_m - T_c)\,(Con + Con_a + Rad) \tag{5.28}$$

and the heat flux imposed at the mold is

$$H_{m,w} = -H_{c,w}A_c/A_m \tag{5.29}$$

where A_c/A_m is the ratio of the interfacial area of the casting cell set and the mold cell. It should be noted that for the mesh used in the present computations this ratio is mostly in the range of 0.95–1.05.

(3), (4), (5) The free surface of the liquid metal (5) loses heat to the side (3) and top (4) walls of the mold. Convection in the air above the free surface of the liquid metal is neglected. Radiation between the mold surfaces (3) and (4) is neglected because

$$|T_3 - T_4| \ll |T_5 - T_3|$$

and

$$|T_3 - T_4| \ll |T_5 - T_4|$$

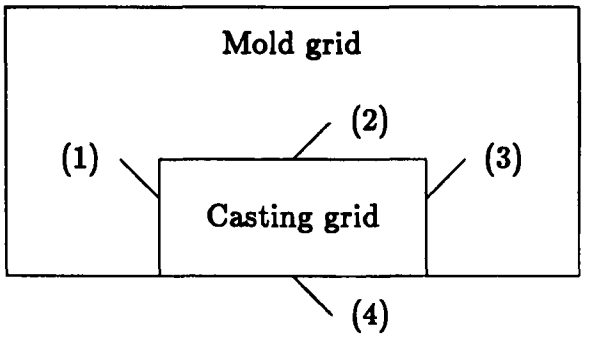

Figure 5.9 Mold casting coupling after filling

where T_3, T_4 and T_5 are the average temperatures of the surfaces (3), (4) and (5) respectively. The heat flux from the surface of the liquid metal (5) is given as

$$H_{c,s} = F_{s,w}\sigma\epsilon(T_5^4 - T_3^4) + F_{s,t}\sigma\epsilon(T_5^4 - T_4^4) \tag{5.30}$$

the heat flux to the mold side wall (3) is given as

$$H_{m,w} = F_{s,w}\sigma\epsilon(T_5^4 - T_3^4) \tag{5.31}$$

and the heat flux to the mold top wall (4) is given as

$$H_{m,t} = F_{s,t}\sigma\epsilon(T_5^4 - T_4^4) \tag{5.32}$$

(6) The boundary (6) is the axis of symmetry. An adiabatic condition, (zero heat flux) is imposed.

Coupling after the mold is filled

Figure 5.9 shows the grid after filling, with different segments of the interface identified from (1) to (4). The grid is arranged such that after filling, there is a one–to–one correspondence between the mold and the casting cells. The heat flux conditions at the segments are given as follows:

(1) This segment couples the bottom of the casting to the sand base. The heat transfer at this segment is described in the previous section, where the interface conditions during filling are described.

(2) This segment couples the side walls of the casting and the mold. The grid is arranged such that, after filling, there is a one–to–one correspondence between the cells of the casting and the mold. The different components of the interface heat transfer are conduction at spot contacts

$$Con = \frac{\eta_w}{(\Delta r_c/k_c + \Delta r_m/k_m + R_w)}$$

conduction through the air in the gap

$$Con_a = (1 - \eta_w)k_a/\delta$$

and radiation

$$Rad = (1 - \eta_w)\sigma\epsilon\{T_c + 273.15 + T_m + 273.15\}\{(T_c + 273.15)^2 + (T_m + 273.15)^2\}$$

The heat flux from the casting is computed as

$$H_{c,w} = (T_m - T_c)\,(Con + Con_a + Rad) \tag{5.33}$$

and the heat flux imposed at the mold is

$$H_{m,w} = -H_{c,w} \tag{5.34}$$

In the above equations η_w represents the fraction of the interfacial area at which the mold and the casting are in contact. The interface dynamics (interface contact resistance and variation of η_w with time) used in this chapter are the same as those used for the plate casting work described in Chapter 2. These assumptions and the values for the thermal contact resistance and gap formation time are described in Section 2.3.1.

(3) This section represents the interface between the top walls of the casting and the mold. The different components of the interface heat transfer are conduction at spot contacts

$$Con = \frac{\eta_t}{(\Delta x_c/k_c + \Delta x_m/k_m + R_t)}$$

conduction through the air in the gap

$$Con_a = (1 - \eta_t)k_a/\delta g$$

and radiation

$$Rad = (1 - \eta_t)\sigma\epsilon\{T_c + 273.15 + T_m + 273.15\}\{(T_c + 273.15)^2 + (T_m + 273.15)^2\}$$

The heat flux out of the casting is computed as

$$H_{c,t} = (T_m - T_c)\,(Con + Con_a + Rad) \tag{5.35}$$

and the heat flux imposed at the mold is

$$H_{m,t} = -H_{c,t} \tag{5.36}$$

(4) The boundary (4) is the axis of symmetry. An adiabatic condition, (zero heat flux) is imposed.

5.3.5 Solution algorithm

The SIMPLE algorithm described in Chapter 3 is used as the solution technique. The mold and the casting computations are coupled by the heat flux condition at each time step.

At each iteration, the interfacial heat flux is first determined based on the mold and casting temperatures computed during the previous iteration. The momentum

and the energy equations for the casting region are then solved, followed by the solution of the energy equation in the mold region, using the interfacial heat flux computed at the beginning of the iteration as a boundary condition. The value of the interfacial heat flux is correct at the final iterations when the temperature fields attain their correct values.

It should be mentioned that the coupling procedure described above may cause convergence problems if the computed interface temperatures during the iterative process deviate widely from the correct values. This may occur if the procedure is used in a steady state case, with an initial guessed temperature field deviating widely from the correct solution. A transient solution is obtained in the present study, in which the temperature field from the previous time step is used as an initial guess. In this case the guessed initial temperature field is close to the final solution and convergence problems are not experienced.

The temperature fields of the mold and casting are coupled at the iteration level in the technique described above. This approach preserves the implicit nature of the SIMPLE algorithm and a time step limiting condition is not needed. Another approach, which could have been used, would be to couple the casting and mold temperature fields at the time step level. In this case the computations for the mold and casting regions would be carried out at alternate time steps, and the previous time step values of the mold or casting wall temperatures would be used to determine the interface heat flux. This procedure would probably be more stable, as at each time step the computations would only be carried out for either the mold or the casting region. This is an explicit approach however, and a time step limitation may be required. The implicit approach is chosen in the present work to avoid the time step limitation.

5.4 Verification of convection computations

Natural convection is computed in this study using the Boussinesq approximation as described previously. This section describes some additional experimental and computational work carried out to verify the natural convection calculations.

Experimental work

Tests[2] are done in an annular crucible of length $0.085\,m$, inner diameter $0.019\,m$ and outer diameter $0.038\,m$, as shown in Figure 5.10. The crucible is placed in an oven at a uniform temperature of $230\,^{o}C$. The top and bottom surfaces are insulated and the inner wall is cooled by a water coil buffered in oil. A melt of a *Pb–Bi* alloy is contained in the annular space between the inner and outer walls of the crucible. A natural convection flow pattern is obtained in the melt due to the temperature gradient between the inner and outer walls. Temperature measurements are carried out in the melt by a 0.5 *mm* thermocouple mounted on a traversing mechanism. The final temperature readings are taken after a sufficiently long period to ensure that a steady state temperature field is obtained.

Mathematical modelling

Mathematical modelling of the natural convection is carried out using the Finite Volume Method and the Boussinesq approximation. Two mesh sizes (20×20 and 35×35) are used to verify grid independence. The results presented in this study are computed on the 35×35 mesh shown in Figure 5.11. The thermophysical properties of the melt are shown in Table 5.2. The product of the Grashof and Prandtl numbers for the test case is 1.3×10^5, therefore the flow is laminar [47].

[2]The experimental work reported in this section was done in collaboration with Mr. D. Maeda, at the Department of Metallurgical Engineering, U.B.C.

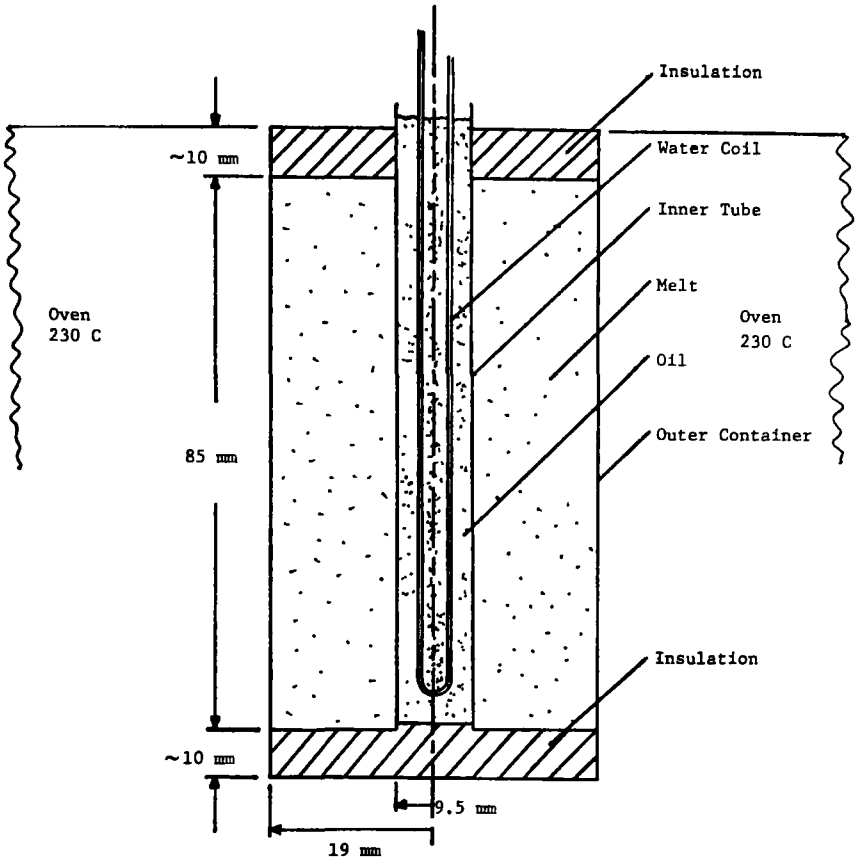

Figure 5.10 Schematic of the annular crucible

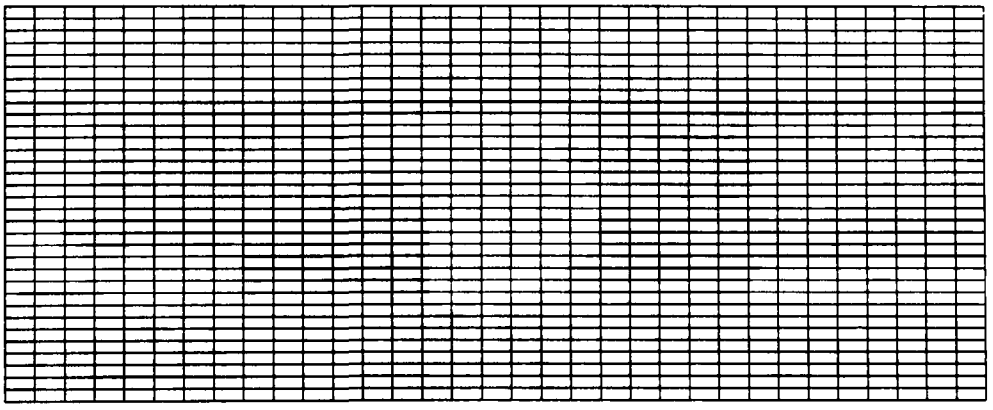

Figure 5.11 Mesh used to compute the flow in the crucible

Table 5.2 Physical properties of *Pb–Bi* Alloy

$T_{melting}$ °C	ρ kg/m^3	μ kg/ms	k $J/ms°C$	C $J/kg°C$	β C^{-1}
124	10460	1.70×10^{-3}	10	147	1×10^{-4}

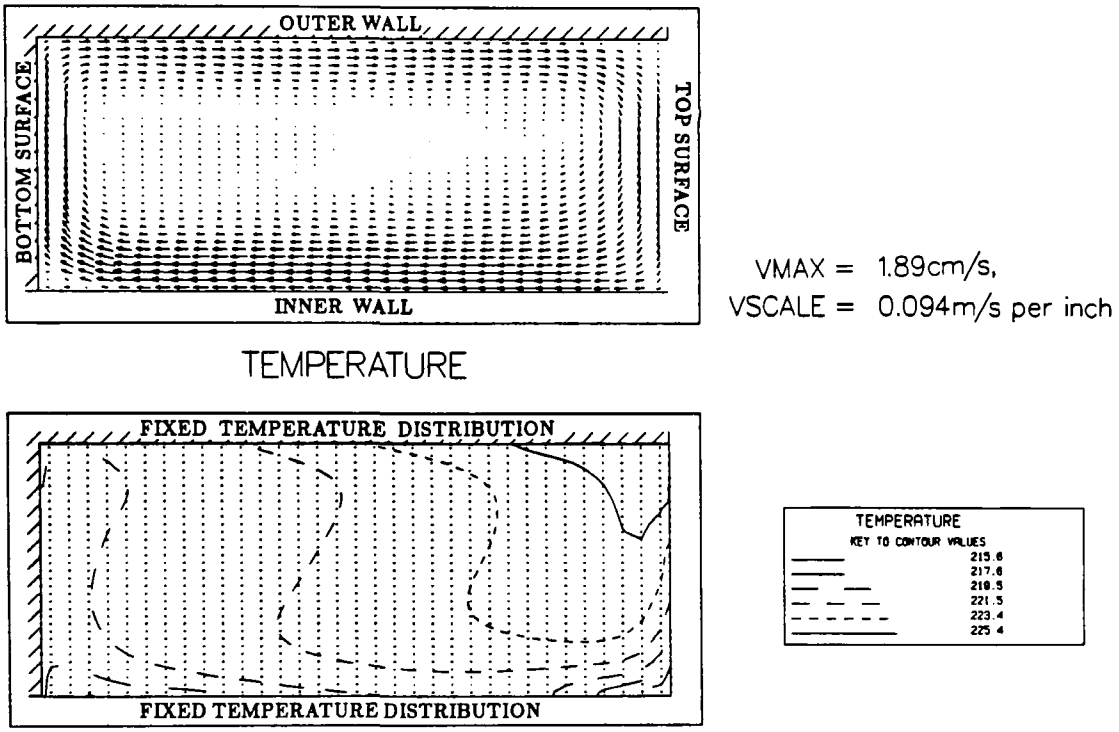

Figure 5.12 Velocity and temperature distribution during natural convection

Wall conditions ($U = 0, V = 0$) are used at each of the boundaries for the momentum equations. The temperatures at the boundaries are imposed to those measured experimentally in the fluid close to the crucible walls.

Results and discussion

Figure 5.12 shows the computed velocity and temperature fields. The melt in the region of the relatively cooler inner wall becomes more dense and flows downwards.

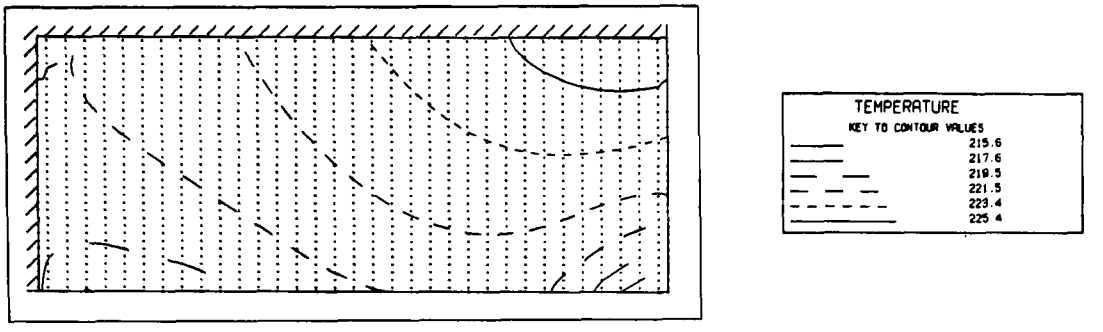

Figure 5.13 Temperature field obtained by heat conduction solution

A maximum velocity of approximately 2 cm/s is obtained close to the cooled wall. The temperature field presented in Figure 5.12 can be compared with that shown in Figure 5.13 obtained for conduction only. It can be seen that the convection of the melt significantly affects the temperature distribution.

Figure 5.14 illustrates the computed temperature distribution (with convection and conduction) together with the experimental measurements. The thick contours show the experimental results and the thin contours represent the computed results. It can be seen that the computed results reproduce the shape of the experimental contours very well. This indicates that the overall computed velocity field (illustrated in Figure 5.12) is quite accurate. It should be noted that the contours are only $1\,^{o}C$ apart and that the agreement between the experimental and computed results is excellent if the experimental contours are moved towards the right by about $2\,cm$. This 'shifting' of the results is not unreasonable because the reference level of the temperature measurements, determined using an ice bath, can be inaccurate by $1^{o}C$. The temperature measurements near the crucible walls can be inaccurate because of the strong temperature gradients in these regions. The measurements are made with a 0.5 mm diameter thermocouple, which spans approximately two grid cells. These errors are then transferred to the computations as the measured temperatures are used as boundary conditions. An indication of the inaccuracy is that the experimental contours appear to be normal to the heated wall which clearly

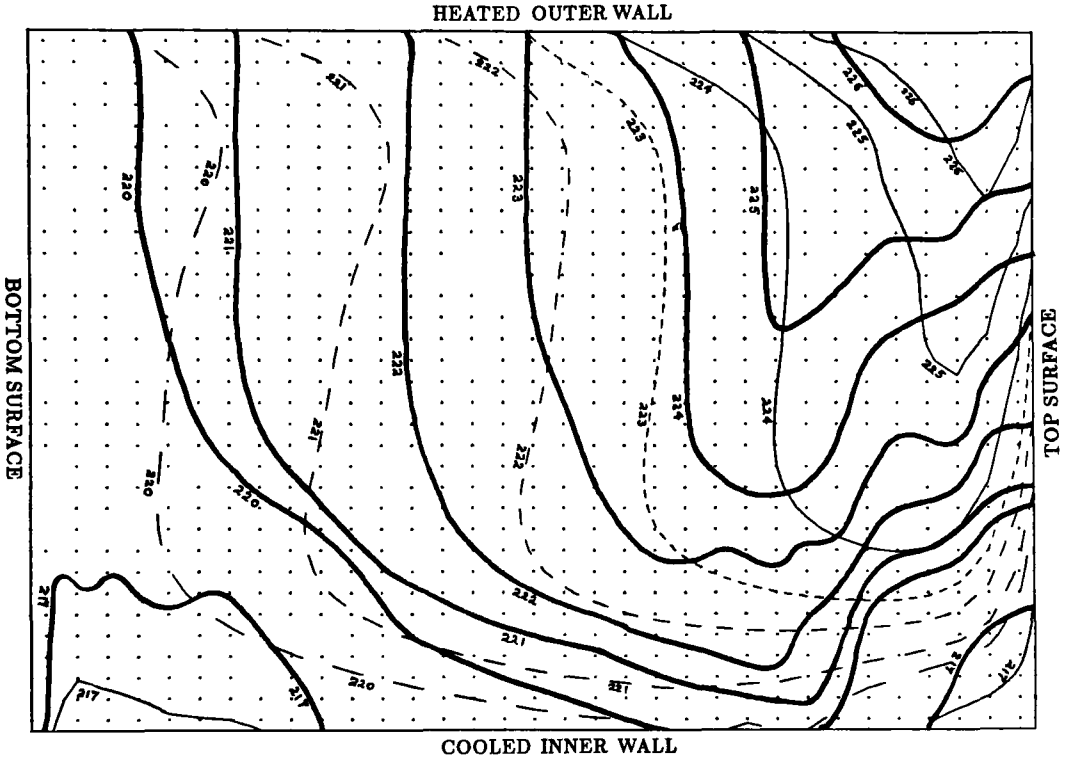

Figure 5.14 Experimental (thick lines) and computed (thin lines) temperature distributions in the crucible

cannot be the case. Considering the factors mentioned above, and the errors in the estimation of the thermophysical properties of the melt, it is felt that the agreement between the computed and experimental results is very good. It is therefore concluded that natural convection can be computed fairly accurately using the Finite Volume Method along with the Boussinesq approximation.

5.5 Results and discussion

5.5.1 Filling stage

Figures 5.15–5.18 show the velocity, turbulent kinetic energy, effective viscosity and temperature distributions at various times during the filling process.

The inlet jet penetrates from the bottom, flows to the top and then radially outwards forming a vortex under the free surface. The vortex formed by the jet causes a recirculatory flow pattern in the region bounded by the mold walls and the jet. It can be seen that the flow field is strongly influenced by the jet and therefore the effects of the incorrect initial conditions are not expected to induce significant error. The strong influence of the jet remains significant until the end of the filling stage.

The turbulent kinetic energy contours have been non–dimensionalized to U_{in}^2 where U_{in} is the inlet velocity. The effective viscosity has been non–dimensionalized to the laminar viscosity. The highest values of the turbulent kinetic energy and the effective viscosity are in the regions where the jet spreads into the fluid and in the vortex. The effective viscosity is between one and two orders of magnitude larger than the laminar viscosity.

The temperature contours show that the highest temperatures in the fluid occur

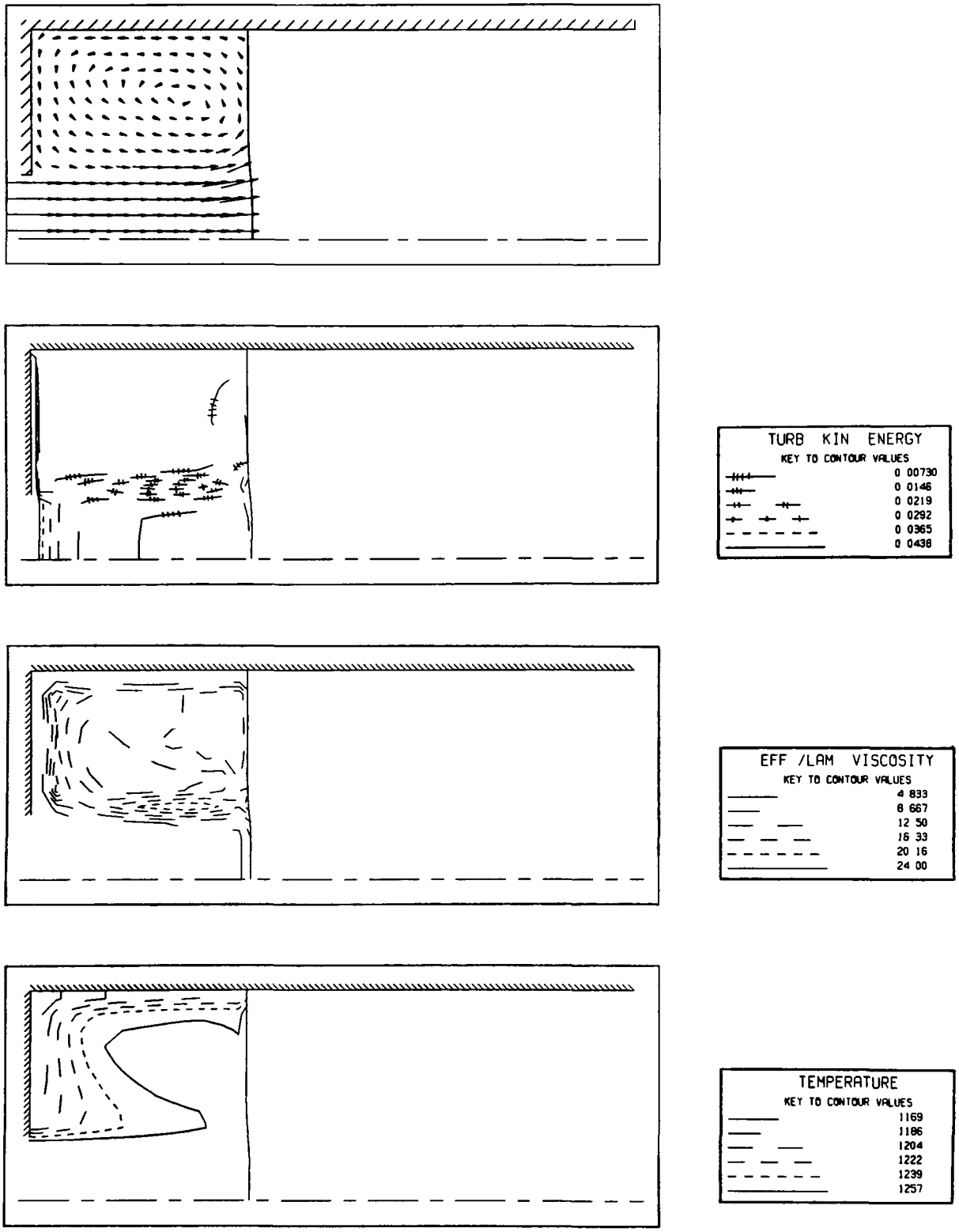

Figure 5.15 Velocity, turbulent kinetic energy, viscosity and temperature fields during filling. Time = 2 s, Level = 0.055 m, Velocity scale = 0.27 $m/s\,cm$.

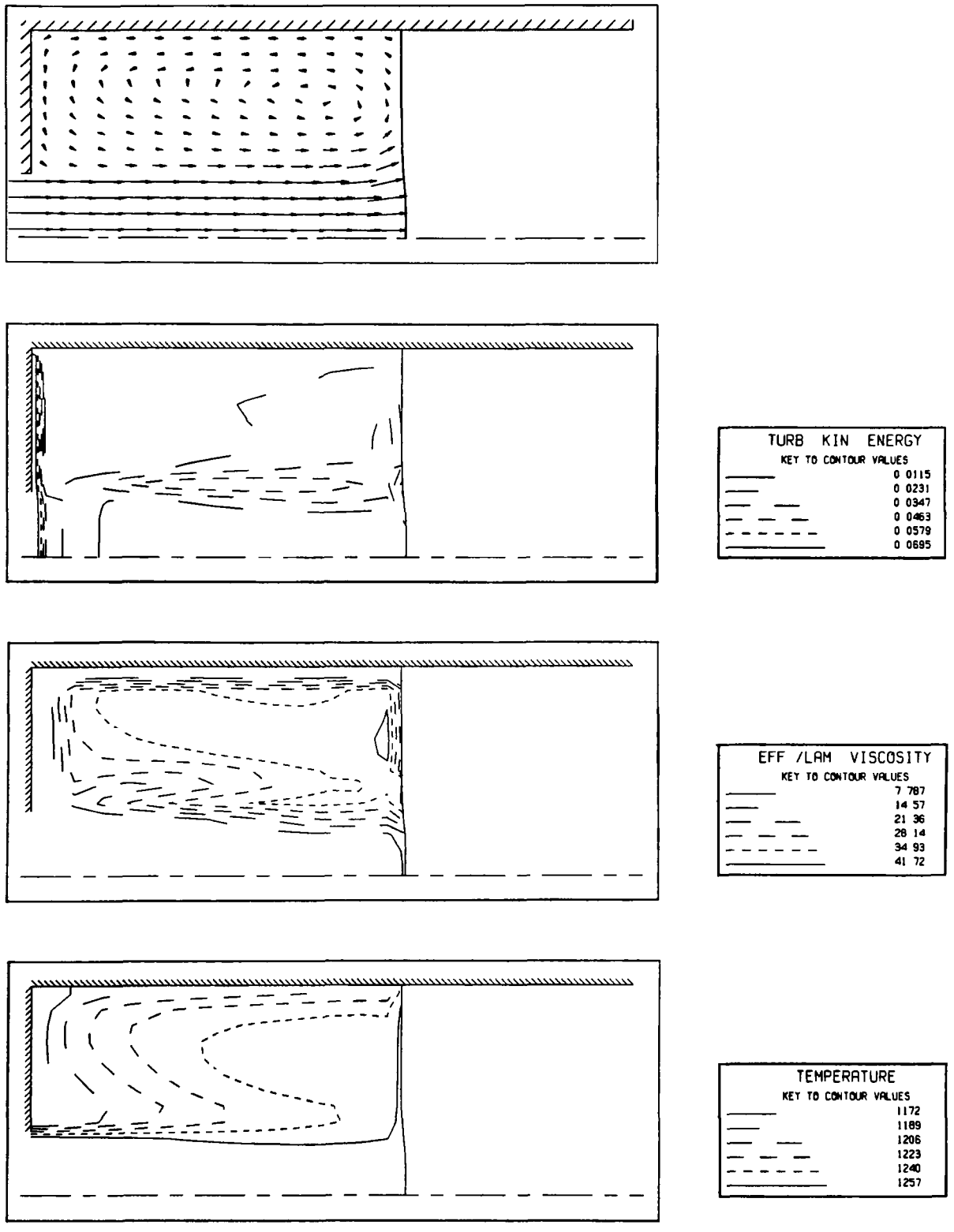

Figure 5.16 Velocity, turbulent kinetic energy, viscosity and temperature fields during filling. Time = 4 s, Level = 0.095 m, Velocity scale = 0.28 $m/s\,cm$.

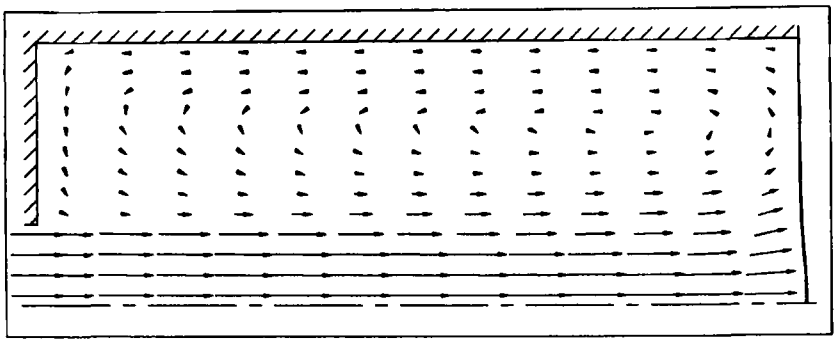

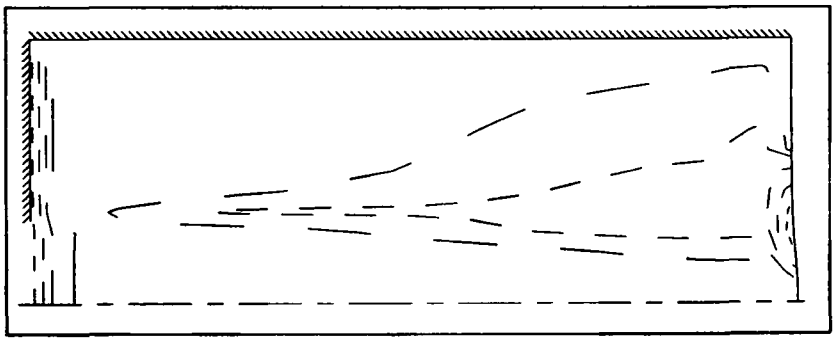

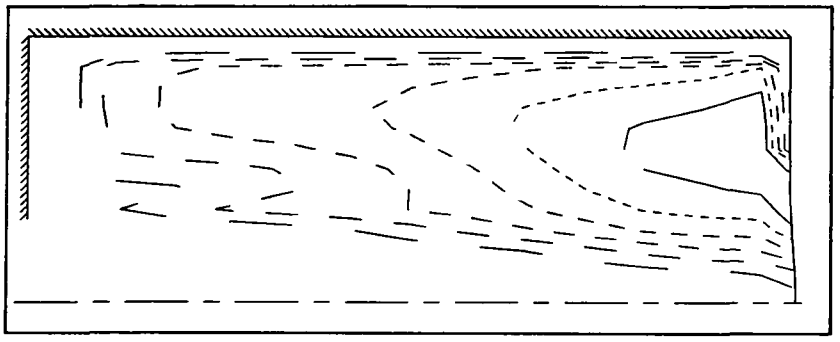

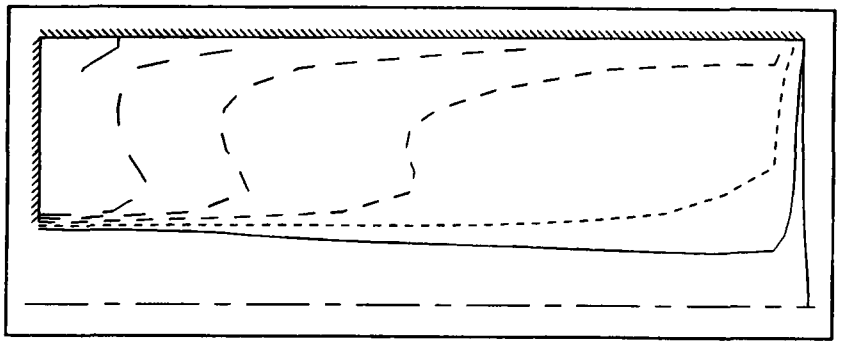

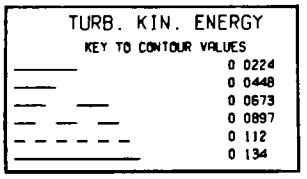

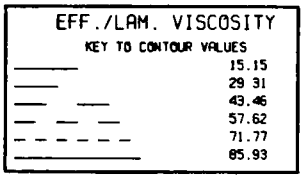

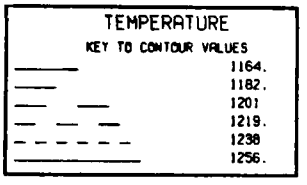

Figure 5.17 Velocity, turbulent kinetic energy, viscosity and temperature fields during filling. Time = 7 s, Level = 0.0154 m, Velocity scale = 0.31 $m/s\,cm$.

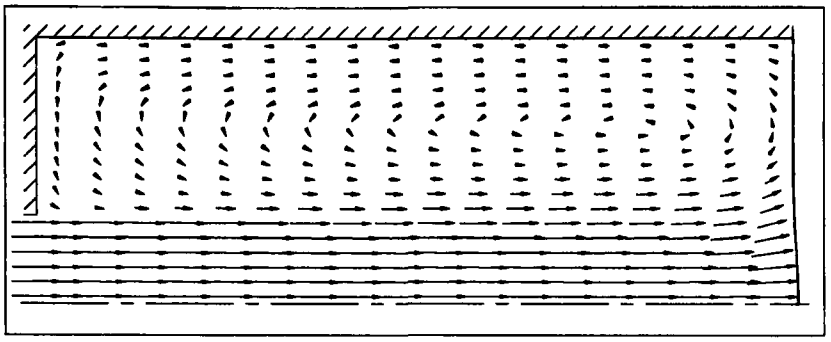

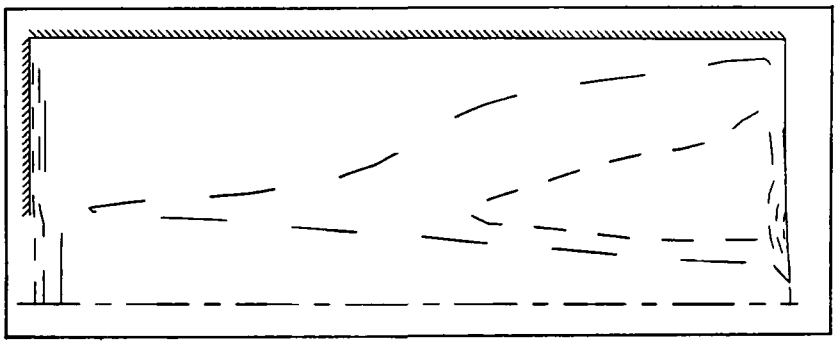

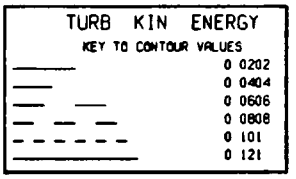

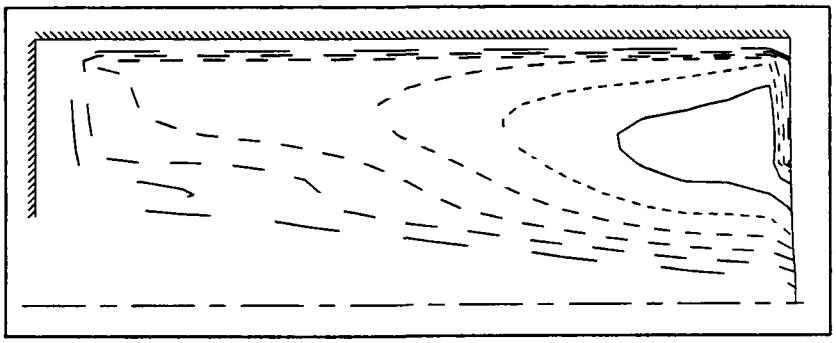

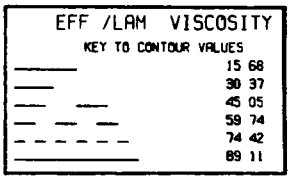

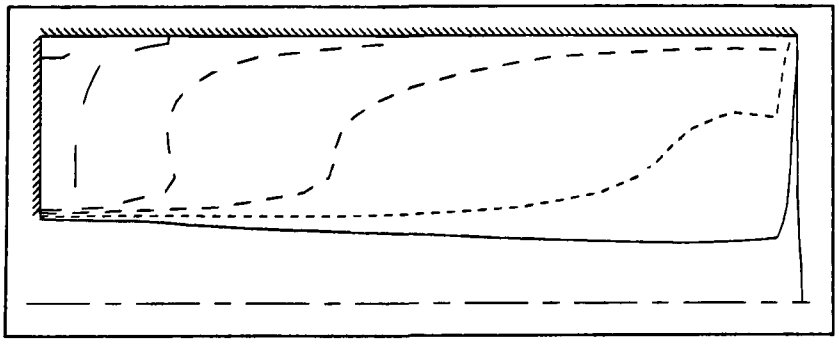

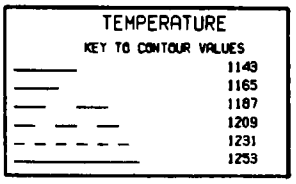

Figure 5.18 Velocity, turbulent kinetic energy, viscosity and temperature fields. Fine mesh case. Time = 7 s, Level = 0.0154 m, Velocity scale = 0.281 $m/s\,cm$.

in the core of the jet and in the upper regions where the jet spreads radially outwards. The temperatures then drop progressively at increasing radii (close to the mold walls). It can be seen that (at time 7 s, Figures 5.17 and 5.18) at the end of the filling stage the temperature distribution is *not* uniform, as incorrectly assumed almost universally in the literature.

The results of the computations based on the fine mesh are very similar to the coarse mesh results, indicating that the solution is not very sensitive to the mesh size. A typical comparison can be seen for the end of the filling stage (at time 7 s) in Figures 5.17 and 5.18 for the coarse and fine mesh respectively. It can be seen that the results for the two cases are very similar. The computations using the fine mesh are relatively expensive as discussed subsequently.

5.5.2 Solidification stage

Solidification in the presence of convection

Figures 5.19 to 5.26 show the temperature and velocity distributions during the solidification process. The results are shown for cases in which both conduction and convection are computed (Figures 5.19(a) to 5.26(a)) and in which only conduction is computed (Figures 5.19(b) to 5.26(b)). The 1144 $°C$ level contours represent the solidus interface.

Figures 5.19(a) and (b) show the temperature and velocity fields 20 s into the process. A recirculatory flow pattern can be seen, in which the fluid near the mold wall is cooled, flows down and rises in the central region. A vortex forms at the bottom near the mold walls as the fluid is directed radially inwards. A smaller vortex forms at the top near the axis of symmetry. It can be seen that a fairly strong convective field results with a maximum velocity of about 0.038 m/s near the mold walls and a Grashof number of 4.8×10^6.

The temperature contours show steep thermal gradients near the mold walls. The cooler fluid flowing down near the mold walls rises relatively slowly in the central region, causing the temperature field to be stratified close to the symmetry axis. The convective results show that no significant solidification takes place $20\,s$ into the process. Figure 5.19(b) shows that if convection is neglected the computations indicate that a solidified skin forms near the mold walls. Cooling near the walls is much less rapid when convection is accounted for, as the fluid at higher temperature from the inner regions of the casting flows to the outer regions.

Figures 5.20(a) and (b) show the temperature and velocity fields $40\,s$ into the process. The convection results indicate a solidified shell to have formed at the lower regions of the mold walls. The liquid metal gets cooler as it flows downwards, therefore, solidification starts first at the lower region of the mold walls. A small vortex forms at the top side because the solid fraction (in the region marked 'A') near the upper half of the mold wall is fairly high therefore the flow cannot penetrate this region and is deflected inwards. The maximum velocity in this case is $0.013\,m/s$ with a Grashof number of 1.2×10^6. The conduction results show a thicker solid shell to have formed. It can be seen that the heat flow is essentially one–dimensional into the cast iron mold. There is very little loss to the sand base and the top.

Figure 5.21(a) shows that a regular recirculatory flow pattern is established $80\,s$ into the process. The maximum velocity is about $0.004\,m/s$, with a Grashof number of 7×10^4. Figure 5.21(b) shows that the heat flow is still one–dimensional. The maximum velocity is reduced by half $120\,s$ into the process, as shown in Figure 5.22(a). The solid fraction is high in the bottom region, allowing little penetration of the liquid metal.

Figures 5.23 and 5.24 show the advancement of the solidus front in the central region of the casting. It should be noted that the casting can be removed from the mold at time $220\,s$ (Figure 5.24) after the liquid metal is enclosed in the solidified shell. An interesting observation is that solidification appears to be taking place

faster at the top if only conduction is computed (Figure 5.23(b) and 5.24(b)) and faster at the bottom if convection is also computed (Figure 5.23(a) and 5.24(a)). When conduction only is computed, then heat transfer from the upper region of the casting to the sand layer at the top causes faster solidification at the top. When liquid metal convection is computed, however, the heat content of the liquid metal is redistributed and the heat loss from the top becomes negligible as compared to the heat loss from the sides. A thicker shell therefore solidifies at the bottom of the side walls.

Figures 5.25 and 5.26 show the final stages of solidification and the temperature field just after solidification. It can be seen that the last region to solidify is the upper central region. It is important to accurately predict the spatial position of this region as this is the usual location of the shrinkage cavity and segregation defects. This location can be 'moved' to a more desirable region by a strategic placement of gates and/or chills, so that the defects can later be machined off after the casting is ejected from the mold.

Comparison with experimental data

Figures 5.27 to 5.36 show the temperature variation with time at the thermocouple locations shown by the mold–casting icons as well as in Figure 5.1. The computed results are shown with two sets of experimental data. A comparison of the data shows the reproducibility of the experimental results. The experimental results are accurate to within $\pm 2\,^{o}C$. The computed results are shown with and without convection. The solidification times can be deduced from the sharp temperature drop and change of slope of the cooling curves after the $1144\,^{o}C$ eutectic arrest.

Figures 5.27, 5.29 and 5.31 show the temperatures in the mold at the bottom (1), middle (3) and top (5) thermocouple locations respectively. It can be seen that the mold temperatures are predicted quite accurately. The conduction and combined

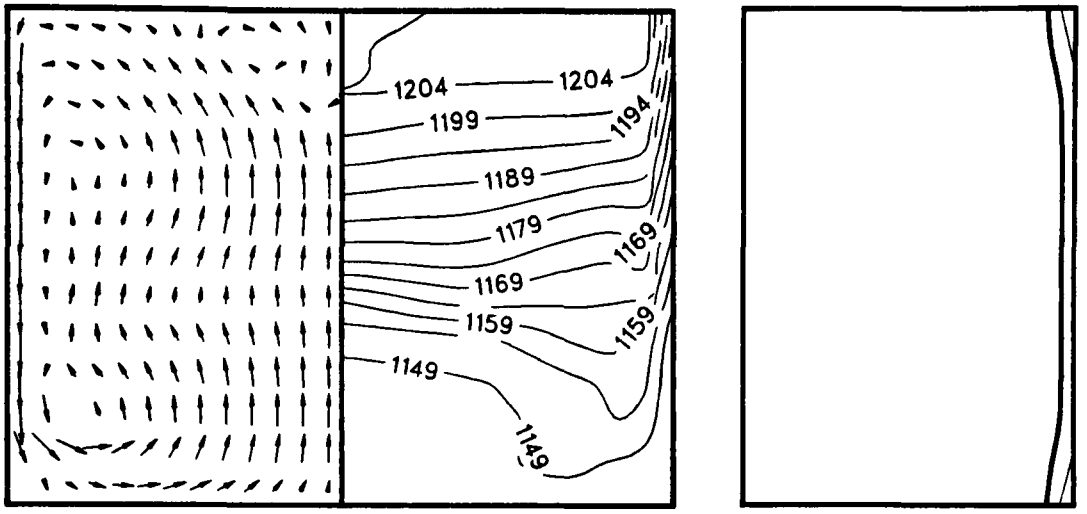

Figure 5.19 Velocity and temperature distributions during (a) combined heat transfer, and (b) conduction heat transfer. Time = 20 s, maximum velocity = 3.8 cm/s, $Gr = 4.8 \times 10^6$.

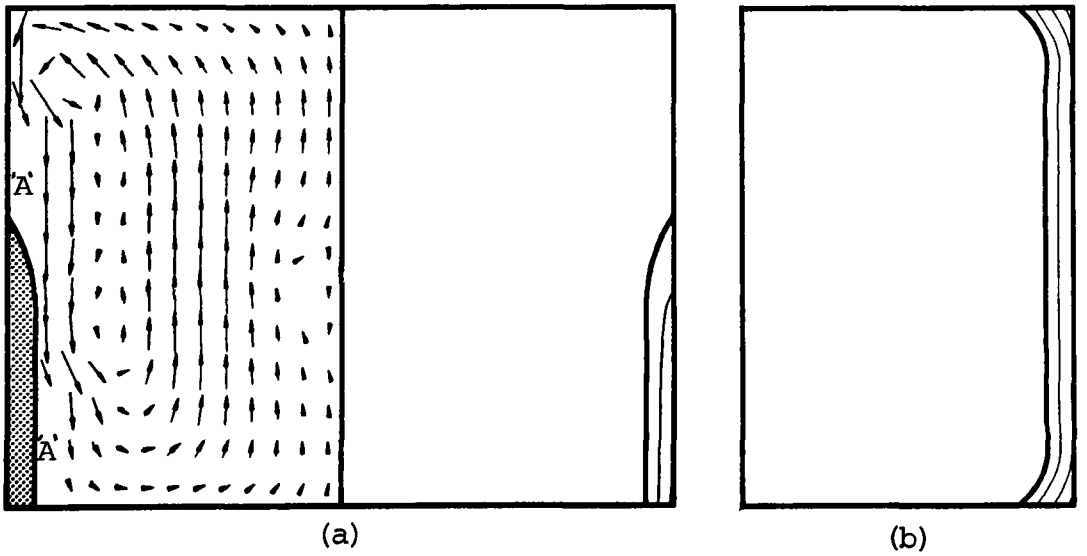

Figure 5.20 Velocity and temperature distributions during (a) combined heat transfer, and (b) conduction heat transfer. Time = 40 s, maximum velocity = 1.3 cm/s, $Gr = 1.2 \times 10^6$.

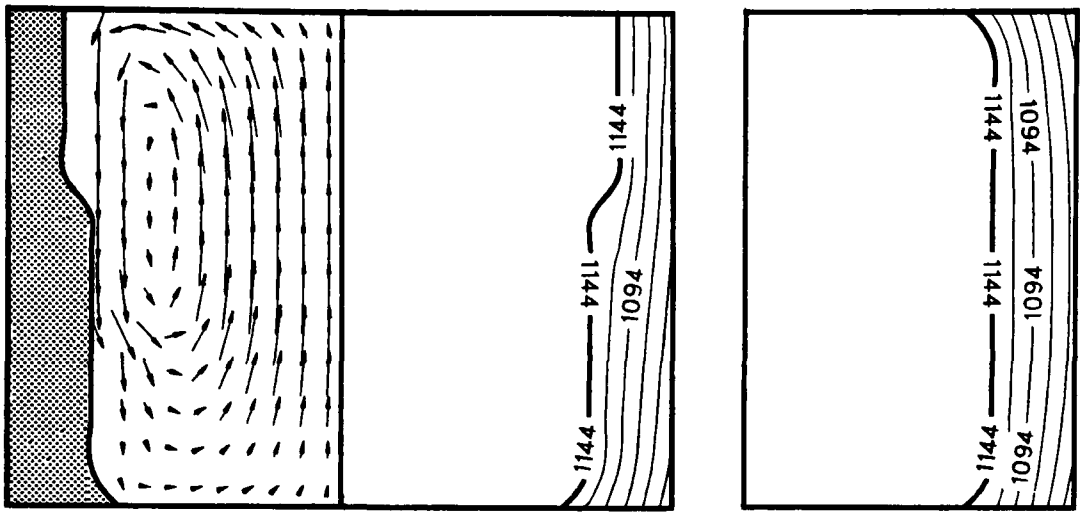

Figure 5.21 Velocity and temperature distributions during (a) combined heat transfer, and (b) conduction heat transfer. Time = 80 s, maximum velocity = 4.4 mm/s, $Gr = 7 \times 10^4$.

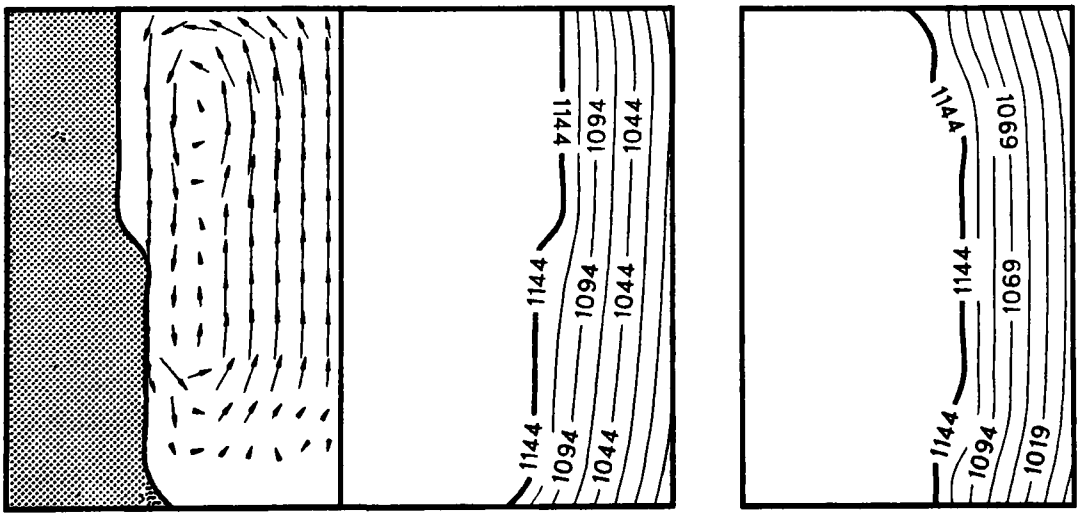

Figure 5.22 Velocity and temperature distributions during (a) combined heat transfer, and (b) conduction heat transfer. Time = 120 s, maximum velocity = 2 mm/s, $Gr = 1 \times 10^4$.

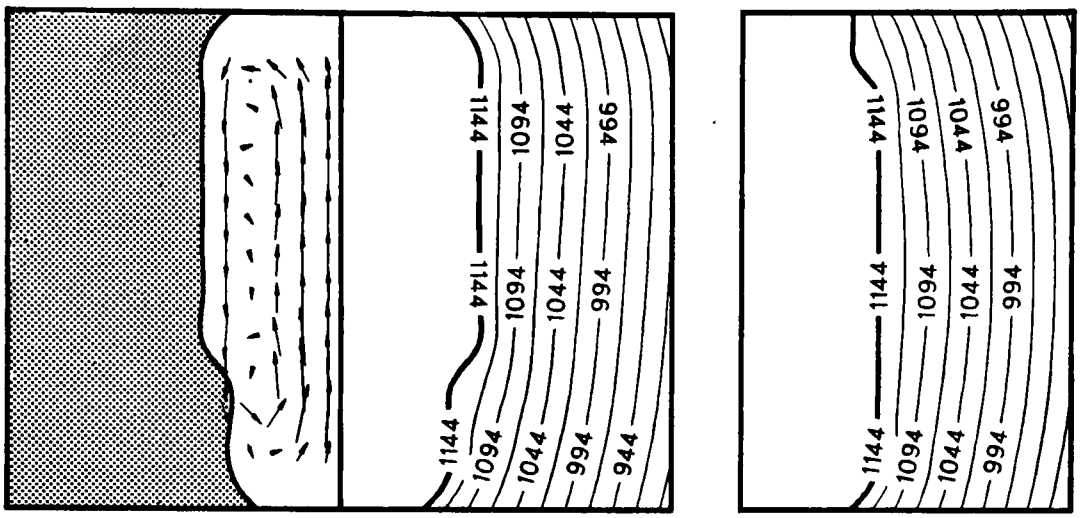

Figure 5.23 Velocity and temperature distributions during (a) combined heat transfer, and (b) conduction heat transfer. Time = 180 s, maximum velocity = 1.5 mm/s, $Gr = 3 \times 10^3$.

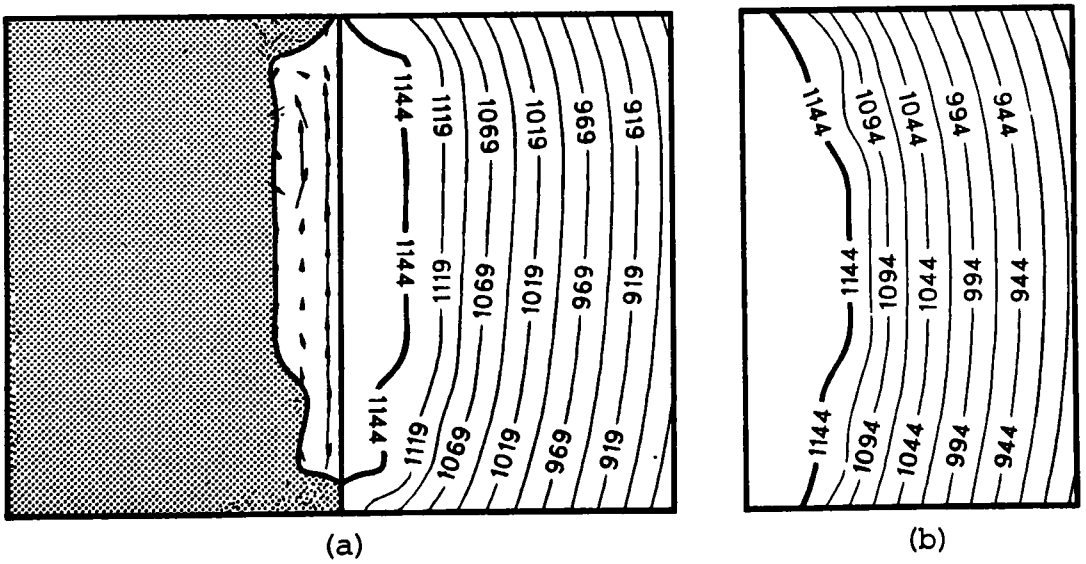

Figure 5.24 Velocity and temperature distributions during (a) combined heat transfer, and (b) conduction heat transfer. Time = 220 s, maximum velocity = 2.3 mm/s, $Gr = 7 \times 10^2$.

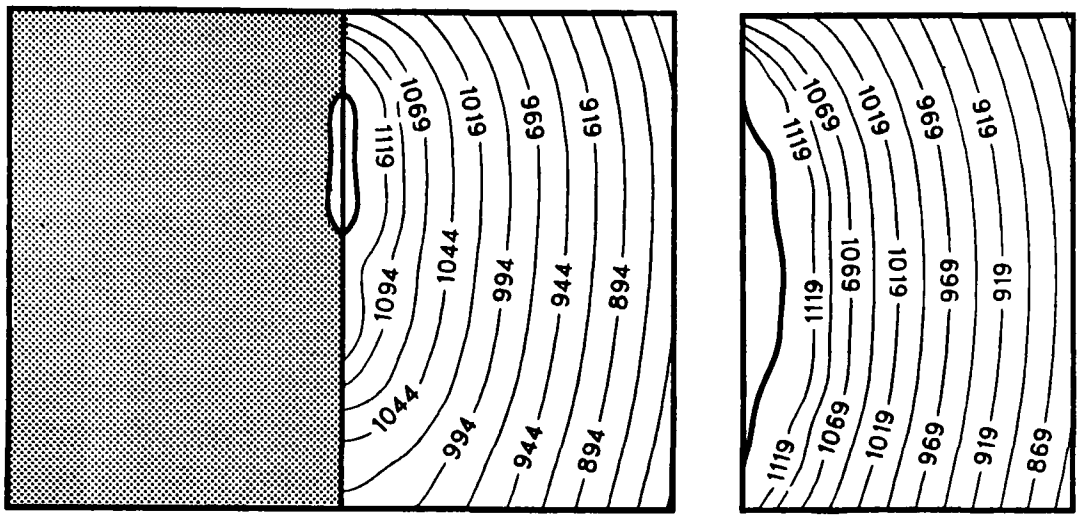

Figure 5.25 Velocity and temperature distributions during (a) combined heat transfer, and (b) conduction heat transfer. Time = 260 *s*

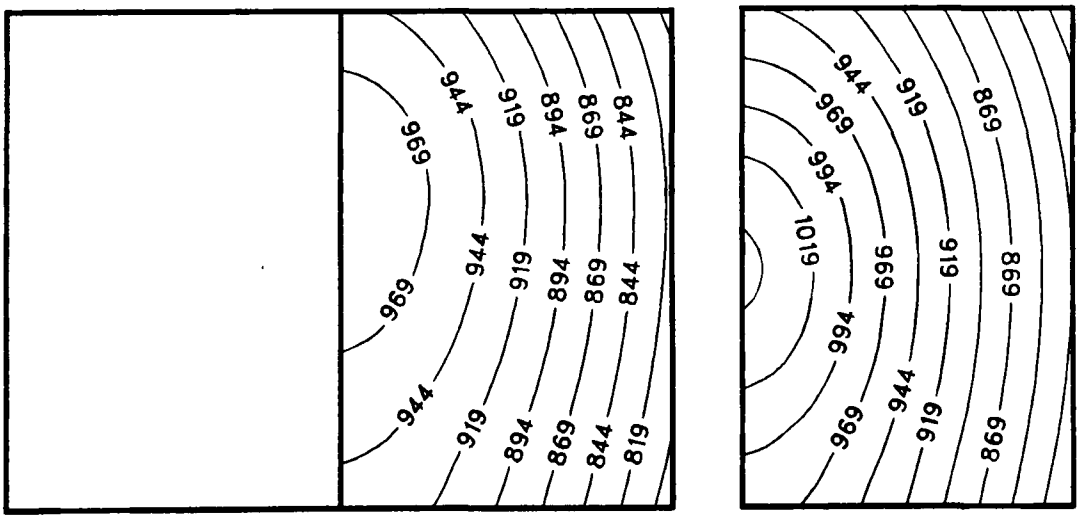

Figure 5.26 Velocity and temperature distributions during (a) combined heat transfer, and (b) conduction heat transfer. Time = 300 *s*

heat transfer solutions are almost identical in the mold, with the exception of the very early stages for the middle and top locations (Figures 5.29 and 5.31) where the differences because of the filling time are apparent.

Figures 5.28, 5.30 and 5.32 illustrate the temperatures in the casting near the mold wall at the bottom (2), mid-height (4) and top (6) thermocouple locations respectively. It can be seen that the computed cooling rate is somewhat faster than experimentally observed, especially at the bottom location (Figure 5.28). A better agreement could have been obtained by varying the interface heat transfer with time to take the casting shrinkage and mold expansion into account, however, a detailed study of the interface heat transfer is not within the scope of this work. It can be seen (Figure 5.32) that initially higher temperatures are computed using combined heat transfer (both conduction and convection in contrast with conduction alone), as hotter fluid is convected from the central region of the casting towards the upper peripheral region.

Figure 5.33 shows the temperature in the bottom central region of the casting. Very good agreement is obtained between the convection results and the experimental data, both for the initial stages as well as the solidification time. If only conduction is computed, the initial temperatures and the solidification time are over–predicted because the convection of the cooler liquid from the solidifying side walls to the bottom is neglected. The convection causes lower temperatures in the bottom region, resulting in faster cooling and solidification than predicted by conduction alone. The experimental cooling rate is slower after solidification, possibly due to shrinkage of the solidified casting.

Figure 5.34 shows the temperature variation in the central region at the mid-height of the casting (location (8)). The combined heat transfer calculations are more accurate in this case as well, and a similar reasoning as for location (7) in the previous paragraph applies. Figures 5.35 and 5.36 show the temperature variation at the top (9) and middle (10) locations, respectively. It can be seen that

excellent agreement is obtained between the combined heat transfer results and the experimental data.

In summary it appears that there *is* significant convection during the solidification process. The recirculatory flow pattern transfers heat from the bottom central region (7) to the upper peripheral regions (6). The conduction calculations neglect this heat transfer and therefore they overestimate the temperatures at (7) and underestimate the temperatures at (6). For the present geometry the conduction calculations provide a fair approximation of the heat transfer, and are considerably more economical and simpler than the combined heat transfer computations. In the present study a typical convection simulation required 410 CPU seconds and a conduction simulation required only 60 CPU seconds on a Cray X-MP computer. It should be noted that an accurate computation of convection is necessary for the calculation of segregation and a detailed study of the heat transfer. It should also be noted that the importance of convection heat transfer can vary with the geometry of the casting.

Interface heat transfer

Figure 5.37 shows the variation of the interface heat transfer coefficient with time. The interface heat transfer model in the present work includes spot conduction, radiation and conduction through the air in the gap into account. The values reported by Sully [118] for vertically cast $0.02\,m$ thick grey iron plates and Nishida and Matsubara [80] for $0.05\,m$ diameter aluminum cylinders are also shown. It can be seen that the computed values are very close to the experimental results reported in the literature. It is interesting to note the minor fluctuations in the interface heat transfer values. There fluctuations are due to the temperature oscillations taking place when the solidus front passes through the cell layers close to the mold walls. Such temperature fluctuations can occur when weak methods [87] are used to determine latent heat release of isothermally solidifying materials.

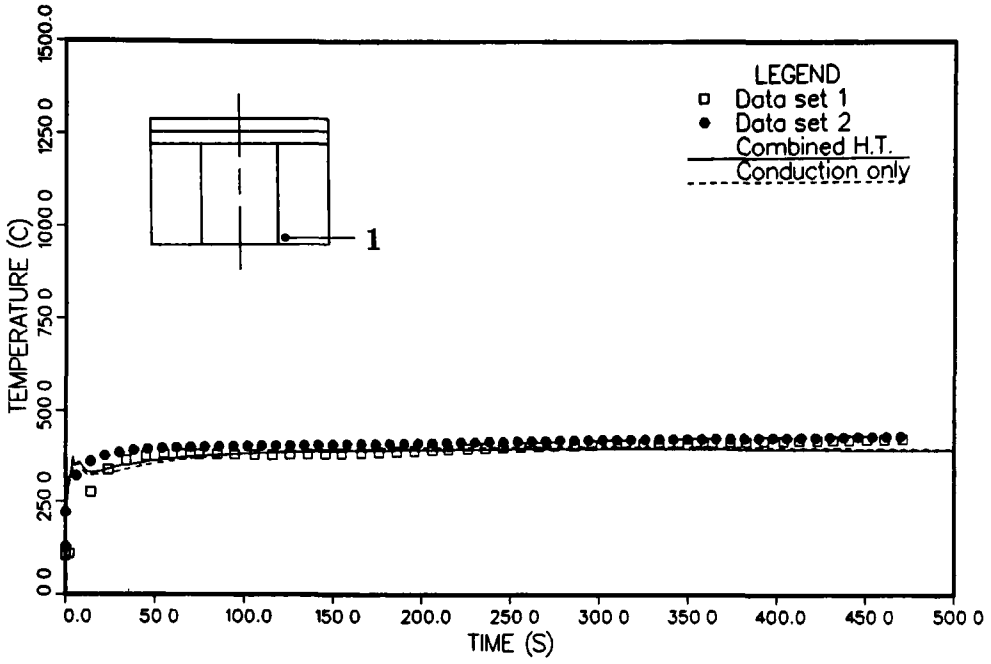

Figure 5.27 Temperature variation with time at thermocouple location (1)

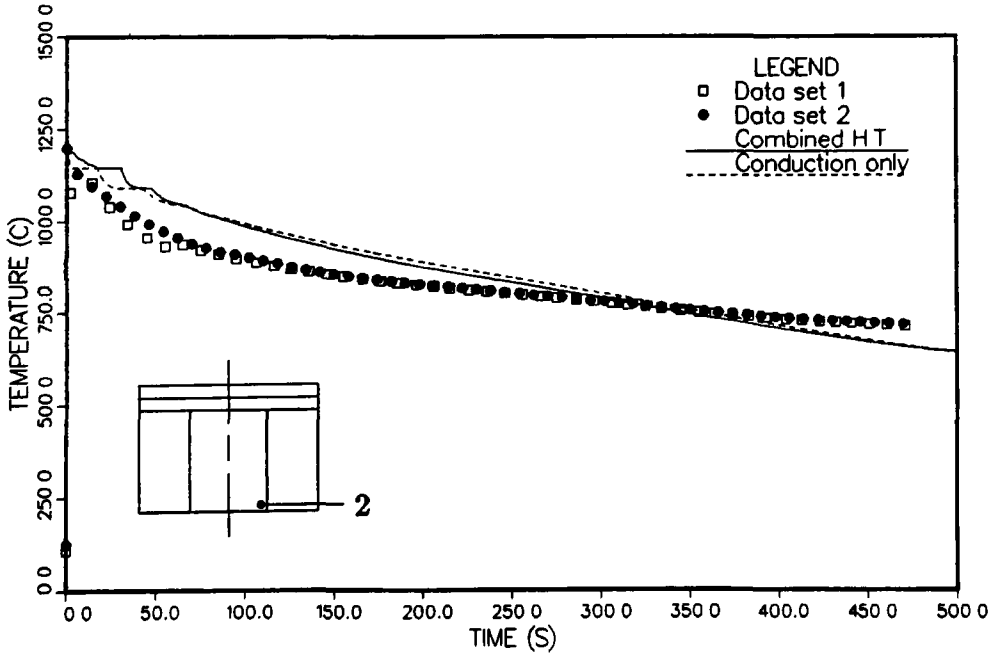

Figure 5.28 Temperature variation with time at thermocouple location (2)

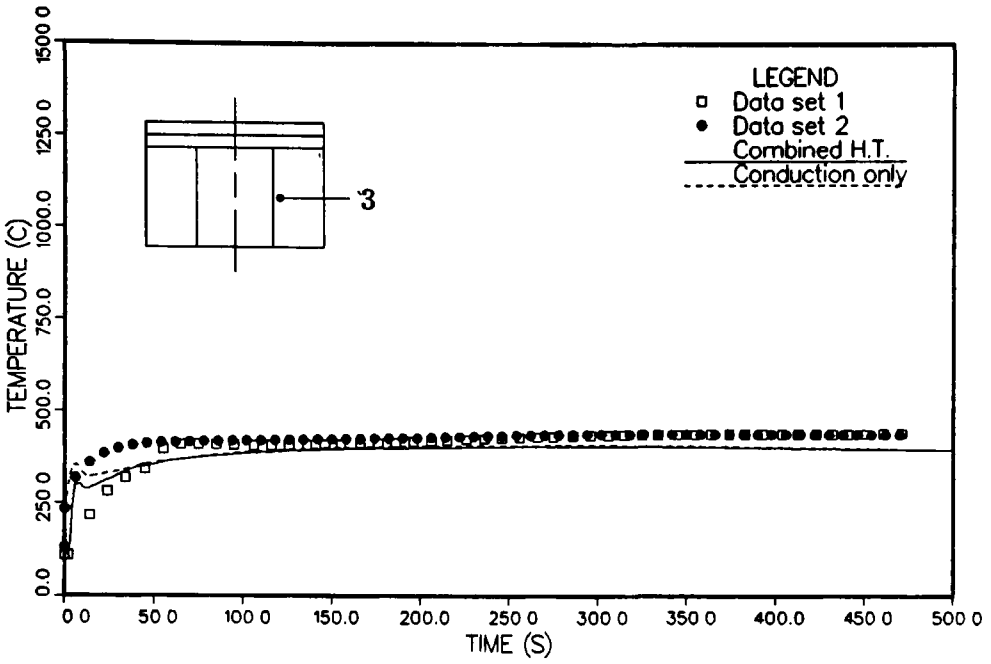

Figure 5.29 Temperature variation with time at thermocouple location (3)

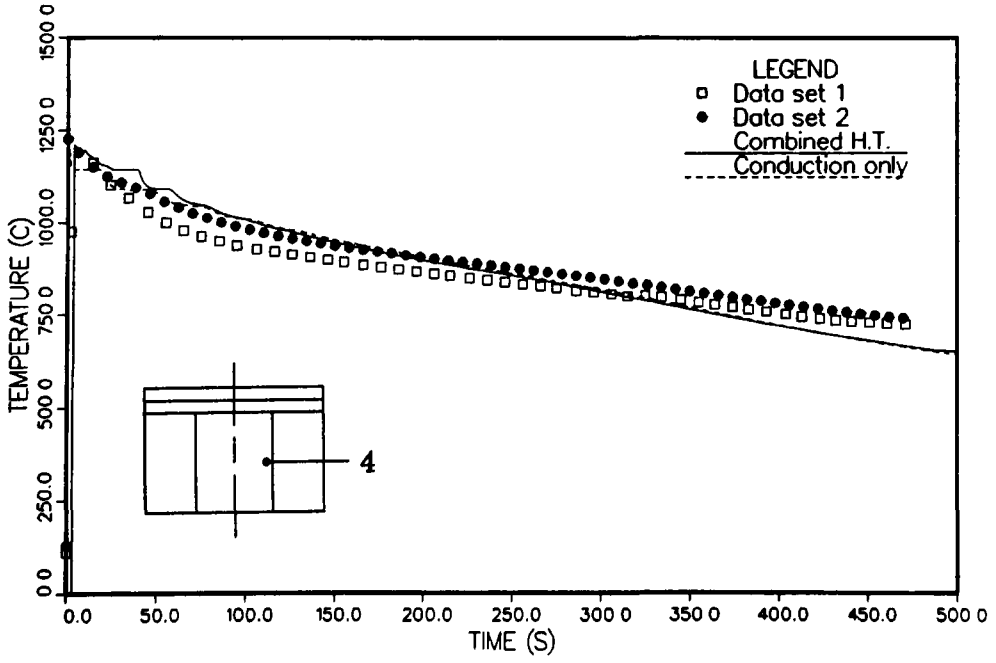

Figure 5.30 Temperature variation with time at thermocouple location (4)

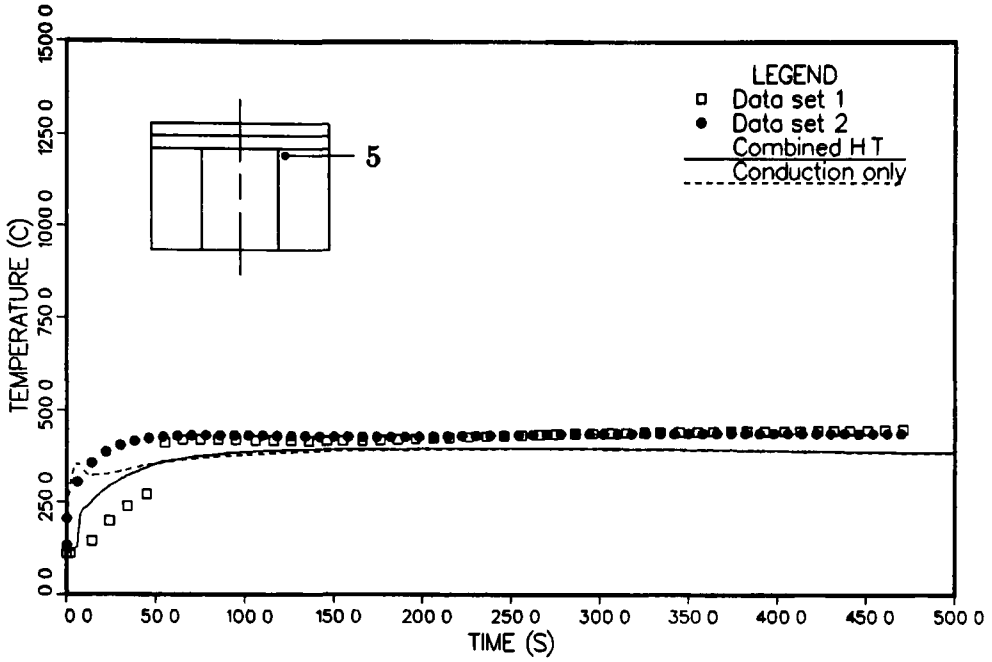

Figure 5.31 Temperature variation with time at thermocouple location (5)

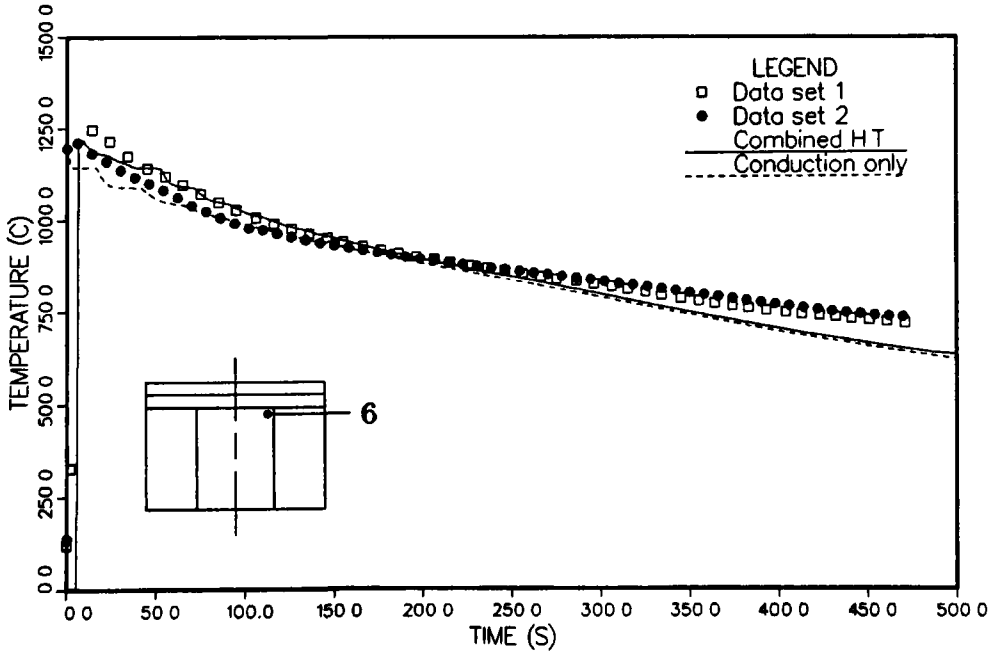

Figure 5.32 Temperature variation with time at thermocouple location (6)

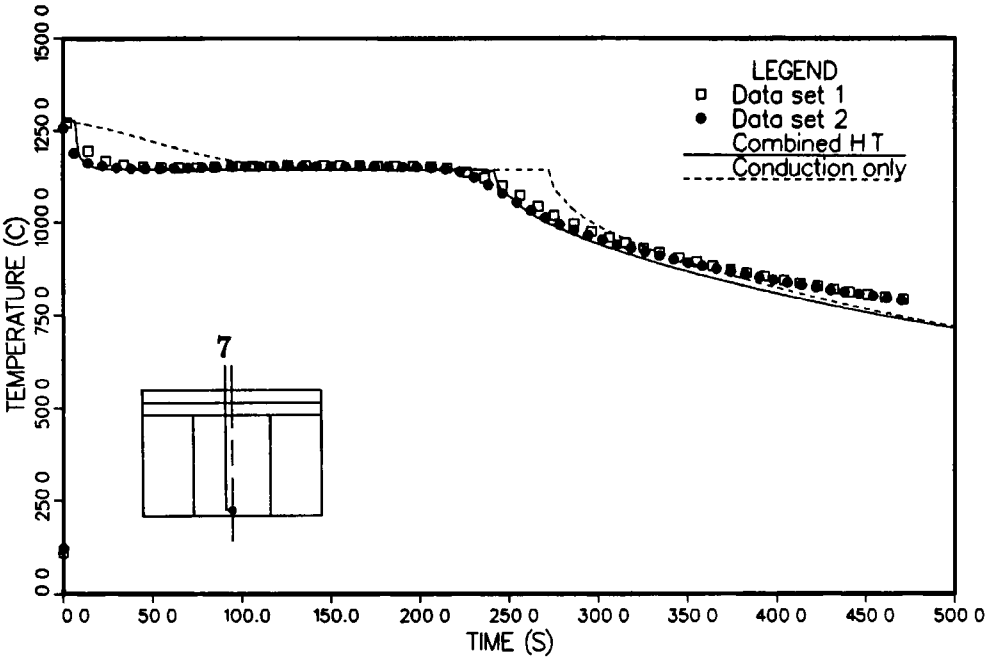

Figure 5.33 Temperature variation with time at thermocouple location (7)

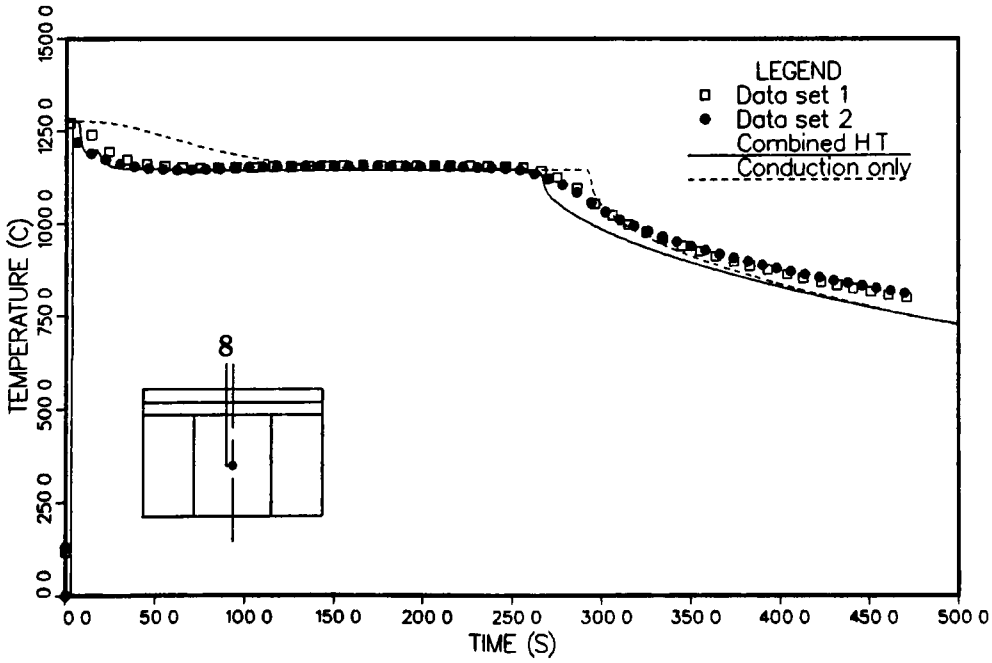

Figure 5.34 Temperature variation with time at thermocouple location (8)

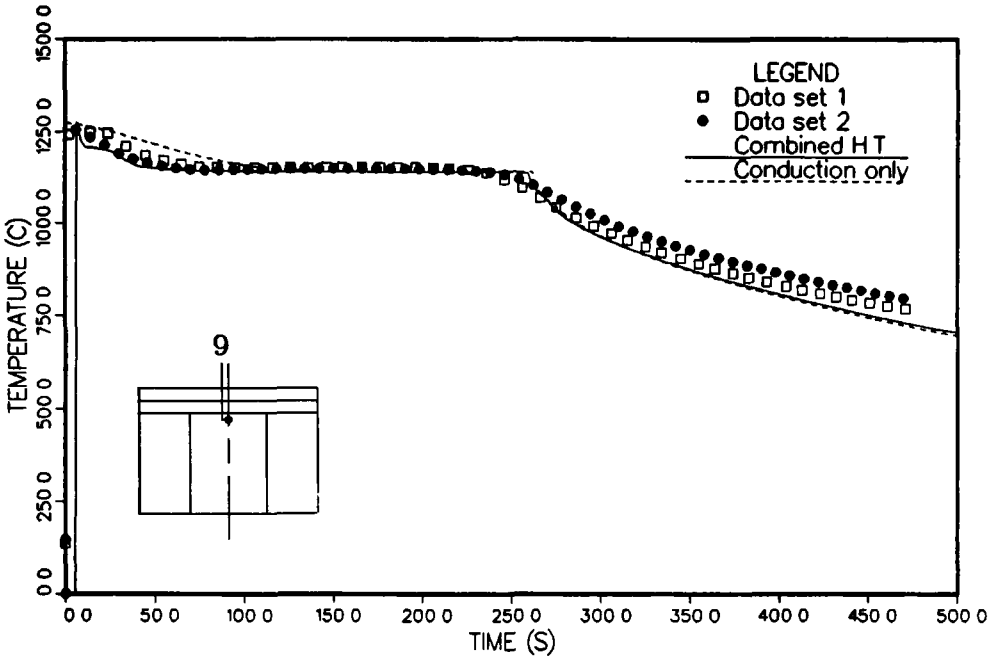

Figure 5.35 Temperature variation with time at thermocouple location (9)

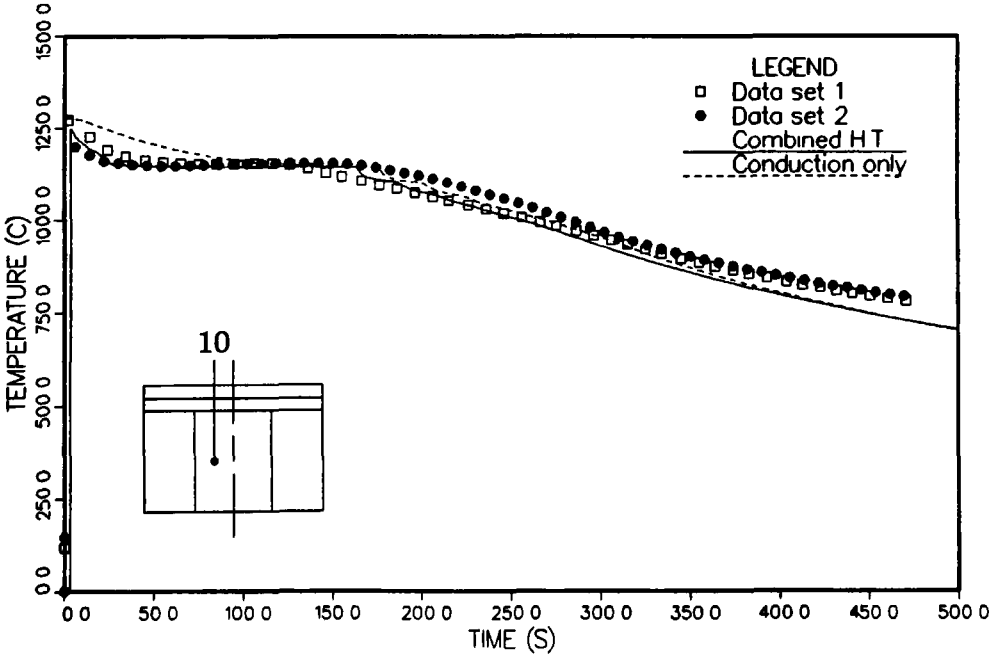

Figure 5.36 Temperature variation with time at thermocouple location (10)

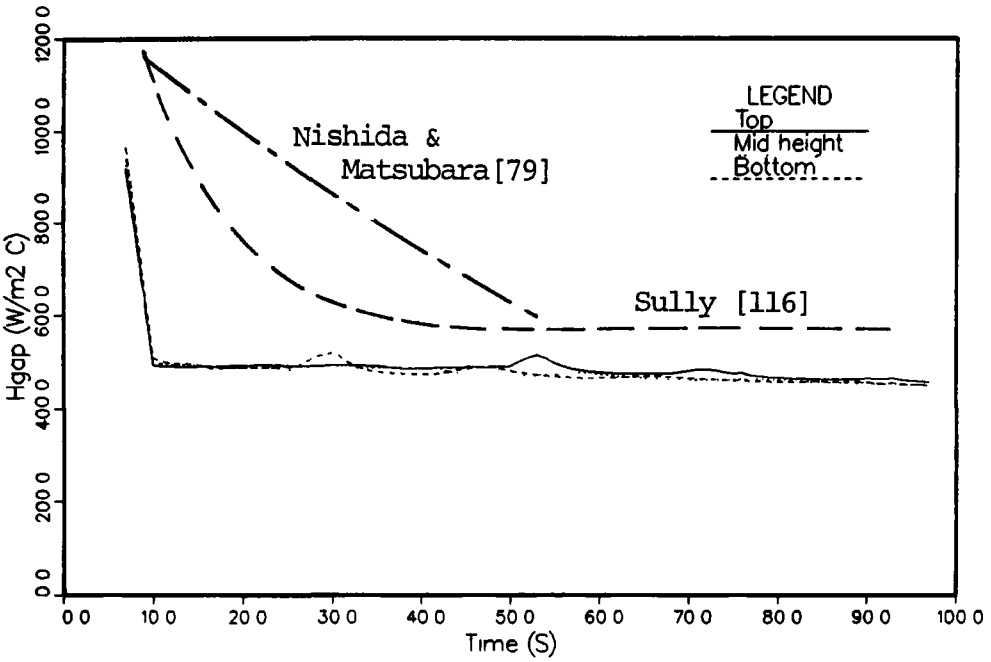

Figure 5.37 Variation of the interface heat transfer coefficient with time

Effects of computational parameters

Computations were carried out to determine the effect of different parameters; namely, mesh size, time step and the time t_t, at which the turbulence modelling is terminated.

Figures 5.38–5.41 show the typical temperature variation at four different locations for five different test cases:

(a) Base test case, (coarse mesh in Figure 5.2(b), $t_t = 10\,s$, time step = 1 s).

(b) Mesh size test, (fine mesh in Figure 5.2(c), $t_t = 10\,s$, time step = 0.5 s).

(c) Time step test, (as in (a) but time step = 0.5 s).

(d) Termination of turbulence test, (as in (a) but $t_t = 7\,s$).

(e) Termination of turbulence test, (as in (a) but $t_t = 13\,s$).

The results indicate that the temperature distributions are only marginally dependant on the mesh size and time step and essentially independent of t_t.

Figure 5.42 shows the temperature distribution for the fine mesh case at $80\,s$. A comparison with Figure 5.21 shows that the velocity field in both cases are very similar and the maximum velocity values are within 10 %. The liquid metal solidifies as it flows down near the solidus interface, therefore, the solidus front is expected to be inclined from the vertical. The solidus shape predicted using the two mesh sizes are also very similar. In both cases the inclined interface is being simulated in a stepwise manner; in the coarse mesh case there is one step in the interface and in the fine mesh case there are two steps. The computations using the fine mesh case are considerably more expensive however. The computations require 410 CPU seconds using the coarse mesh and 1340 CPU seconds using the fine mesh with a Cray X-MP computer.

A comparison of Figures 5.21 and 5.43 shows the effect of time step on the temperature distribution, solidus front shape and velocity field. It can be seen that the temperature distribution is almost identical and the solidus front shapes are very similar. The convective velocity fields are also very similar, however the maximum velocity obtained using the small time step is 15 % higher.

A comparison of Figures 5.19, 5.44 and 5.45 show the effect of the time t_t, at which the computation of turbulence is terminated. The turbulence computation is terminated immediately after filling is completed ($t_t = 7\,s$) in the results reported in Figure 5.44, 3 seconds after filling ($t_t = 10\,s$) in Figure 5.19, and 6 seconds after filling ($t_t = 13\,s$) in Figure 5.45. The velocity fields are very similar, especially for $t_t = 7\,s$ and $t_t = 10\,s$. The small vortex at the top near the symmetry axis is not present if $t_t = 13\,s$ because of the effects of the higher turbulent effective viscosity. The maximum velocity values for the three cases are within 9 %. It can be seen that the temperature fields are very similar for the three cases, suggesting that the differences in the total heat transfer are not significant. The differences in

the velocity and temperature fields become almost insignificant 80 seconds into the process, and the maximum velocity values are within 3 %.

In summary, it has been shown in this section that the computed results are relatively insensitive to computational parameters such as time step, mesh size, and the time at which the computation of turbulence is terminated.

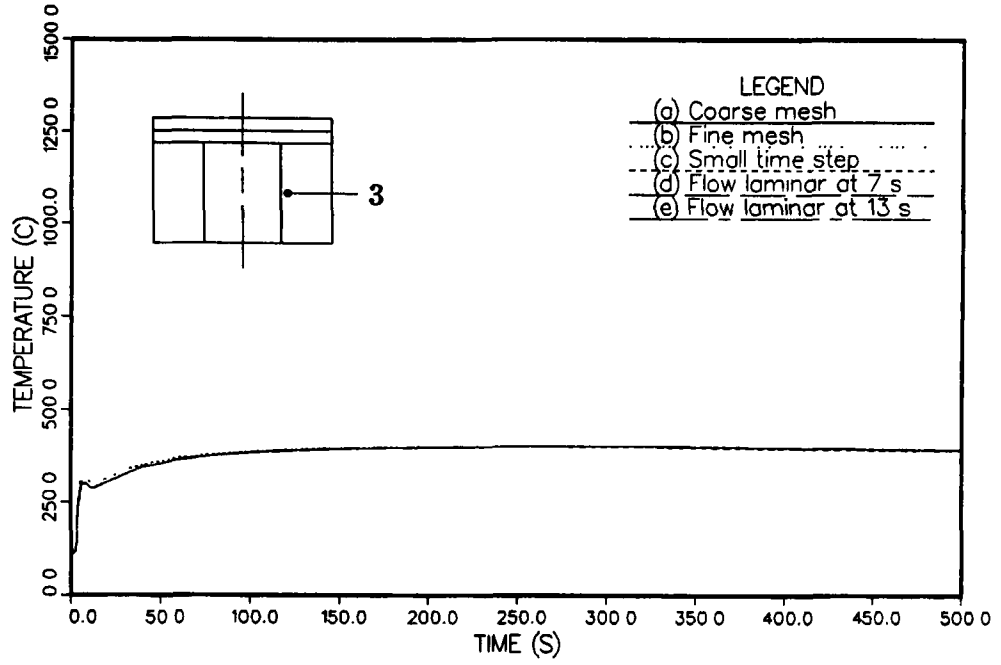

Figure 5.38 Parametric effects on the temperature variation with time, location (3)

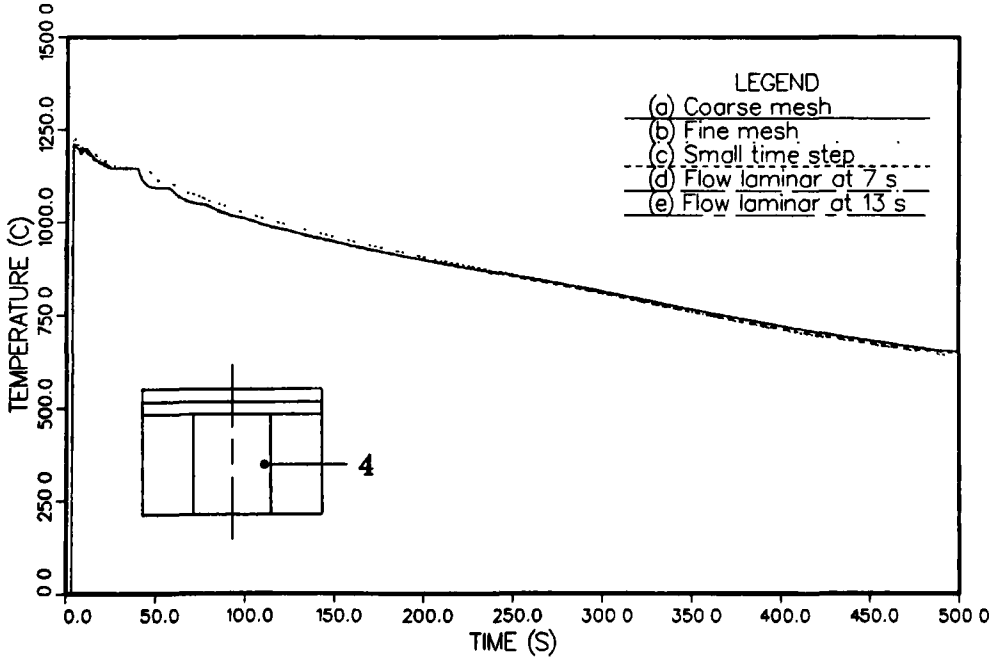

Figure 5.39 Parametric effects on the temperature variation with time, location (4)

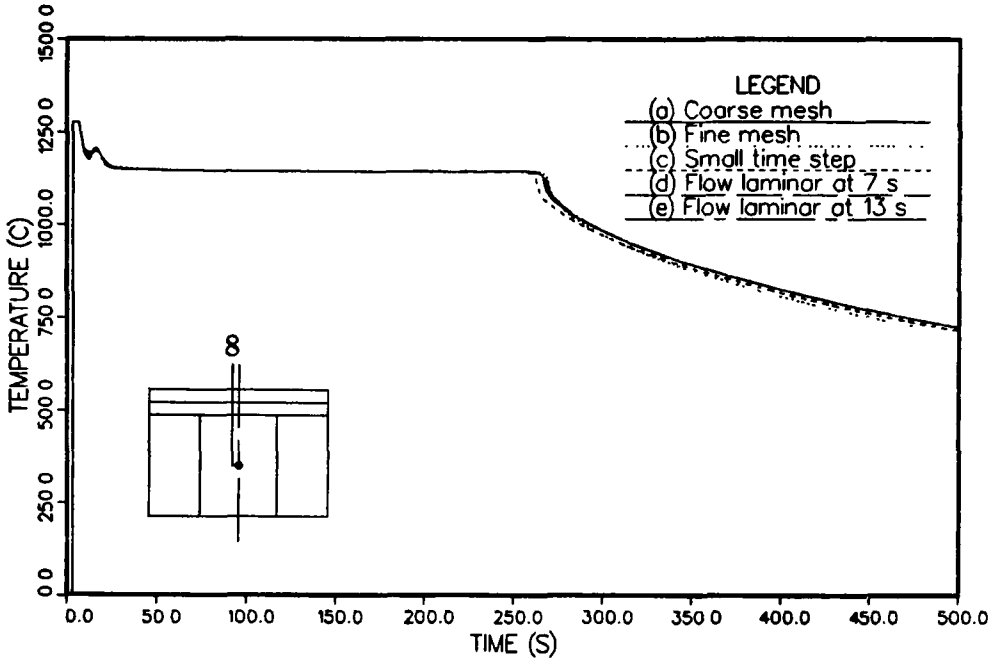

Figure 5.40 Parametric effects on the temperature variation with time, location (8)

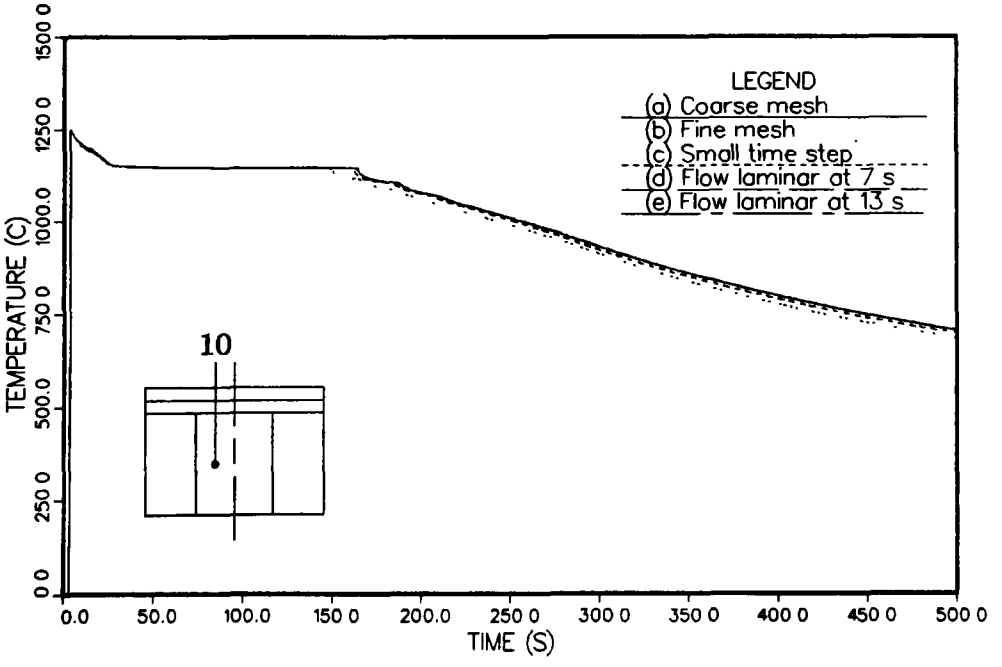

Figure 5.41 Parametric effects on the temperature variation with time, location (10)

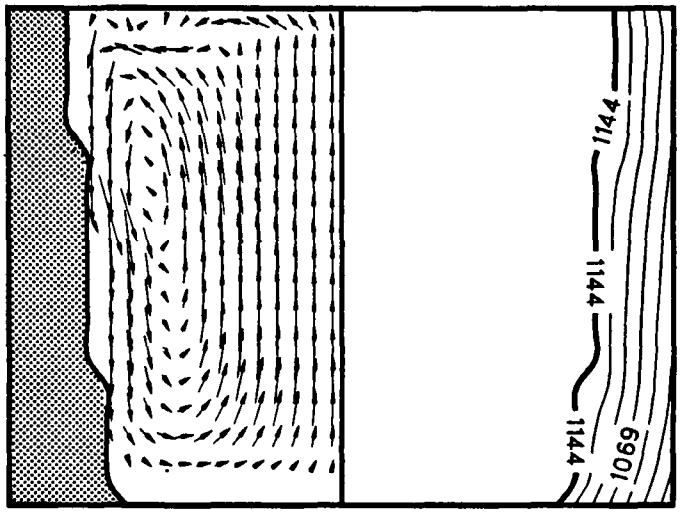

Figure 5.42 Velocity and temperature fields at time = 80 s. Maximum velocity = 4.8 mm/s. Fine mesh case.

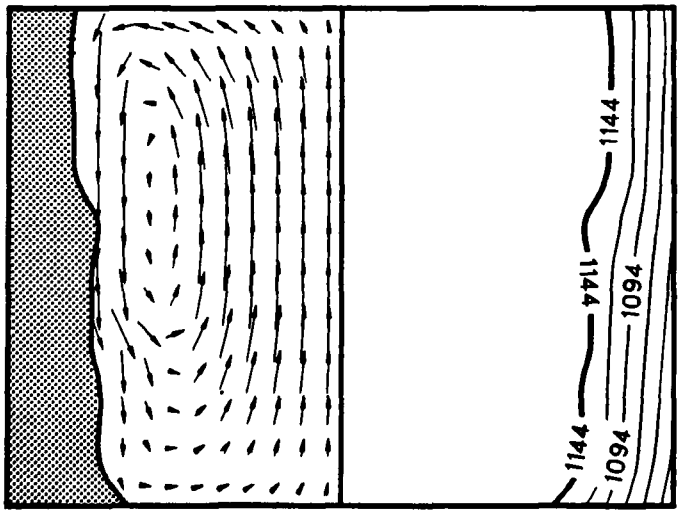

Figure 5.43 Velocity and temperature fields at time = 80 s. Maximum velocity = 5.1 mm/s. Small time step case.

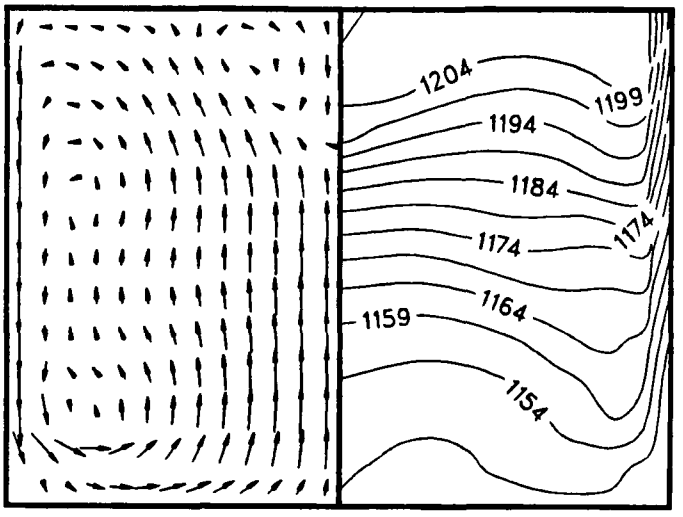

Figure 5.44 Velocity and temperature fields at time = 20 s. Maximum velocity = 4.1 mm/s. $t_t = 7\,s$

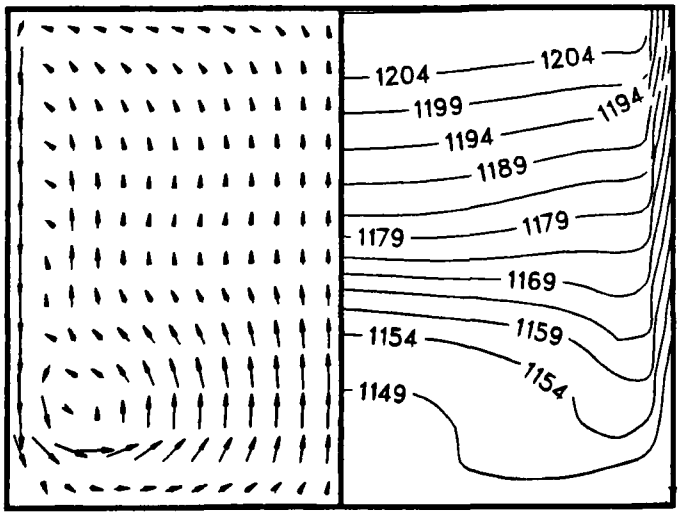

Figure 5.45 Velocity and temperature fields at time = 20 s. Maximum velocity = 3.8 mm/s. $t_t = 13\,s$

Chapter 6

SUMMARY, CONCLUSIONS AND RECOMMENDATIONS

6.1 Summary

Mathematical modelling and experimental work has been undertaken to investigate heat transfer and liquid metal flow during permanent mold casting processes. The work has been carried out in three phases, as described in the following:

In the first phase heat transfer during solidification of a cast iron plate has been mathematically and experimentally investigated. An Alternating Direction Implicit finite difference technique has been used for the mathematical modelling. Phase change has been simulated and a finite pour time has been allowed for. Experimental work has been carried out to obtain the temperature distribution in the casting and mold. Calculated temperatures have been compared against experimental data and satisfactory agreement has been obtained. The importance of liquid metal convection as well as keying effects at a side gate or a projecting

section (holding the casting against a mold cavity surface and affecting the interface heat transfer) have been demonstrated. It has been concluded that the discrepancies between the computed and experimentally measured temperatures are due to a combination of simplifying assumptions related to the interface treatment and liquid metal convection. Thermal stresses in the mold have been computed using the finite element method. The implications of the temperature field on the thermal stress distribution and mold life have been discussed [3,99,100].

In the second phase, new treatments of computational domains which change spatially with time, and which model flows with free surfaces using the Finite Volume Method have been developed. This work has been aimed at modelling flow and heat transfer during the filling of molds with liquid metal. Experimental work has been carried out to investigate the velocity fields and free surface profiles during the filling of a cylindrical container with water. The velocity fields have been obtained by a photographic flow visualization technique. Comparison of the experimental and predicted free surface profiles and velocity fields have yielded very good agreement [97]. The free surface treatment has been demonstrated to perform better than the widely used free slip condition. The free surface treatment developed in this study has also been applied [96] to the study of gas–stirred liquid reactors and shown to be very useful. The treatment has also proven to be useful [109,117] in modelling external flows with a zero pressure gradient.

In the third phase [1,97,98] the casting of a cylindrical grey iron ingot has been mathematically and experimentally investigated. Computational work has been carried out to simulate the liquid metal flow and heat transfer during the pouring and solidification of a cylindrical grey iron ingot. The mesh transformation and free surface treatment techniques developed in phase two have been used to simulate the liquid metal flow during the filling of the mold. The mathematical models developed in this phase have also been verified against experimental data for free convection of Pb–Sn alloys. A new model has been developed to treat liquid metal flow in the mushy region. The model is based on experimental data and takes the change in

morphology of the mushy region into account. Experimental work has been carried out to obtain temperature distributions during the casting of a cylindrical ingot. A comparison of the computed and experimental temperature fields in the casting and mold has shown excellent agreement. The computer simulation provides detailed information about the temperature field, solidus front shape and velocity fields during pouring and solidification. The significance of forced and natural convection in heat transfer during casting processes has been shown. Mesh size and time step studies have been carried out to assess the influence of these parameters on the results.

6.2 Contributions

1. A mathematical model of the conduction heat transfer during the complete mold casting system has been developed. Some aspects, namely gating location and finite pouring time, have not been addressed previously in the open literature and have been given special attention. The post iterative method for latent heat release has been extended for binary alloys. Thermal stresses in the mold have been determined and their effect on mold life has been analyzed. The effects of the initial mold temperature on the thermal stresses has been demonstrated. The results of the model have been compared with experimental data.

2. A complete casting simulation model, including all significant heat transfer mechanisms has been developed. Novel treatments incorporated in the model include:

    - A new mesh transformation technique applied with a free surface implementation using the Finite Volume Method. The free surface implementation predicts the surface shape and applies the necessary boundary conditions.

- New equations to account for latent heat release using a source based method.
- A new formulation to simulate flow through the solid liquid mushy zone.

Experimental work has been carried out in support of the mathematical modelling. The computed results have been compared with experimental data obtained from water model and casting solidification tests.

6.3 Engineering benefits

The performance of the mathematical models has been demonstrated to be satisfactory. These models can be therefore now used as part of a series of CAD packages for casting design. The conduction models developed in phase one provide a reasonably accurate simulation of the heat flow at a relatively low cost. The combined heat transfer model developed in phase three provides a complex and accurate simulation of the heat transfer at a somewhat higher cost. This is required for process optimization and for modelling of the segregation during solidification. The free surface treatment developed in phase two can be applied to a wider class of problems. The method has been used to study flow in the region of a spout generated by injecting gas vertically upwards in a pool of liquid. The free slip condition provides an inadequate treatment of the region of the spout. This work is relevant to the study of gas stirring in liquid vessels.

6.4 Conclusions

The following conclusions can be drawn from the mathematical and experimental work:

1. The temperature distributions in the liquid metal during and after the mold filling are strongly affected by the velocity field.
2. Liquid metal convection during solidification affects the solidus front shape, temperature distributions and heat transfer in the casting.
3. The location where solidification takes place last depends on the liquid metal convection during solidification.
4. Conduction based models provide a satisfactory approximation of the temperature distribution in the molds for the test cases in this study.
5. The mold casting interface constitutes a significant resistance to the heat flow in permanent molding. Keying effects at a side gate or a projecting section significantly affect the interface heat transfer.
6. The finite pouring time causes an asymmetry in the thermal stress distribution in the mold.

6.5 Recommendations

1. The heat transfer mechanisms at the mold casting interface are very complex. Further research in this area is necessary to improve the performance of the mathematical models.
2. The structure of the mushy region is difficult to define qualitatively, as it is a function of many different parameters, for example material properties,

cooling rate, alloying elements and innoculants. Further experimental work is required to provide the necessary data for the improvement of the mathematical treatment of this region.

3. Liquid metal properties are not well defined, especially near the melting point. Experimental work is required to obtain more property data to better simulate the liquid metal.

4. Further refinement of the mathematical models can be carried out by also simulating segregation and coupling it to the energy equation calculations including the latent heat treatment.

5. The liquid metal density variation due to temperature and phase change can be accounted for to simulate shrinkage.

6. The mathematical models developed in this study can be extended to other processes, for example, continuous casting of alloys.

7. The models can also be extended to the processing of non–metallic materials (for example plastic extrusion) by accounting for the non–Newtonian behavior.

References

[1] Z. Abdullah, M. Salcudean, 'Computation of Casting Solidification in Presence of Natural Convection', *Numerical Methods in Thermal Problems R. W. Lewis, K. Morgan, W. G. Habashi, eds.*, **5**, Part 1, Proceedings of the Fifth International Conference held in Montreal, Canada, June 29–July 3, (1987).

[2] Z. Abdullah, 'Mathematical Modelling of Casting Processes', Internal Report, Department of Mechanical Engineering, University of Ottawa, (July 18, 1986).

[3] Z. Abdullah, M. E. Salcudean, K. G. Davis, 'Modelling the Solididification of Cast Iron in Permanent Molds', *Symposium on Computer Modelling of Fabrication Processes and Constitutive Behaviour of Metals*, Organized by CANMET/PMRL, Energy, Mines and Resources, and AMCA Int. Ltd., Ottawa, Canada, (May 15–16, 1986).

[4] S. Abis, 'Numerical Simulation of Solidification in an Aluminum Casting', *Metallurgical Transactions B*, **17**, 209-216, (March 1986).

[5] D. A. Anderson, J. C. Tannehill, R. H. Pletcher, *Computational Fluid Mechanics* ,McGraw Hill Book Co., (1984).

[6] H. T. Angus, 'Cast Iron: Physical and Engineering Properties', *2nd Ed.*, Butterworths, London, (1976).

[7] S. Asai, J. Szekely, 'Turbulent Flow and its Effects in Continuous Casting', *Ironmaking and Steelmaking*, **3**, (1975).

[8] P. K. Bannerjee, R. Butterfield, ***Boundary Element Methods in Engineering Science***, McGraw Hill, Maidenhead, U.K., (1981).

[9] G. Birkhoff, E. H. Zarantonello, ***Jets, Wakes, and Cavities***, Academic Press Inc., New York, (1957).

[10] E. A. Boucheron, R. N. Smith, 'Application of the Enthalpy Method to Multi-dimensional Solidification Problems with Convection', ***Paper 86-WA/HT-42, Presented at the Winter Annual Meeting of the ASME***, Anaheim, California, (Dec 7-12, 1986).

[11] C. A. Brebbia, ***The Boundary Element Method for Engineers***, Pentech Press, London, (1978).

[12] H. D. Brody, D. Apelian, ***eds.***, 'Modeling of Casting and Welding Processes', ***Proceedings of a symposium sponsered by the solidification committee of the Metallurgical Society of AIME, the Process Modeling Activity of American Society for Metals and the Engineering Foundation***, Rindge, New Hampshire, (August 3–8, 1980).

[13] H. D. Brody, R. A. Stoehr, 'Computer Simulation of Heat Flow in Casting', ***Journal of Metals***, 20-27, (September 1980).

[14] R. Chan, 'A Genralized Arbitrary Lagrangian Eularian Method for Incompressible Flows with Sharp Interfaces', ***Journ. of Computational Physics***, **17**, 311–331, (1975).

[15] K. C. Cheng, V. J. Lunardini, N. Seki, ***eds.***, ***Proceedings of the 1987 International Symposium on Cold Regions Heat Transfer***, University of Alberta, Edmonton, Alberta, Published by the ASME, (June 4–6, 1987).

[16] T. W. Clyne, 'The Use of Heat Flow Modelling to Explore Solidification Phenomena', ***Metallurgical Transactions B***, **13**, 471-478, (September 1982).

[17] G. S. Cole, G. F. Bolling, 'Importance of Fluid Flow Motion During Ingot Solidification', *A. F. S. Transactions*, **90**, (1982).

[18] R. D. Cook, *Concepts and Applications of Finite Element Analysis*, Wiley, (1981).

[19] J. Crank, P. Nicolson, 'A Practical Method for Numerical Evaluation of Partial Differential Equations of the Heat Conduction Type', *Proc. Cambridge Philos. Soc.* **43**, 50–67, (1947).

[20] A. B. Crowley, 'Numerical Solution of Stefan Problems', *Int. Jour. Heat Mass Transfer*, **21**, 215-219, (1978).

[21] J. A. Dantzig, J. T. Berry, *eds.*, 'Modelling of Casting and Welding Processes, II', *Proceedings of the conference held at New England College, sponsored by the Engineering Foundation and the Metallurgy Division, National Bureau of Standards*, Henniker, New Hampshire, (July 31–August 5, 1983).

[22] V. L. Davies, 'Feeding Range Determination by Numerically Computed Heat Distribution', *AFS Cast Metals Research Journal*, 33-44, (June 1975).

[23] V. L. Davies, 'Heat transfer in gravity die castings', *British Foundrymen Journal*, **73**, (1980).

[24] K. G. Davis, CANMET/PMRL, Department of Energy, Mines and Resources, Government of Canada, Personal communications, (1985).

[25] P. V. Desai, J. T. Berry, C. Kim, 'Computer Simulation of Forced and Natural Convection During Filling of a Casting', *AFS Transactions*, **92**, (1984).

[26] P. V. Desai, C. Kim, 'Heat Losses in Runner Channels', *Proceedings of the Engineering Foundation Conference–Modelling of Casting and Welding Processes II*, The Metallurgical Society of the AIME, (1983).

[27] Doherty, , *Hot Pipe*, U. S. Geological Survey Computer Contribution No. 4, (1970).

[28] H. M. Domanus, Y. Y. Liu, W. T. Sha,'Fluid Flow and Heat Transfer Modeling for Castings', *Proceedings of the 1986 Engineering Foundation Conferences-Modelling and Control of Casting and Welding Processes II.*, The Metallurgical Society of AIME, (1986).

[29] G. M. Dusinberre, 'Numerical Methods for Transient Heat Flows', *Trans. ASME*, 67:703, (1945).

[30] W. R. Ellis, 'An Inventory of the Canadian Ferrous Foundry Capabilities'. Report produced by the Resource Industries Branch, Department of Industry, Trade and Commerce, Federal Government of Canada. Ottawa, Ontario. (1982).

[31] M. C. Flemings, *Solidification Processing*, McGraw Hill, New York, (1974).

[32] H. L. Frisch, R. Simha, 'The Viscosity of Colloidal Suspensions and Macromolecular Solutions', in *RHEOLOGY, Theory and Applications*, Edited by F. R. Eirich, Academic Press Inc, New York, (1956).

[33] J. P. Gabathuler, F. Weinberg, 'Fluid Flow in a Dendritic Array', *Proceedings of the 1983 Engineering Foundation Conference-Modelling of Casting and Welding Processes II*, Published by the Metallurgical Society of the AIME, (1983).

[34] J. P. Gabathuler, F. Weinberg, 'Fluid Flow into a Dendritic Array under Forced Convection', *Mettallurgical Transactions B*, 14B, 733–741, (December 1983).

[35] R. Guenigault, G. Roots, 'Effects of Natural Convection on the Inward Solidification of Spheres and Cylinders', *Int. Journ. Heat Mass Transf.*, 28, 6, 1229–1231, (1985).

[36] A. D. Gosman, F. J. K. Ideriah, 'TEACH 2E: A General Computer Program for Two Dimensional Turbulent,Recirculating Flows', *Report, Dept. of Mech. Engineering, Imperial College*, London, U. K., (1976).

[37] F. Harlow, A. Amsden, 'A Numerical Fluid Dynamics Calculation Method for All Flow Speeds', *Journ. of Computational Physics*, **8**, 197–213, (1971).

[38] F. H. Harlow, J. E. Welch, 'Numerical Calculation of Time Dependant Viscous Incompressible Flow', *Physics and Fluids*, **8**, (1965).

[39] C. Harrison, F. Weinberg, 'The Influence of Convection on Heat Transfer in Liquid Tin', *Met. Trans. B.*, **16B**, (June 1985).

[40] J. O. Hinze, *Turbulence*, McGraw Hill Book Co., (1975).

[41] C. W. Hirt, B. D. Nichols,'Volume of Fluid (VOF) Method for the Dynamics of Free Boundaries', *Journal of Computational Physics*, **39**, 201–205, (1981).

[42] C. W. Hirt, B. D. Nichols, 'Volume of Fluid (VOF) Method for the Dynamics of Free Boundaries', *Journal. of Computational Physics*, **39**, (1981).

[43] C. W. Hirt, B. D. Nichols, N. C.Romero, 'SOLA–A Numerical Solution Algorithm for Transient Fluid Flows', Los Alamos Scientific Laboratory Report, LA-5852, (1975).

[44] C. W. Hirt, J. P. Shannon, 'Free-Surface Stress Conditions for Incompressible-Flow Calculations',*Journal of Computational Physics*, **2**, 403–411, (1968).

[45] K. Ho, R. D. Pehlke, 'Mechanisms of Heat Transfer at a Metal-Mold Interface', *AFS Transactions*, **92**, 587–598, (1984).

[46] K. Ho, R. D. Pehlke, 'Transient Methods for Determination of Metal–Mold Interfacial Heat Transfer', *AFS Transactions*, **91**, 689–698, (1983).

[47] J. P. Holman, *Heat Transfer*, McGraw Hill, New York, (1976).

[48] C. P. Hong, T. Umeda, Y. Kimura, 'Numerical Models for Casting Solidification: Part II. Application of the Boundary Element Method to Solidification Problems', *Metallurgical Transactions B*, **15**, 101-107, (March 1984).

[49] C. P. Hong, T. Umeda, Y. Kimura, 'Application of the Boundary Element Method to Casting Solidifcation', *Metallurgical Transactions B*, **15**, 101-107, (March 1984).

[50] F. J. K. Ideriah, 'Turbulent Natural and Forced Convection in Plumes and Cavities', Ph.D. Thesis, Department of Mechanical Engineering, Imperial College, London, (1977).

[51] Y. Jaluria, *Natural Convection Heat and Mass Transfer*, Pergamon Press, (1980).

[52] J. W. Jerome, 'Nonlinear Equations of Evolution of a Genralized Stefan Problem', *Journal of Differential Eqn.*, **26**, 240–261, (1977).

[53] A. Jeyarajan, R. D. Pehlke, 'Casting Design by Computer', *AFS Transactions*, **83**, 405-412, (1975).

[54] A. Jeyarajan, R. D. Pehlke, 'Numerical Simulation of Casting Solidification', *AFS Transactions*, **9**, 2, 457-464, (June 1973).

[55] W. P. Jones, B. E. Launder, 'The Prediction of Laminarization with a Two–Equation Model of Turbulence', *Int. Joun. Heat Mass Transfer*, **15**, 301–314, (1972).

[56] S. Kou, R. Mehrablan, *eds.*, 'Modeling and Control of Casting and Welding Processes', *Proceedings of the Third Conference on Modelling of Casting and Welding Processes sponsored by the Engineering Foundation*, Santa Barbara, California, (January 12–17, 1986).

[57] A. I. Koler, J. D. Thomas, A. A. Tzavaras, 'Computations of Heat of Fusion in a Mathematical Model for Large Steel Cast Shapes', *Cast Metals Research Journal*, (Dec. 1973).

[58] A. N. Kolmogorov, 'Equations of Turbulent Motion in an Incompressible Fluid', *Izv. Akad. Nauk. SSSR, Sexia fizicheska* **VI**, 1–2, 56–58, (1968).

[59] K. Kublbeck, G. P. Merker, J. Straub, 'Advanced Numerical Computation of Two Dimensional Time Dependant Free Convection in Cavities ', *Int. J. Heat Mass Transfer*, **23**, 203-217.

[60] K. Y. M. Lai, M. Salcudean, 'Computer Analysis of Multidimensional Turbulent, Buoyancy–Induced, Two–Phase Flows in Gas–Agitated Liquid Reactors', *Computers and Fluids*, **15**, 3, 281–295, (1987).

[61] K. Y. M. Lai, M. Salcudean, S. Tanaka, R. I. L. Guthrie, 'Mathematical Modeling of Flows in Large Tundish Systems in Steelmaking', *Metallurgical Transactions B*, **17B**, 449–459, (1986).

[62] L. D. Landau, E. M. Lifshitz, *Fluid Mechanics*, Pergamon Press, London, (1959).

[63] B. E. Launder, D. B. Spalding, 'The Numerical Computation of Turbulent Flows',*Computer Methods in Applied Mechanics and Engineering*, **3**, (1974).

[64] A. Lazardis, 'A Computer Aided Solution of the Solidification Problem', *AFS Cast Metals Research Journal*, (March 1974).

[65] A. Lazardis, 'A Numerical Solution of the Multidimensional Solidification (or Melting) Problem' *Int. J. Heat Mass transfer*, **13**, 1459-1477, (1970).

[66] R. W Lewis, K. Morgan, *eds.*, 'Numerical Methods in Thermal Problems', *Proceedings of the Fourth International Conference*, held in Swansea, U.K., (1985).

[67] R. W. Lewis, K. Morgan, W. G. Habashi, *eds.*, 'Numerical Methods in Thermal Problems', **5**, *Proceedings of the Fifth International Conference* , Montreal, Canada , (June 29th–July 3rd, 1987), Pineridge Press, Swansea, U.K.

[68] R. W. Lewis, K. Morgan, O. C. Zienkiewicz, *eds.*, *Numerical Methods in Heat Transfer*, John Wiely and Sons Ltd, New York, (1981).

[69] D. G. Lilley, D. L.Rhode, 'A Computer Code for Swirling Turbulent Axisymmetric Recirculating Flows in Practical Isothermal Combustor Geometries', *NASA Contractor Report*, 3442, (1982).

[70] C. H. Low, 'Fluid Flow During Argon-Stirring in Ladles and Heat Transfer During Solidification in Molds', *MASc. Thesis*, Department of Mechanical Engineering, University of Ottawa, (1982).

[71] V. Lunardini, *Heat Transfer in Cold Climates*, Van Nostrand Reinhold Company, New York, (1981).

[72] A. L. Maples, D. R. Poirier, 'Convection In the Two Phase Zone of Solidifying Alloys', *Mettallurgical Transactions B*, **15B**, 163–172, (March 1984).

[73] R. E. Marrone, J. O. Wilkes, R. D. Pehlke, 'Numerical Simulation of Solidification, Part I: Low Carbon Steel Casting - T Shape', *AFS Cast Metals Research Journal*, (December 1970).

[74] R. E. Marrone, J. O. Wilkes, R. D. Pehlke, 'Numerical Simulation of Solidification, Part II: Low Carbon Steel Casting - L Shape', *AFS Cast Metals Research Journal*, (December 1970).

[75] Merzkirch, *Flow Visualization*, John Wiley and Sons, New York, (1974).

[76] G. H. Meyer, 'Multidimensional Stefan Problems', *SAIM Jour. Numer. Analysis.*, **10**, 3, 522–538, (1973).

[77] I. Minkoff, ***Solidification and Cast Structure***, John Wiley and Sons, New York, (1986).

[78] I. Minkoff, ***The Physical Metallurgy of Cast Iron***, John Wiley and Sons, New York, (1983).

[79] B. D. Nichols, C. W. Hirt, R. D. Hotchkiss, 'SOLA–VOF: A Solution Algorithm for transient Fluid Flow with Multiple Free Boundaries', ***Report LA-8355, Los Alamos Scientific Laboratory***, (1980).

[80] Y. Nishida, H. Matsubara, 'Effect of pressure on heat transfer at the metal mold inteface', ***British Foundrymen Journal***, **69**, 274–278, (1976).

[81] K. Ohtsuka, K. Mizuno, , J. Yamada, 'Application of a Computer Simulation System to Aluminum Permanent Mold Castings', ***AFS Transactions***, **90**, (1982).

[82] S. I. Pai, ***Fluid Dynamics of Jets***, D. Van Nostrand Co. , New York, (1954).

[83] S. V. Patankar, ***Numerical Heat Transfer and Fluid Flow***, McGraw Hill Book Co. , New York, (1982).

[84] D. W. Peaceman, H. H. Rachford, 'The Numerical Solution of Parabolic and Elliptic Differential Equations', ***Journ. of the Society of Ind. App. Math.***, bf3, 1, 28–41, (1955).

[85] R. D. Pehlke, M. J. Kirt, R. E. Marrone, D. J. Cook, 'Numerical Simulation of Casting Solidification', ***AFS Cast Metals Research Journal***, 9, 2, 49-55, (June 1973).

[86] D. R. Poirier, 'Permeability for Flow of Interdendritic Liquid in Columnar-Dendritic Alloys', ***Metallurgical Transactions B***, **18B**, 245–255, (March 1987).

[87] D. Poirier, M. Salcudean, 'On Numerical Methods used in Mathematical Modelling of Phase Change in Liquid Metals', ***ASME paper 86-WA/HT-22, pre-***

sented at the winter annual meeting of the ASME, Annaheim, California, (Dec 7–12, 1986).

[88] W. Pracht, 'Calculating Three Dimensional Fluid Flows At All Speeds with an Eularian Lagrangian Computing Mesh', *Journ. of Computational Physics*, **17**, 132–159, (1975).

[89] L. Prandtl, 'Uber ein neues Formel-System fur die ausgenbildate Turbulenz',*Nacr. Akad. Wiss.*, Gottinqin, Math.–Phys., K. L., 6, (1945).

[90] N. R. Ramachandran, J. P. Gupta, Y. Jaluria, 'Thermal and Fluid Flow Effects During Solidification in a Rectangular Enclosure', *Intern. Journ. Heat Mass Transf.*, **25**, 2, 187–194, (1982).

[91] J. Reade, *Canadian Foundry Association*, Personal communications, Ottawa, Ontario, (1986).

[92] G. P. Reddy, 'Design at the External Corners of V Junctions Using Numerical Techniques', *AFS Transactions*, **85**, 597-608, (1977).

[93] B. R. Robson, 'The Acceleration of Neutrally Buoyant Spheres in a Uniform Flowing Fluid', *Report LTR-LA-43, NRC*, Canada, (1970).

[94] W. Rodi, 'Turbulence Models and their Applications to Hydraulics, A State of the art Review.' International Association of Hydraulics Research, Delft, Netherlands, (1984).

[95] W. D. Rolph, D. Bathe, 'An Efficient Algorithm for Analysis of nonlinear Heat Transfer with Phase Changes', *Int. Journ. Num. Meth. Eng.*, **18**, 119–134, (1982).

[96] V. Sahajwalla, MaSc thesis, Department of Mechanical Engineering, UBC. Vancouver, B.C. (1988).

[97] M. Salcudean, Z. Abdullah, 'On the Numerical Modelling of Heat Transfer during Solidification Processes', *Int. Jour. Numer. Methods Eng.*, In Print, (1988).

[98] M. Salcudean, Z. Abdullah, 'Mathematical Modelling of Casting Processes', *Final Report to the Dept. of Energy Mines and Resources, Department of Mechanical Engineering, University of Ottawa*, (1987).

[99] M. E. Salcudean, Z. Abdullah, 'Numerical Simulation of Casting Processes', *Proceedings of the VIII International Heat Transfer Conference and Exhibition*, 459–464, San Fransisco, California, (August 12–22, 1986).

[100] M. Salcudean, Z. Abdullah, C. H. Low, K. Davis, 'Computation of Heat Transfer in a Casting', *Proceedings of the Tenth IASTD International Symposium, Applied Simulation and Modelling*, San Francisco, USA, (June 4-6, 1984).

[101] M. Salcudean, V. Costescu, Ardeleanu, 'Contributions to the Study of Ingot Solidification, Cooling and Heating Phenomena by Mathematical Modelling', *Rev. Roum. Sci. Tech. Met.*, **17**, 1, 39–49, (1972).

[102] M. Salcudean, R. I. L. Guthrie, 'A Three–Dimensional Representation of Fluid Flow Induced in Ladles or Holding Vessels by the Action of Liquid Metal Jets', *Met. Transactions AIME*, **10B**, 423–428, (1979).

[103] M. Salcudean, W. Hutny, A. Hurda, 'Thermal Stress Analysis in Molds', *Report by the Department of Mechanical Engineering, University of Ottawa*, (April, 1985).

[104] M. Salcudean, C. H. Low, A. Hurda, R. I. L. Guthrie, 'Computation of Three–Dimensional Flow and Heat Transfer in Gas Agitated Reactors', *Chem. Eng. Commun.*, **21**, 89–103, (1983).

[105] M. Salcudean, A. Mashaie, 'Mathematical Modelling of Heat Transfer in Permanent Molds', *Report to the Department of Energy Mines and Resources*

from the Department of Mechanical Engineering, University of Ottawa, (1983).

[106] H. Schlichting ,*Boundary Layer Theory*, McGraw–Hill, New York, 6th Ed., (1968).

[107] T. M. Shih, *Numerical Heat Transfer*, Hemisphere Publishing Co., New York, (1984).

[108] M. M. S. Sindir, *A Numerical Study of Turbulent Flows in a Backward Facing Step Geometry: A Comparison of four Models of Turbulence*, Ph.D. Thesis, Department of Mechanical Engineering, University of California, Davis, (1982).

[109] D. Sinitsin, MaSc thesis, Department of Mechanical Engineering, UBC. Vancouver, B.C. (1988).

[110] T. G. Smith, J. O. Wilkes, 'Laminar Free Surface Flow into a Vertical Cylinder', *Computers and Fluids*, 51–68 (1975).

[111] A. D. Solomon, V. Alexiades, D. G. Wilson, G. Geist, J. Kerper, 'An Enthalpy Method for the Solidification of a Supercooled Liquid', ORNL–6217, (1986).

[112] E. M. Sparrow, S. V. Patankar, S. Ramadhyani, 'Analysis of Melting in the Presence of Natural Convection in the Melt Region', *Transactions of the ASME*, **99**, Nov., (1977).

[113] M. J. Stewart, F. Weinberg, 'Fluid Flow through a Solid Liquid Dendritic Interface', *Metallurgical Transactions*, **3**, 333–337, (January 1972).

[114] R. A. Stoehr, 'Simulations in the Designs of Sand Castings', *Proceedings of the Conference on Modelling of Casting and Welding Processes; Met. Soc. of AMIE*, (1981).

[115] R. Stoehr, W. S. Hwang, 'Modelling the Flow of Molten Metal having a Free Surface During Entry Into Molds', *Proceedings of the 1983 Engineering*

Foundation Conferences–Modelling of Casting and Welding Processes II., The Metallurgical Society of AIME, (1983).

[116] V. L. Streeter, E. B. Wylie *Fluid Mechanics*, McGraw Hill, New York, (1985).

[117] D. Stropky, MaSc thesis, Department of Mechanical Engineering, UBC. Vancouver, B.C. (1988).

[118] L. J. D. Sully, 'The Thermal Interface Between Castings and Chill Molds', *AFS Transactions*, **84**, 735–744, (1979).

[119] J. Szekely, H. J. Wang, K. M. Kiser, 'Flow Pattern Velocity and Turbulence Energy Measurements and Predictions in a Water Model of an Argon Stirred Ladle',*Metalurgical Transactions B*, **7B**, 287–295, (1976).

[120] J. Szekely, R. T. Yadoya, 'The Physical and Mathematical Modelling of the Flow Field in the Mold Region in Continous Casting Systems: Part II. The Mathematical Representation of the Turbulent Flow Field', *Metallurgical - Transactions*, **4**, 1379–1388, (May 1973).

[121] B. G. Thomas, I. V. Samarasekera, J. K. Brimacombe, 'Comparison of Numerical Modeling Techniques for Complex, Two–Dimensional, Transient Heat–Conduction Problems', *Metallurgical Transactions B*, **15**, 2, (June, 1984).

[122] V. Voller, 'Implicit Finite Difference Solutions of the Enthalpy Formulation of Stefan Problems', *IMA Jour. of Numer. Analysis*, **5**, 201–214, (1985).

[123] V. Voller, 'Interpretation of the Enthalpy in a Discretized Multidimensional Region undergoing a Phase Change', *Int. Commun. Heat Mass Transf.*, **10**, 323–328, (1983).

[124] V. Voller, M. Cross, 'An Explicit Numerical Method to Track a Moving Phase Change Front', *Int. Jour. Heat Mass Transf.*, **26**, 1, 147–150, (1983).

[125] V. Voller, M. Cross, 'Use of an Enthalpy Method in The Solution of Stefan Problems', *Numerical Methods in Thermal Problems*, **3**, (R. W. Lewis, J. A. Johnson, W. R. Smith, *eds.*), Swansea, Pineridge Press, (1983).

[126] V. Voller, M. Cross, 'Accurate Solutions of Moving Boundary Problems Using the Enthalpy Method', *Int. Jour. Heat Mass Transf.*, **24**, 545–556, (1980).

[127] V. Voller, M. Cross, N. C. Markatos, 'An Enthalpy Method for Convective Diffusive Phase Change', *Int. Jour. Numer. Meth. Engineering*, **24**, 271–284, (1987).

[128] V. Voller, N. C. Markatos, M. Cross, 'Techniques for Accounting for the Moving Interface in Convection Diffusion Phase Change', *Proceedings of the Fourth International Conference in Numerical Methods in Thermal Problems*, Swansea, U. K. , (July 15-18, 1985).

[129] A. P. Watkins, Phd Thesis, Department of Mechanical Engineering, Imperial College, University of London, (1977).

[130] R. B. Weatherwax, O. K. Riegger, 'Computer Aided Solidification Study of a Die-Cast Aluminum Piston', *AFS Transactions*, **85**, 317-322, (1977).

[131] F. M. White *Viscous Fluid Flow*, McGraw Hill, New York, (1974).

[132] X. C. Zeng, R. D. Pehlke, 'Numerical Simulation of Solidification For a Copper-Base Alloy Casting', *AFS Transactions*, **92**, 479-488, (1984).

[133] O. C. Zienkiewicz, *The Finite Element Method*, McGraw Hill Book Co., New York, (1977).